



저작자표시-비영리-변경금지 2.0 대한민국

이용자는 아래의 조건을 따르는 경우에 한하여 자유롭게

- 이 저작물을 복제, 배포, 전송, 전시, 공연 및 방송할 수 있습니다.

다음과 같은 조건을 따라야 합니다:



저작자표시. 귀하는 원저작자를 표시하여야 합니다.



비영리. 귀하는 이 저작물을 영리 목적으로 이용할 수 없습니다.



변경금지. 귀하는 이 저작물을 개작, 변형 또는 가공할 수 없습니다.

- 귀하는, 이 저작물의 재이용이나 배포의 경우, 이 저작물에 적용된 이용허락조건을 명확하게 나타내어야 합니다.
- 저작권자로부터 별도의 허가를 받으면 이러한 조건들은 적용되지 않습니다.

저작권법에 따른 이용자의 권리는 위의 내용에 의하여 영향을 받지 않습니다.

이것은 [이용허락규약\(Legal Code\)](#)을 이해하기 쉽게 요약한 것입니다.

[Disclaimer](#)

Ph.D. DISSERTATION

**4H-SiC Homoepitaxial Growth on Various SiC  
Substrates for Power Device Application**

by

Hunhee Lee

August 2015

DEPARTMENT OF MATERIALS SCIENCE AND ENGINEERING  
COLLEGE OF ENGINEERING  
SEOUL NATIONAL UNIVERSITY

# ABSTRACT

Silicon carbide (SiC) has been considered as a promising wide bandgap material for high power, high frequency, and high temperature devices owing to its high breakdown field ( $\sim 3 \times 10^6$  V/cm), high thermal conductivity, high saturated electron drift velocity ( $\sim 2 \times 10^7$  cm/s), and chemical stability. The commercialization of its large single-crystal wafer and excellent epitaxial growth technique provide a better candidate for application in high-power and high-frequency electronic devices compared with other wide-bandgap materials such as GaN, ZnO, and diamond. Among the many SiC polytypes, most of the recent work has focused on 4H-SiC, owing to its high saturated electron drift velocity and commercial availability. For growth of high quality SiC epitaxial layers, many techniques were tried such methods as molecular-beam epitaxy (MBE), liquid-phase epitaxy (LPE), and vapor-phase epitaxy (VPE), there are some remaining problems. To solve this problem, the author focuses on the homoepitaxial growth of a 4H-SiC epilayer by MOCVD using bis-trimethylsilylmethane (BTMSM,  $C_7H_{20}Si_2$ ). BTMSM is an organo-silicon source which has a non-toxic and non-flammable nature, thus giving it certain advantages in comparison with the normal process using silane ( $SiH_4$ ). Moreover, because BTMSM has a Si-C bonding structure, low temperature epitaxial growth is also possible.

Homoepitaxial growth of SiC epitaxial layers on various substrates including 4H-SiC  $4^\circ$ ,  $8^\circ$  off-axis, on-axis Si-face substrates, and C-faces substrates was carried out at temperature ranging from 1240 to 1550 °C and carrier gas flow rates of 5-20 sccm for the BTMSM source.

In the case of homoepitaxial growth on various off-angle substrates, it was found that the structure perfection of SiC epilayers is improved with higher temperature and lower flow rate of BTMSM. This growth behavior can be explained by the step-controlled epitaxy model. At the nominally on-axis surface spiral growth occurs via micro-steps provided by screw dislocations intersecting the surface. When growth temperature became 1480 °C on the nominally on-axis, we conducted island growth, which possesses a number of blocks, but hexagonal shapes were sparsely appeared. In addition, epilayer began to have smooth surface in macroscopic view as well as a shape of continuous chain of hexagonal-shape, when the temperature reached 1550 °C. When epilayer grows at 1480 °C, 4H-SiC was grown to a hexagonal shape, and nearby blocks were composed of 3C-SiC. This means the application of BTMSM source enabled growth of 4H-SiC at a relatively lower temperature of 1480 °C, which is the same as the polytype of substrate. Moreover, we could identify that 4H-SiC could grow at 1550 °C, satisfying stability of 4H-SiC polytype for 100%. The whole area was grown to 4H-SiC epilayer, revealing two types of surface regions which are hexagonal chain-shape and smooth surface. The smooth surface could be obtained due to high dislocation density of the area when compared to the hexagonal chain region. Increasing the growth temperature helps to enhance the mobility of the adatoms on the surface, lowering the probability for a two dimensional nucleation of 3C.

Many researchers have attempted epitaxial growth using 4H-SiC Si-face substrates, but there are few studies that have investigated the epitaxial growth on the C-face. Therefore, it is essential to determine the dependence of the

quality of epitaxial layers on substrate polarity. This study has its significance in that an organosilicon source material of BTMSM was used and the epitaxial growth on C-face 4H-SiC substrates was analyzed in detail, which has not been previously attempted by other groups. *In situ* H<sub>2</sub> etching and homoepitaxial growth of 4H-SiC have been carried out on 4° off-axis Si-face and C-face 4H-SiC substrates by low-pressure CVD. H<sub>2</sub> etching characteristics and epitaxial growth behaviors on two different polarities using a BTMSM were systematically analyzed and discussed. When the temperature of *in situ* H<sub>2</sub> etching was 1500 °C, the Si-face and C-face showed macro step-bunching and some clusters, respectively, whereas both faces showed fairly good quality when treated at 1450 °C for 10 min. High-quality 4H-SiC epitaxial layers with less crystallographic defects and free of step-bunching were demonstrated on both Si-face and C-face substrates. The optimal growth temperature on the Si-face substrate was 1320-1440 °C with a BTMSM source flow rate of 5-10 sccm, while the growth temperature should be increased to 1500 °C on the C-face substrate with a lower source flow rate of 5 sccm. A mechanism for the observed generation of step-bunching and surface morphological defect on both substrates depending on the growth temperature and source flow rate was also proposed.

**Keywords : 4H-SiC, homoepitaxial growth, BTMSM, Si- and C-face substrate, off-axis angle, on-axis substrate**

**Student Number : 2009-23054**

**Hunhee Lee**

# CONTENTS

<b>Abstract</b> .....	i
<b>Contents</b> .....	iv
<b>List of Tables</b> .....	vii
<b>L i s t o f</b>	
<b>Figures</b> .....	viii

## **1. Introduction**.....1

1 . 1 . O v e r v i e w	1
1 . 2 . D i s s e r t a t i o n	1
Outline .....	2

## **2. Literature Review**.....3

2 . 1 . P r o p e r t i e s o f	
SiC .....	3
2 . 1 . 1 . P h a s e E q u i l i b r i u m a n d	
P o l y t y p i s m .....	3
2.1.2. Physical properties of SiC and Its Potential	
A p p l i c a t i o n s . . . . .	8
2.1.2.1. Mechanical Properties.....	8
2.1.2.2. Thermal Properties.....	8
2.1.2.3. Optical Properties.....	12
2 . 1 . 2 . 4 . E l e c t r i c a l	
Properties .....	12
2 . 1 . 2 . 5 . P o t e n t i a l A p p l i c a t i o n s o f	
S i C .....	15
2 . 2 . S i C E p i t a x i a l G r o w t h	

.....	19
2.2.1. Chemical Vapor Deposition (CVD) .....	19
2.2.1.1. Principle of CVD process .....	21
2.2.1.2. Heteroepitaxial Growth of 3C-SiC .....	24
2.2.1.3. Homoepitaxial Growth of 3C-SiC .....	25
2.2.1.4. Homoepitaxial Growth of $\alpha$ -SiC .....	26
2.2.1.5. Structural Properties of $\alpha$ -SiC .....	33
2.2.1.6. Growth Equipment and Precursor Materials for CVD .....	36
2.3. SiC Doping.....	38
2.3.1. Site-competition Epitaxy.....	38
2.3.2. Diffusion of Impurities in SiC .....	39
2.3.2.3. Ion Implantation.....	40
2.4. Step Kinetics on Vicinal Surface.....	43
2.5. SiC Power Device Application.....	49
Bibliography.....	53
<b>3 .      E x p e r i m e n t a l</b>	
<b>Procedure</b> .....	60
3.1. CVD System.....	60
3.2. Procedure for the Growth of 4H-SiC Epitaxial Layer.....	62



BTMSM.....	98
4.2.1. Introduction	
.....	98
4.2.2. 4H-SiC Epitaxial Layers Grown on 8° off-axis Substrates..	100
4.2.2.1. Morphological Characteristics.....	100
4.2.2.2. Structural Characteristics.....	105
4.2.3. 4H-SiC Epitaxial Layers Grown on 4° off-axis Substrates...	111
4.2.3.1. Morphological Characteristics.....	111
4.2.3.2. Structural Characteristics.....	116
4.2.4. 4H-SiC Epitaxial Layers Grown on On-axis Substrates .....	122
4.2.4.1. In-situ surface preparation.....	122
4.2.4.2. 4H-SiC Epitaxial Growth on On-axis Substrates.....	126
4.2.4.3. Growth Rate.....	140
Bibliography.....	142

**5. Conclusions.....146**

**L i s t o f Publications.....149**

**A b s t r a c t ( i n**

**Korean)** ..... 156

# LIST OF TABLES

Table 2.1. Lattice constants of different SiC polytypes. Theoretical values are taken from or have been calculated recently. Experimental values have been taken from (2H), (3C), and (4H and 6H).

Table 2.2. Mechanical Properties of 3C-, 4H-, and 6H-SiC.

Table 2.3. Thermal properties of SiC polytypes.

Table 2.4. The optical band gaps and exciton energy gaps for SiC polytypes.

Table 2.5. The electrical properties of common SiC polytypes, Si, GaAs, and GaN.

Table 2.6. Figures of merit for selected semiconductors.

# LIST OF FIGURES

- Fig. 2.1. Phase diagram of the binary system Si-C.
- Fig. 2.2. The tetragonal bonding of a carbon atom with the four nearest Silicon neighbours. The distance  $a$  is approximately  $3.08 \text{ \AA}$ .
- Fig. 2.3. The close packing of spheres. There are three possible position for a layer (A, B, and C).
- Fig. 2.4. Illustration of different polytypes of SiC. (a) The position of the first layer of atoms of Si and C is illustrated as A whereas the next layers can be shown as B and C. The top-view and side-view of 3C, 4H, and 6H polytypes are shown in (b), (c), and (d) respectively.
- Fig. 2.5. Schematic illustration of simple surface diffusion model, where steps with a height  $h$  are separated by an equal distance.
- Fig. 2.6. The distribution of adatom concentration and supersaturation ratio  $\alpha$  ( $= n_s/n_{s0}$ ) on off-axis surface.
- Fig. 2.7. Critical growth conditions as a function of growth temperature, growth rate, and off-angles of the substrate ( $\theta = 0.2^\circ, 1^\circ, 3^\circ, 6^\circ, \text{ and } 10^\circ$ ). The top-left and bottom-left regions from the curves correspond to two-dimensional nucleation and step-flow growth conditions, respectively.
- Fig. 2.8. Schematic images of the relationship between growth modes and polytypes of grown layers. Homoepitaxy of 4H-SiC is achieved owing to step flow growth (a), and 3C-SiC is grown through two-dimensional nucleation (b).

Fig. 2.9. Diffusion coefficients for different impurities in 6H-SiC. [1: Be (bulk diffusion), 2: Be (diffusion in the surface region), 3: B (Bulk diffusion), 4: B (diffusion in the surface region), 5: Al, 6: Ga, 7: oxygen, 8-1 and 8-2: nitrogen]

Fig. 2.10. One dimensional picture of the step flow growth. Region 1 indicate upper terrace region and region 2 indicates lower terrace region.  $K^-$  and  $K^+$  is kinetic coefficient influencing asymmetric kinetics at step edge.

Fig. 2.11. Model potential for adatoms near a step edge. (a) Normal and (b) inverse ES barrier.

Fig. 2.12. Schematic of SiC high power electronic devices.

Fig. 2.13. Comparison SiC-IPM with Si IPM.

Fig. 2.14. Scematic of SiC high power electronics devices for Toyota's HEV (Hybrid electric Vehicle), FCEV (Fuel Cell Hybrid Vehicle).

Fig. 3.1. Schematic diagram of MOCVD system.

Fig. 3.2. The schematic diagram of the reactor chamber of CVD system.

Fig. 3.3. The structure of bis-trimethylsilylmethane. Silicon atoms bonded tetrahedrally with carbon atoms, which is the same structure of SiC crystal.

Fig. 4.1. AFM images of (a) Si-face (b) C-face bare substrate, (c) Si-face (d) C-face substrate after H<sub>2</sub> etching at 1500 °C, and (e) Si-face (f) C-face substrate after H<sub>2</sub> etching at 1450 °C.

Fig. 4.2. (a) AFM image and (b) Nomarski micrograph of 4H-SiC epitaxial layer grown at 1400 °C on 4° off-axis Si-face substrates. (BTMSM

Source flow rate: 10 sccm)

Fig. 4.3. Peak to valley of height profile data of AFM images of 4H-SiC epilayers grown on 4° off-axis Si-face substrates at various conditions.

Fig. 4.4. RMS roughness of AFM image in 4H-SiC epitaxial layer, which was grown at various growth temperatures and flow rates of BTMSM carrier gas.

Fig. 4.5. Micro-Raman spectra (FTO phonon mode) of various growth temperatures for epilayers on Si-face substrates.

Fig. 4.6. (a) AFM image of 4H-SiC epitaxial layer grown at 1500 °C on 4° off-axis Si-face substrates, and (b) its peak to valley of the height profile data. (BTMSM source flow rate: 10 sccm)

Fig. 4.7. (a) Nomarski micrographs of 4H-SiC epitaxial layers grown at various growth conditions on 4° off-axis C-face substrates. (b) AFM image of the inverted pyramid defect.

Fig. 4.8. (a) AFM image, and (b) the peak to valley of the height profile of the AFM image of 4H-SiC epitaxial layer grown at 1500 °C on 4° off-axis C-face substrates. (BTMSM source flow rate: 10 sccm)

Fig. 4.9. FWHM difference of 4H-SiC (0004) rocking curves before and after the epitaxial grown on the C-face substrates as a function of (a) growth temperature and (b) BTMSM source flow rate.

Fig. 4.10. Micro-Raman spectra of various growth temperatures for epilayers on C-face substrates.

Fig. 4.11. Complex triangular defect occurring with higher BTMSM flow rate

of 15 sccm on the C-face. (a) The optical image, (b) Micro-Raman spectra of the point “A” shown in (a), (c) Raman intensity ratio map of the peak at  $796\text{ cm}^{-1}$  (3C-TO phonon mode) to the peak at  $776\text{ cm}^{-1}$  (4H-TO phonon mode) for the defect shown in (a).

Fig. 4.12. (a) Nomarski micrographs of the defective region of 4H-SiC epitaxial layers grown at temperature of  $1500\text{ }^{\circ}\text{C}$  and source flow rate of 15 sccm on  $4^{\circ}$  off-axis C-face substrates. (b) The schematic diagram of the defective region in (a).

Fig. 4.13. Micro-Raman spectra of the defect free zone and isolated inverted pyramid defect. Inset image is the Nomarski image of the inverted pyramid defect.

Fig. 4.14. Nomarski micrographs of 4H-SiC epitaxial layers grown at various growth conditions on  $8^{\circ}$  off-axis substrates.

Fig. 4.15. AFM images of 4H-SiC epitaxial layers grown at various growth conditions on  $8^{\circ}$  off-axis substrates.

Fig. 4.16. RMS roughness of AFM image in 4H-SiC epitaxial layer, which was grown on  $8^{\circ}$  off-axis substrates at various (a) growth temperatures and (b) flow rates of BTMSM carrier gas.

Fig. 4.17.  $\omega$ -Rocking curve for (a) substrate and (b) epilayer grown on  $8^{\circ}$  off-axis substrate at  $1400\text{ }^{\circ}\text{C}$ .

Fig. 4.18. Typical EBSD pattern of the SiC homoepitaxial film on  $8^{\circ}$  off-axis substrate grown at  $1320\text{ }^{\circ}\text{C}$ . (a) Kikuchi diffraction pattern of EBSD, and (b) indexed EBSD pattern.

Fig. 4.19. (a) Micro-Raman spectra (FTO, FLO phonon mode) of various

growth temperatures for epilayers on 8° off-axis substrates.

Magnified view of (b) FTO phonon mode (C) FLO phonon mode.

Fig. 4.20. (a) Micro-Raman spectra (FTO, FLO phonon mode) of various flow rates of BTMSM carrier gas for epilayers on 8° off-axis substrates.

Magnified view of (b) FTO phonon mode (C) FLO phonon mode.

Fig. 4.21. AFM images of 4H-SiC epitaxial layers grown at various growth conditions on 4° off-axis substrates.

Fig. 4.22. Nomarski micrographs of 4H-SiC epitaxial layers grown at various growth conditions on 4° off-axis substrates.

Fig. 4.23. RMS roughness of AFM image in 4H-SiC epitaxial layer, which was grown on 4° off-axis substrates at various (a) growth temperatures and (b) flow rates of BTMSM carrier gas.

Fig. 4.24.  $\omega$ -Rocking curve for (a) substrate and (b) epilayer grown on 8° off-axis substrate at 1400 °C.

Fig. 4.25. Typical EBSD pattern of the SiC homoepitaxial film on 4° off-axis substrate grown at 1400 °C. (a) Kikuchi diffraction pattern of EBSD, and (b) indexed EBSD pattern.

Fig. 4.26. (a) Micro-Raman spectra (FTO, FLO phonon mode) of various growth temperatures for epilayers on 4° off-axis substrates.

Magnified view of (b) FTO phonon mode (C) FLO phonon mode.

Fig. 4.27. (a) Micro-Raman spectra (FTO, FLO phonon mode) of various flow rates of BTMSM carrier gas for epilayers on 4° off-axis substrates.

Magnified view of (b) FTO phonon mode (C) FLO phonon mode.

Fig. 4.28. SEM and AFM images of (a), (b) bare on-axis, (c), (d) treated on-

axis substrate.

Fig. 4.29. (a) AFM image, and (b) the peak to valley of the height profile of the AFM image of 4H-SiC on-axis substrate after H<sub>2</sub> etching at 1470 °C.

Fig. 4.30. AFM images of 4H-SiC epitaxial layer grown at (a) 1240 (b) 1280 (c) 1320 (d) 1360 (e) 1400 (f) 1440 °C on Si-face on-axis substrates. (BTMSM Source flow rate: 10 sccm)

Fig. 4.31. RMS roughness of AFM image in 4H-SiC epitaxial layer, which was grown on Si-face on-axis substrates at various growth temperatures with flow rates of BTMSM carrier gas of 10 sccm.

Fig. 4.32. NMS images of 4H-SiC epitaxial layer grown at (a) 1240 (b) 1280 (c) 1320 (d) 1360 (e) 1400 (f) 1440 °C on Si-face on-axis substrates. (BTMSM Source flow rate: 10 sccm)

Fig. 4.33. NMS images of 4H-SiC epitaxial layer grown at (a) 1480 (b) 1520 (c) 1520 °C (another part) on Si-face on-axis substrates. (BTMSM Source flow rate: 10 sccm)

Fig. 4.34. (a) Micro-Raman spectra (FTO, FLO phonon mode) of various growth temperatures for epilayers grown on Si-face on-axis substrates. Magnified view of (b) FTO phonon mode (C) FLO phonon mode.

Fig. 4.35. 4H-SiC epitaxial layer grown at 1480 °C on Si-face on-axis substrates. (BTMSM Source flow rate: 10 sccm) (a) The optical image, (b) magnified image of (a), (c) Raman intensity map of the peak at 972 cm<sup>-1</sup> (3C-LO phonon mode) for the shown in (b).

Fig. 4.36. EBSD mapping of the SiC epitaxial layer on on-axis substrate grown at 1480 °C. (a) NMS image, (b) SEM image, and (c) EBSD mapping image for the shown in (b).

Fig. 4.37. EBSD mapping of the SiC epitaxial layer on on-axis substrate grown at 1550 °C. (a) NMS image, (b) SEM image, and (c) EBSD mapping image for the shown in (b).

Fig. 4.38. EBSD mapping of the SiC epitaxial layer on on-axis substrate grown at 1550 °C (another part). (a) NMS image, (b) SEM image, and (c) EBSD mapping image for the shown in (b).

Fig. 4.39. (a) SEM, (b) AFM image, (c) 2D image of AFM, and (d) the peak to valley of the height profile of the AFM image of 4H-SiC epitaxial layer grown at 1550 °C on Si-face on-axis substrate. (BTMSM Source flow rate: 10 sccm)

Fig. 4.40. Cross-section SEM micrograph of 4H-SiC epitaxial layers grown on Si-face on-axis substrates at various growth conditions.

# 1. Introduction

## 1.1. Overview

With the impressive development of the information technology, the semiconductor industry has grown explosively. While Si-based semiconductor devices are still dominant in market (over 90%) and continue growing, there have been a lot of efforts in the development of compound semiconductor devices for electrical and optical devices, especially in the full range of wavelength, and for electronic devices operating at high frequency, high power, high temperatures, and harsh environments. In most cases, these devices involve growing epitaxial layers by molecular beam Epitaxy (MBE), chemical vapor deposition (CVD), and vapor phase epitaxy (VPE). Among them, the silicon carbide (SiC) is likely candidate to replace Si in the near future due to their superior electrical, mechanical properties which will be discussed in detail in chapter 2. During recent years, great progress has been made in the growth of SiC single crystals and epitaxial films. However, the quality of the grown crystals and epilayer still needs further improvement, because the crystals still contain a number of various structural defects, such as micropipes, dislocations, inclusions, and mosaic structure, etc., of which the formation is strongly related to the key parameters of epitaxial growth process. So, in order to exploit the promising potential of SiC material, first, it is essential to obtain the high quality epitaxial films with precise doping controls. It has been well known that the heteroepitaxial growth with silicon

substrate causes the resulting epilayer to have a high defect level because of the large differences in the crystal lattice constants and the thermal expansion coefficients of Si and 3C-SiC. Therefore, homoepitaxy that, in principle, eliminates the lattice constant and the thermal expansion mismatches is preferable for the structurally perfect epilayer. However, a reduction of the growth temperature, improvement of crystallinity, and precise doping control are still required. To solve these problems, an organo-silicon precursor, bis-trimethylsilylmethane (BTMSM,  $C_7H_{20}Si_2$ ) was used. BTMSM is an organo-silicon source which has a nontoxic and nonflammable nature, thus giving it certain advantages in comparison with the normal process using silane ( $SiH_4$ ). Moreover, because BTMSM has an Si-C bonding structure, low temperature epitaxial growth is also possible.

## **1.2. Dissertation Outline**

The literature review and the background of SiC semiconductor material and its applications will be presented in Chapter 2. In Chapter 3, the experimental procedure will be shown. Chapter 4 discusses the results of the 4H-SiC epitaxial layers grown on various substrates including  $4^\circ$ ,  $8^\circ$  off-axis, on-axis Si-face substrates, and C-faces substrates. Finally, chapter 5 presents a brief summary, including the conclusion.



## 2. Literature Review

### 2.1. Properties of SiC

#### 2.1.1. Phase Equilibrium and Polytypism

Silicon carbide is the only compound species in the Si-C binary system that exists in the solid state, as shown in Fig. 2.1. However, it is difficult to grow from a stoichiometric melt due to the peritectic nature of the material. The solubility of carbon in molten silicon is very low at temperatures below 2270 K, for example, the solubility is only 0.1% at 2073 K.

Silicon carbide was one of the first semiconductors discovered and its large cohesive energy made people mistake it for an element. SiC is the only known binary compound of silicon and carbon. The basic structural unit of SiC consists of a primarily covalently bonded tetrahedron of four carbon atoms with a silicon atom positioned at the center of mass of the tetragonal structure (or vice versa), as shown in Fig. 2.2. The approximate bond length between the Si-Si or C-C atoms is 3.08 Å [1] whereas the distance between Si and C is approximately 1.89 Å [2]. The SiC crystals are constructed with these tetrahedral joined to each other at the corners. When the same chemical compound exists in two or more crystallographic forms, these forms are called polymorphs and the phenomenon is called polymorphism. In certain close-packed structures, there exists a special one-dimensional type of

polymorphism called polytypism. Polytypes are alike in the two dimension of the close-packed plane but differ in the stacking sequence in the dimension perpendicular to the close-packed plane.

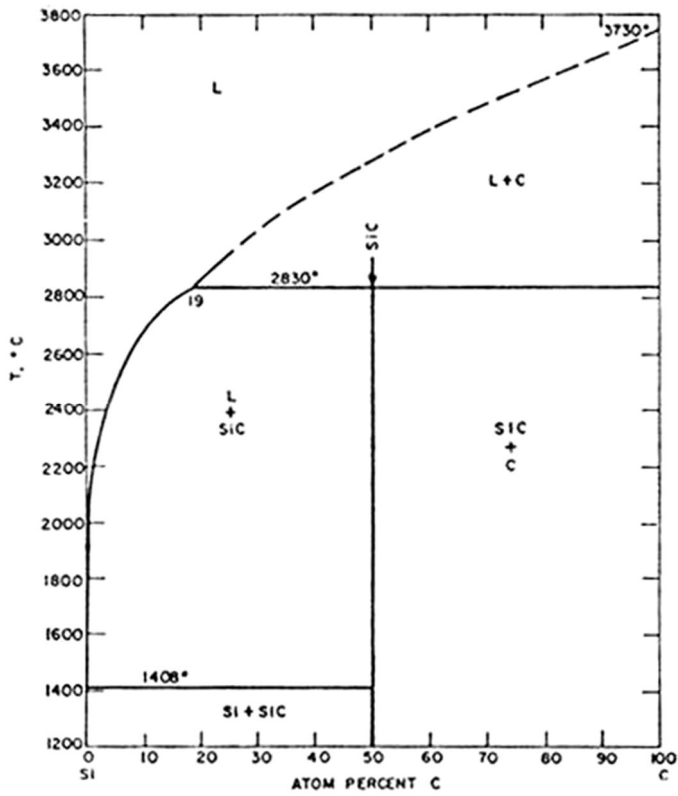


Fig. 2.1. Phase diagram of the binary system Si-C. [99]

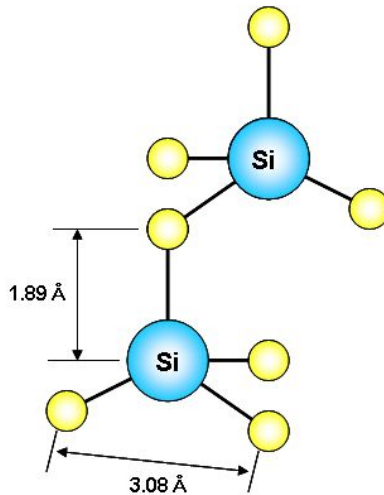


Fig. 2.2. The tetragonal bonding of a carbon atom with the four nearest silicon neighbours. The distance  $a$  is approximately  $3.08 \text{ \AA}$ . [1]

In a polytypic compound, similar sheets of atoms or symmetrical variants are stacked atop each other and related according to a symmetry operator. The differences among the polytypes arise only in the direction perpendicular to the sheets (along the  $c$ -axis). In SiC, the sheets can be represented as a close-packed array of spheres forming a two-dimensional pattern with six-fold symmetry. Each sheet represents a bilayer compound of one layer of Si atoms and one layer of C atoms. Using the notations from hexagonal crystal structures, the first sheet can be defined as the basal or  $c$ -plane with Miller-indexed directions according to Fig. 2.3. The most stable way to stack an identical second sheet of close-packed spheres is to place the spheres atop the "valleys" in the first sheet. There are two possibilities for arranging the second sheet relative to the first sheet in this way. The second sheet may be displaced along, for example,  $[1-100]$  until the spheres lie in the valleys denoted "B" in

Fig. 2.3, or the sheet may be displaced along, for example,  $[1-100]$  until the spheres lie in the valleys denoted "C" in Fig. 2.3. Thus, a sheet can be denoted A, B, or C, depending on the positions of its spheres. All polytypes can be described as different stackings of A, B, and C sheets, with the restriction that sheets with the same notation cannot be stacked upon each other. A large number of SiC polytypes exist (some sources mention more than 250 [3]), with some having stacking sequences of several hundreds of bilayers. The crystal structures of the SiC polytypes are cubic, hexagonal, or rhombohedral. The only cubic polytype is referred to as  $\beta$ -SiC, whereas the hexagonal and rhombohedral polytypes are referred to collectively as  $\alpha$ -SiC. Due to the increasing number of discovered polytypes of  $\alpha$ -SiC, it was suggested that each polytype could be named with a number according to the periodicity in the stacking direction and the letter H, for hexagonal, or R, for rhombohedral [4]. Subsequently, it became common to refer to  $\beta$ -SiC as 3C-SiC.

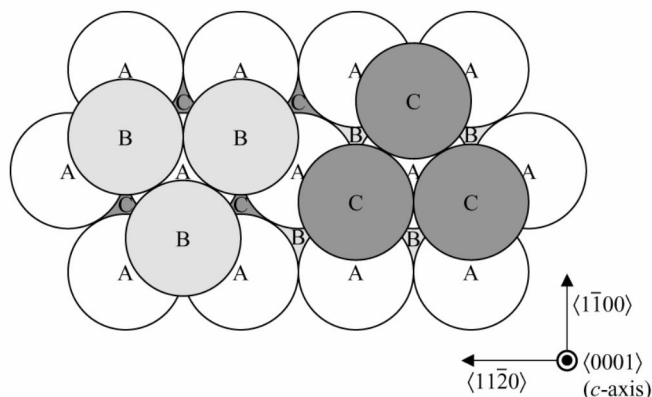


Fig. 2.3. The close packing of spheres. There are three possible position for a layer (A, B, and C). [99]

The purely wurtzite ABAB... stacking sequence (with the stacking along the [0001] direction) is denoted as 2H-SiC reflecting its two bilayer stacking periodicity and hexagonal symmetry. Another simple stacking sequence of ABCABC... produces the zincblende 3C structure (with the stacking along the [111] direction), which is the only possible cubic polytype. All of the other polytypes are mixtures of the fundamental zincblende and wurtzite structures. Some common hexagonal polytypes with more complex stacking sequences are 4H- and 6H-SiC. 4H-SiC is composed equally of cubic and hexagonal structures, while 6H-SiC is two thirds cubic. Despite the cubic elements, each has overall hexagonal crystal symmetry. The stacking sequences for 4H and 6H are ABACABAC... and ABCACBABCACB... respectively. Fig. 2.4 illustrates most common polytypes of SiC: 3C, 4H, and 6H.

Figure 2.4 is the illustration of different polytypes of SiC. (a) The position of the first layer of atoms of Si and C is illustrated as A whereas the next layers can be shown as B and C. The top-view and side-view of 3C, 4H, and 6H polytypes are shown in (b), (c), and (d), respectively.

The extent to which a real crystal structure approximates a close packing can be determined by its lattice constants. Any close packing can be conveniently referred to the hexagonal axes. If  $c$  denotes the height of the hexagonal unit cell,  $n$  the identity period, and  $h$  the separation between successive layers, then  $c = nh$ . Simple calculation gives:

$$\frac{c}{a} = \frac{nh}{a} = 0.8165 \times n \quad (2.1)$$

The axial ratio  $c/a$  for an ideally close packed structures must be an integral multiple of 0.8165. However, in the case of  $\alpha$ -SiC, the value of  $c/na$

deviates from 0.8165 due to the local relaxation as shown in Table 2.1 [10]. This difference of the lattice constant can be utilized to identify the polytype of SiC by high resolution X-ray diffraction (HRXRD).

## **2.1.2. Physical properties of SiC and Its Potential Applications**

### **2.1.2.1. Mechanical Properties**

SiC has robust mechanical property and chemical stability which are presented in Table 2.2 [11]. Its favorable mechanical properties such as high elastic modulus and toughness, in combination with its large band gap, make SiC an excellent material for high temperature applications. Compared to Si, SiC has demonstrated higher chemical inertness and radiation resistance which also increase its potential for sensors operating in adverse environments. Such applications are in instrumentation and control of nuclear power systems which require high temperature transducers capable of operating in radiation environment. In comparison to diamond, attractive features of SiC are that it can be easily doped both p- and n-type using well-known p-type dopants of aluminum and n-type dopants of nitrogen. In addition, SiC has a natural oxide to be grown on its surface.

### **2.1.2.2. Thermal Properties**

The excellent high-temperature properties make SiC very suitable for high

high-temperature electronic applications. The high elastic modulus of SiC and the relatively low atomic weights of Si and C promote harmonic lattice vibrations, giving SiC a high thermal conductivity. The values at room temperature for some polytypes are given in Table 2.3 [12]. The 3~10 times high thermal conductivity compared to the conventional semiconductors such as Si and GaAs makes SiC a promising material for high power and high frequency device applications.

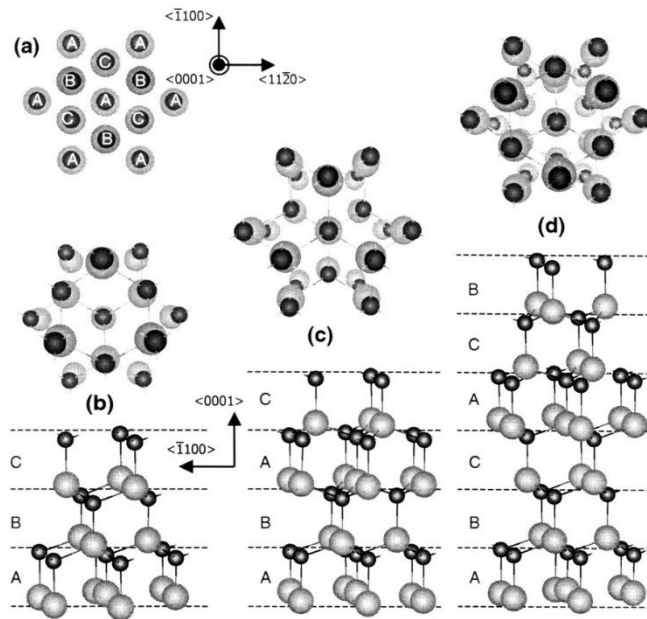


Fig. 2.4. Illustration of different polytypes of SiC. (a) The position of the first layer of atoms of Si and C is illustrated as A whereas the next layers can be shown as B and C. The top-view and side-view of 3C, 4H, and 6H polytypes are shown in (b), (c), and (d) respectively.

Table 2.1. Lattice constants of different SiC polytypes. Theoretical values are taken from [5] or have been calculated recently [10]. Experimental values have been taken from [7] (2H), [8] (3C), and [9] (4H and 6H).

polytype	ref.	a(Å)	c/n (Å)	c/(na)
3C	[5]	3.034	2.477	0.8165
	[6]	3.063	2.501	0.8165
	[8]	3.083	2.517	0.8165
6H	[5]	3.033	2.480	0.8177
	[6]	3.062	2.502	0.8172
	[9]	3.081	2.520	0.8178
4H	[5]	3.032	2.482	0.8185
	[6]	3.061	2.503	0.8179
	[9]	3.081	2.521	0.8184
2H	[5]	3.031	2.480	0.8185
	[6]	3.057	2.508	0.8201
	[7]	3.076	2.524	0.8205

Table 2.2. Mechanical Properties of 3C-, 4H-, and 6H-SiC. [11]

polytype	Young's modulus (GPa)	Mohs hardness	Acoustic velocity (ms <sup>-1</sup> )
3C	392-448	~9	12600
6H		~9	13730
4H		~9	13260

Table 2.3. Thermal properties of SiC polytypes. [99]

	3C-SiC	4H-SiC	6H-SiC
Thermal conductivity (Wcm <sup>-1</sup> K <sup>-1</sup> )	4.9	4.9	4.9
Thermal expansion coefficient (K <sup>-1</sup> )	$2.9 \times 10^{-6}$		$4.2 \times 10^{-6}$ (   a-axis) <sup>a</sup> $4.68 \times 10^{-6}$ (   c-axis) <sup>a</sup>
Decomposition temperature (°C)	$2839 \pm 40$		

<sup>a</sup> measured at 700 K

### 2.1.2.3. Optical Properties

SiC polytypes have relatively high band gap energies, ranging from 2.39 to 3.33 eV at 0K. These different band gap energies originate from the different polytypes structures that cause changes in the configurations of the valence and conduction bands. With the exception of 2H- and 3C-SiC, there are a limited number of band-structure calculations, mainly due to the rather large number of atoms in the unit cells. All polytypes have the indirect band gaps. In general, the band gap values increase with the degree of hexagonality. The values of the optical band gaps and exciton energy gaps for SiC polytypes are shown in Table 2.4 [13].

### 2.1.2.4. Electrical Properties

The electrical properties of SiC are different for each polytype, as shown in Table 2.5. The table also shows the electrical properties for Si, gallium arsenide (GaAs), and gallium nitride (GaN). The electron and hole mobilities in SiC are a function of carrier concentration, polytype, structural perfection, and temperature. There has been a tendency towards increasing mobilities and decreasing residual carrier concentration for unintentionally doped epitaxial layers. The electron mobility of 3C-SiC was predicted from theoretical calculations to be significantly greater than can be obtained from 6H-SiC, due to reduced phonon scattering in the cubic material. For this reason, there was early interest in the growth of thin film of 3C-SiC for device applications.

However, most recent work has concentrated on the use of 4H-SiC, which has a theoretical electron mobility essentially the same as 3C-SiC and much greater than 6H-SiC. In addition, 4H-SiC has identical mobilities along the vertical and horizontal directions, whereas 6H-SiC has anisotropic mobilities. The breakdown field of 3 MV/cm is one order of magnitude larger than Si and GaAs. This parameter is important in order to reduce on-resistance in power devices. The high saturation drift velocity ( $2 \times 10^7$  cm/s) also enables SiC to operate in devices at high frequencies.

Table 2.4. Optical band gaps and exciton energy gaps for SiC polytypes. [13]

	3C-SiC	6H-SiC	15R-SiC	4H-SiC	2H-SiC
Hexagonality	0	33	40	50	100
Optical bandgap (eV, room T)	2.2	2.86	-	3.26	-
Exciton energy gap (eV, 0 K)	2.39	3.023	2.986	3.265	3.33

Table 2.5. The electrical properties of SiC polytypes, Si, GaAs, and GaN. [99]

	3C-SiC	4H-SiC	6H-SiC	Si	GaAs	GaN
Electron mobility ( $\text{cm}^2\text{V}^{-1}\text{s}^{-1}$ )	1000	900	450	1500	8500	900
Hole mobility ( $\text{cm}^2\text{V}^{-1}\text{s}^{-1}$ )	50	100	50	450	400	20
Breakdown electric field ( $\times 10^6 \text{Vcm}^{-1}$ )	2	3	3	0.3	0.4	3
Thermal conductivity ( $\text{Wcm}^{-1}\text{K}^{-1}$ )	4.9	4.9	4.9	1.5	0.46	1.3
Saturated electron drift velocity ( $\times 10^7 \text{cm}^{-1}$ )	2.7	2.2	1.9	1	2	2
Relative dielectric constatt ( $\epsilon_r$ )	9.7	10.03	10.03	11.9	12.8	10.4
Band gap (eV)	2.39	3.26	3.02	1.12	1.42	3.42

### 2.1.2.5. Potential Applications of SiC

The high breakdown field and high thermal conductivity of SiC coupled with high operational junction temperatures theoretically permit extremely high power densities and efficiencies to be realized. The high breakdown field of SiC relative to Si or GaAs enables the blocking voltage region of a power device to be roughly 10 times thinner and 10 times more heavily doped, permitting roughly a 100-fold decrease in the blocking region resistance. In addition, the high breakdown field and wide energy band gap of SiC also enable much faster power switching than is possible in comparably volt-amp rated Si power-switching devices, resulting in SiC based power converters which can operate at higher switching frequencies with much greater efficiency (i.e., less switching energy loss). Higher switching frequency in power converters is highly desirable because it permits use of smaller capacitors, inductors, and transformers, which in turn can reduce overall system size and weight. While the smaller on-resistance and faster switching of SiC help minimize energy loss and heat generation, the higher thermal conductivity enables more efficient removal of waste heat from the active device. Waste heat radiation efficiency increases greatly with increasing temperature difference between the device and the cooling ambient. Thus, the ability of SiC to operate at high junction temperatures permits much more efficient cooling to take place, so that heat-sinks and other device-cooling hardware (i.e., fan cooling, liquid cooling, air conditioning, etc.) typically needed to keep high-power devices from overheating can be made much

smaller or even eliminated.

Uncooled operation of high-temperature or high-power SiC electronics would enable revolutionary improvements in aerospace systems. Replacement of hydraulic controls and auxiliary power units with distributed “smart” electromechanical controls and sensors capable of harsh-ambient operation will lead to substantial jet-aircraft weight savings, reduced maintenance, reduced pollution, higher fuel efficiency, and increased operational reliability. SiC high-power solid-state switches will also afford large efficiency gains in electric power management and control. Performance gains from SiC electronics could enable the public power grid to meet the increased consumer electricity demand without building additional generation plants, and improve power quality and operational reliability through “smart” power management. More efficient electric motor drives, enabled by improved SiC power devices, will benefit industrial production systems as well as transportation systems such as diesel-electric railroad locomotives, electric mass-transit systems, nuclear-powered ships, and electric automobiles and buses.

Table 2.6 shows the different figures of merit (FOM) characterizing a relative advantage of a given material for various device applications. Johnson's figure of merit (JFM) [14] estimates the potential of a material for high-frequency and high-power applications:

$$\text{JFM} = \frac{E_B^2 v_s^2}{4\pi^2} \quad (2.2)$$

where  $E_B$  is the breakdown electric field and  $v_s$  is the electron saturation velocity. In terms of this figure of merit, SiC is 260 times better than Si and is inferior only to diamond.

Keyes' figure of merit (KFM) [15] is relevant to the application in integrated circuits:

$$\text{KFM} = \kappa \sqrt{\frac{c v_s}{4\pi \epsilon_r}} \quad (2.3)$$

where  $c$  is the velocity of light,  $\epsilon_0$  is the relative static dielectric constant, and  $\kappa$  is the thermal conductivity.

Baliga's figure of merit (BFOM) characterize material properties for application in high-power switches:

$$\text{BFOM} = \epsilon_r \mu E_B^3 \quad (2.4)$$

where,  $\mu$  is the electron mobility. Since all of these FOM give the different assessment of material properties, a combined dimensionless figure of merit (CFOM) was proposed by Shur et al. [16]

$$\text{CFOM} = \frac{\kappa \epsilon_r \mu v_s E_B^2}{\kappa (\epsilon_r \mu v_s E_B^2)_{Si}} \quad (2.5)$$

Although these FOMs of diamond is better than that of SiC, it is important to note that it is nearly impossible to obtain the single crystal and epitaxial film of diamond. Therefore, FOM may overestimate the potential of diamond for device application. Among wide band-gap semiconductor materials, 4H-SiC has come closer to practical applications than any other material [17]. Also GaN shows excellent physical properties. Since GaN-based blue light-emitting diodes were developed in the early 1990s, research work on GaN has been received strong efforts to realize short-wavelength laser diodes and high-frequency devices. However, some difficulties in crystal growth remained unsolved, such as a narrow doping range (especially in p-type), high density of defects in grown layers, and the lack of suitable techniques for large-area

bulk growth.

Table 2.6. Figure of merits for selected semiconductors. [99]

	$(E_B v_s)/2\pi$ ( $\times 10^{11} \text{Vs}^{-1}$ )	$(v_s/\epsilon_r)^{1/2}$ ( $\text{Wcm}^{-1/2}$ $\text{s}^{-1/2}\text{K}^{-1}$ )	JFM	KFM	BFOM	CFOM
Si	9.5	13.8	1.0	1.0	1.0	1.0
GaAs	25.0	6.3	6.9	0.456	15.7	7.36
InP	38.0	8.4	16.0	0.608		
GaN	159.2	24.3	281.6	1.76	24.6	404
6H-SiC	250.0	70.7	695.4	5.12		393
4H-SiC	289.0	76.1	932.3	5.51		404
3C-SiC	320.0	80.3	1137.8	5.81	4.4	
Diamond	859.4	444.0	8206.0	32.2	101	30080

## **2.2. SiC Epitaxial Growth**

Epitaxy comes from the greek words epi meaning on, to or above and taxis meaning order or ordering. The translation describes the growth process rather well: On top of a substrate, there are atoms placed in an ordered fashion. To improve the quality of bulk material and produce complicated device structures, these epitaxial techniques are necessary. As with other semiconductor material systems, LPE techniques and CVD were used early in the development of SiC to produce device structures. Although the crystal grown by LPE was of high quality, difficulties with molten Si used as the melt prompted the development of vapor phase techniques such as sublimation epitaxy and CVD. CVD is presently the most widely used epitaxial technique for the growth of SiC devices structures.

### **2.2.1. Chemical Vapor Deposition (CVD)**

CVD has been a successful and reliable method for epitaxial growth of SiC films on SiC and Si substrate, because CVD has the advantage of large area capability, precise interface and doping control. 6H-SiC epitaxial growth on 6H-SiC {0001} substrates by CVD has been reported since the late 1960s in the temperature range from 1500 to 1850 °C [18-22]. A significant lowering of the growth temperature and improvement of material quality have been achieved by using substrates that are misoriented a few degree off the {0001} plane toward the [11-20] direction [23,24]. This growth on misoriented

substrate has been termed "step-controlled epitaxy" and has the added advantage of stabilizing the polytype structure. Homoepitaxial CVD growth has been reported for 6H, 4H, and 3C-SiC, while heteroepitaxial growth of 3C-SiC has been reported on silicon [25,26]. Several reactor configurations have been successfully developed for the growth of SiC epitaxy. All are constructed with high temperature tolerant materials such as quartz, graphite, and SiC. Most require active water cooling. Hydrogen carrier gas along with silane and propane reagents are typically employed at atmospheric and reduced pressure and temperatures ranging from 1450 to 1600 °C. To reach these high temperatures inductively heated SiC coated graphite susceptors are employed. The most basic configuration is a cold-wall horizontal reactor, which was utilized in this thesis. The group of Davis [27] have developed the multi-wafer barrel reactor. Kordina et al [28]. have developed a hot-wall reactor for the purpose of reducing the large (20~40 kW) power requirement of the other reactors by using a hollow susceptor in an otherwise basic horizontal reactor. Most recently Rupp et al. [29] developed the single wafer rapidly rotating vertical reactor.

Karmann et al. [30] reported the unintentional incorporation of contaminants from the susceptor during SiC CVD. In these experiments, 6H-SiC layers were grown in an atmospheric pressure reactor with a growth rate of 0.7  $\mu\text{m/hr}$ . Uncoated and SiC-coated (100 to 120  $\mu\text{m}$  thick) graphite susceptors were used for comparison. For the uncoated susceptors, the layers were found to be contaminated with aluminum, boron, and nitrogen. Conversely, using an SiC-coated graphite susceptor in the same system, SiC

layers with a concentration ND-NA of  $4 \times 10^{15} \text{ cm}^{-3}$  could be grown. In a low pressure vertical reactor with high-speed substrate rotation, SiC with background concentrations in the  $10^{14} \text{ cm}^{-3}$  range was demonstrated without use of SiC-coated parts. This low amount of contamination is attributed to the favorable gas-flow patterns generated in this reactor.

#### 2.2.1.1. Principle of CVD process

The principle of the CVD process is to transport reactive compounds (precursors) by a carrier gas to a hot zone where the precursors will thermally decompose into atoms or radicals of two or more atoms which may diffuse down onto a substrate and produce an epitaxial film. In this process there are several complications that need to be understood or investigated. The precursors and carrier gas must be correctly chosen, the flow of the gases must be laminar and the material used for the hot parts of the reactor must be chosen with great care in order not to contaminate the system. In addition there are gas phase and surface reactions taking proper place.

The hydro-dynamics needs to be investigated so that the transport of the precursors is made in an accurate way. The flow must be laminar of two reasons: First, to avoid intermixing between gas compositions of two types i.e. when abrupt pn-junctions or hetero-junctions are required, fast switching between different gas compositions are needed and the intermixing in the gas phase must be kept low. Second, a turbulent flow is an efficient heat exchanger in contrast to a laminar flow. In a laminar flow the heat transport is

governed by heat conduction and convection. One may picture it as "sheets" of gas with a specific velocity that are heated or cooled by the adjacent sheets, having a different velocity. The turbulent flow does not have these sheets and a gas molecule close to a hot surface may at the next moment be in the center of the flow. The whole volume of gas will thus be uniformly heated until it reaches the temperature of the walls (if these are at the same temperature). Efficient heat exchangers always try to maintain a turbulent flow on account of the quick heat transfer. The type of flow through the reactor is largely determined by the dimensionless Reynolds number (Re):

$$\text{Re} = \frac{\bar{u}d_h}{\nu} \quad (2.6)$$

where  $\bar{u}$  is the mean velocity,  $d_h$  is the hydraulic diameter (4 times the area divided by the perimeter) and  $\nu$  is the kinematic viscosity. The hydraulic diameter  $d_h$  of a circular tube is, thus, its diameter. The relationship between the kinematic viscosity  $\nu$ , the dynamic viscosity  $\mu$  and the density  $\rho$  is given as:

$$\nu = \frac{\mu}{\rho} \quad (2.7)$$

Typically, the Re number is below 100 for the CVD process. The cross-over to turbulent flow is known to occur for a Re number at approximately 2300 [31]. The roughness of the tube surfaces and the shape of the tube have some influence and may give a cross-over point at lower Re numbers. It is, however, unlikely that turbulent flow would occur at the low Re numbers used in the CVD process. So, it is reasonable that the flow in a CVD reactor normally is assumed laminar. Mass transfer of the reactive species in the gas down on to the substrate will thus be taken care of by diffusion.

When the flow is laminar the velocity profile can easily be calculated for simple geometries such as a flow between parallel plates or flow in a circular pipe. The forces acting on a small element are viscous forces and forces due to the pressure gradient. These forces will balance since at fully developed laminar flow the velocity profile will look exactly the same at different places downstream. A particle will thus at all time travel at the same distance from the walls and at a constant speed. The pressure gradient (pressure force per unit volume) is constant along the length of the pipe or parallel plates.

In the case of CVD, the complexity increases since one or more of the walls are hot and will heat the gas passing through the tube. The physical properties of the gas will thereby change. For gases, the dynamic viscosity increases and the density decreases as the temperature increases, which means that the kinematic viscosity increases with increasing temperature. This will provide more suitable conditions for laminar flow, however, exact calculations of the flow profile will become very difficult to do manually.

It is convenient to discuss the flow close to a wall in terms of a boundary layer. The boundary layer can be illustrated as a layer over which all velocity changes occur. For a laminar flow past a semi-infinite plate the evolution of the boundary layer or the velocity profile is described by the Blasius profile:

$$\delta(x) = 4.99 \left( \frac{vx}{u_0} \right)^{\frac{1}{2}} \quad (2.8)$$

The next question is the temperature distribution of the gas phase. This problem is of considerable importance for the growth of SiC on account of the large difference in dissociation energies between the precursors. Accurate estimations of the temperature distribution involves complicated calculations

and a great deal of approximations. It can, however, be expressed by the Prandtl number (Pr):

$$P_r = \frac{\nu}{\kappa} \quad (2.9)$$

which is the ratio between the kinematic viscosity and the thermal diffusivity. The Prandtl number is thus a property of the fluid. The thermal diffusivity is expressed as :

$$\kappa = \frac{k}{\rho C_p} \quad (2.10)$$

where  $k$  is the thermal conductivity and  $C_p$  is the specific heat at constant pressure. For a gaseous medium the Prandtl number is roughly equal to unity. This implies that the thermal and velocity boundary layers are approximately the same. The question of the temperature distribution remains, however, still unanswered since it is hard to calculate the velocity boundary layer accurately.

#### 2.2.1.2. Heteroepitaxial Growth of 3C-SiC

Heteroepitaxial growth of SiC is initially motivated by lack of large inexpensive SiC substrate for homoepitaxy. Silicon wafer having a large area diameter has been mainly used as a substrate for SiC epitaxial growth. CVD growth on Si Substrates results in growth of 3C-SiC. The quality of the films depends critically on the substrate structure, orientation, and surface quality. 3C-SiC epitaxial films on (001) Si substrates, the most widely utilized substrate material, contain a variety of defects, including misfit dislocations, threading dislocations, twins, stacking faults, and antiphase boundaries

(APB's) [32]. The formation of these defects can be attributed to the following factors, including the large difference (0.08%) of the thermal expansion coefficients and lattice parameters (~20%) between 3C-SiC and Si. Despite intense research of 3C-SiC growth on Si and significant improvement in material properties, the quality of the grown 3C-SiC film is not good enough for most electronic devices. In order to improve the crystalline quality of 3C-SiC films, titanium carbide (TiC) and  $\alpha$ -SiC have been developed as an alternative substrate material. Ingots of TiC 18 mm in diameter have been successfully grown and used for SiC growth, although substrate within the ingots is difficult to remove [33]. The use of TiC substrate can result in 3C-SiC films superior in quality to films on Si substrates [34].

Growth of 3C-SiC on  $\alpha$ -SiC substrates greatly reduces problems of lattice mismatch and chemical incompatibility, resulting in lower defect densities. For example, the density of defects in 3C-SiC films can be dramatically reduced by depositing films on basal orientation substrate of 6H-SiC [35, 36]. However, defects such as DPB's generally persist because of island growth and surface defects, and it is not always possible to achieve 3C-SiC growth devoid of  $\alpha$ -SiC polytypes.

### 2.2.1.3. Homoepitaxial Growth of 3C-SiC

Studies of the homoepitaxy of 3C-SiC have been limited by the availability of bulk 3C-SiC substrate [37]. The limited literature that exists suggests that the growth of epitaxial 3C-SiC should occur at conditions similar to the

growth  $\alpha$ -SiC. Epitaxial films of (111) 3C-SiC were grown in the late sixties [38] on bulk substrates of 3C-SiC. The substrates were platelets produced by liquid-phase growth technique. The growth experiments were performed with  $\text{SiH}_4\text{-C}_3\text{H}_8$  and  $\text{CH}_3\text{SiCl}_3$  gas systems. The best results were obtained with the  $\text{CH}_3\text{SiCl}_3$  gas system. Smooth transparent films were obtained at substrate temperatures of 1560 °C. The growth rate was 2.5  $\mu\text{m/hr}$ . Background concentration Nd-Na in the layers was measured to be about  $5 \times 10^{15} \text{ cm}^{-3}$ . Another demonstration of 3C-SiC growth on 3C-SiC was reported by Yoshida et al. [39] These authors compared 3C-SiC grown on 3C-SiC material initially grown on Si and separated from the Si substrate with 3C-SiC grown on 6H-SiC substrates. It was concluded that higher growth temperatures produced films with better morphological and electrical properties. It was also determined that the 3C polytype was stable 3C-SiC substrates up to 1700 °C. Recently, the growth of 3C-SiC bulk growth [40] is also attempted by modified Lely method.

#### 2.2.1.4. Homoepitaxial Growth of $\alpha$ -SiC

Homoepitaxial growth of  $\alpha$ -SiC (6H-SiC, 4H-SiC, 15R-SiC) by CVD has been advanced at Kyoto University using off-oriented SiC substrates. This technique is called step-controlled epitaxy because the growth process is determined by the lateral growth rate of the terraces. The growth rate, substrate misorientation, and growth temperature determine whether growth will occur via the step-controlled mechanism. Step-flow growth has been one

of the very interesting subjects from a viewpoint of crystal growth. Since Burton, Cabrera, and Frank (BCF) laid the theoretical foundation on dynamics of atomic steps [41], several modification of the BCF theory [42, 43] and applications to MBE of Si [44] and GaAs [45] have been investigated. Kimoto et al. [46] reported the surface kinetics of adatoms in epitaxial growth of SiC on off-axis 6H-SiC {0001} substrates based on BCF theory.

Let's consider a simple surface diffusion model, where steps with a height  $h$  are separated by an equal distance  $\lambda_0$  as shown in Fig. 2.5. Thermally decomposed molecules in the reactor are absorbed and these adatoms diffuse on terraces toward steps. Some of the adatoms can reach steps and are incorporated into the crystal, and the others re-evaporate to vapor. Some adatoms will coalesce to form nuclei if supersaturation on terrace is high enough.

If it is assumed that the nucleation on terraces does not occur, the effective incoming flux onto the surface should be equal to the diffusion flux toward steps. Then, the continuity equation of adatoms is expressed by [46]

$$-D_s \frac{d^2 n_s(y)}{dy^2} = J - \frac{n_s}{\tau_s} \quad (2.11)$$

where  $n_s(y)$  is the number of adatoms per unit area on the surface,  $J$  the flux of reactants arriving at the surface,  $\tau_s$  the mean residence time of adatoms, and  $D_s$  the surface diffusion coefficient. Let's assume that the steps are uniform and perfect sinks for the incoming adatoms, that is, the capture probability of adatoms at steps is unity. Under the boundary condition that the supersaturation ratio  $\alpha$  ( $n_s/n_{s0}$ ) equals unity at steps:  $n_s = n_{s0}$  at  $y=\pm\lambda_0/2$ , the adatom concentration on the terraces can be given as a solution of Eq. (2.11):

$$n_s(y) = J\tau_s + (n_{s0} - J\tau_s) \frac{\cosh(\frac{y}{\lambda_s})}{\cosh(\frac{\lambda_0}{2\lambda_s})} \quad (2.12)$$

where  $n_{s0}$  is the adatom concentration at equilibrium and  $\lambda_s$  is the surface diffusion length of adatoms, which is given by the following equation [47]:

$$\lambda_s = (D_s\tau_s)^{1/2} = \exp\left(\frac{E_{des} - E_{diff}}{2kT}\right) \quad (2.13)$$

where  $a$ ,  $k$  and  $T$  are jump distance (interatomic distance), Boltzmann constant, and absolute temperature, respectively.  $E_{des}$  and  $E_{diff}$  are the activation energies for desorption and surface diffusion. This  $\lambda_s$  is an average length for adatoms to migrate on a "step-free" surface before desorption.

The flow of adatoms in the  $y$  direction  $J_s(y)$  is given by [47]

$$J_s(y) = -D_s \frac{dn_s(y)}{dy} = \lambda_s \left( J - \frac{n_{s0}}{\tau_s} \right) \frac{\sinh(\frac{y}{\lambda_s})}{\cosh(\frac{\lambda_0}{2\lambda_s})} \quad (2.14)$$

Since the capture probability of migrating adatoms at steps is assumed to be unit, the step velocity  $v_{step}$  is given by the following equation using the  $J_s(y)$  at steps ( $y = \lambda_{s0}/2$ ):

$$v_{step} = 2 \left. \frac{J_s(y)}{n_0} \right|_{y=\lambda_0/2} = \frac{2\lambda_s}{n_0} \left( J - \frac{n_{s0}}{\tau_s} \right) \tanh\left(\frac{y}{2\lambda_s}\right) \quad (2.15)$$

Here,  $n_0$  is the density of adatom sites on the surface, and migrating adatoms from both the left and right sides of steps are considered. In step-flow growth, the growth rate ( $R$ ) is calculated by the product of the step velocity and  $\tan\theta$  ( $=h/\lambda_0$ ), where  $\theta$  is the off-angle of a substrate. Thus, the following equation is satisfied:

$$R = \frac{2h\lambda_s}{n_0\lambda_0} \left( J - \frac{n_{s0}}{\tau_s} \right) \tanh\left(\frac{\lambda_0}{2\lambda_s}\right) \quad (2.16)$$

Figure 2.6 shows the distribution of adatom concentration and the

supersaturation ratio ( $\alpha$ ) on a surface. Since  $\alpha$  has a maximum value  $\alpha_{\max}$  at the center of a terrace, nucleation occurs most easily at this position. Based on Eqs. (2.14) and (2.18),  $\alpha_{\max}$  can be expressed by

$$\alpha_{\max} = 1 + \frac{\lambda_0 n_0 R}{2\lambda_0 h} \frac{\tau_0}{n_{s0}} \tanh\left(\frac{\lambda_0}{4\lambda_s}\right) \quad (2.17)$$

The  $\alpha_{\max}$  depends on experimental conditions such as growth rate, growth temperature, and terrace width. This  $\alpha_{\max}$  is an essential parameter that determines whether the growth mode is step-flow or two-dimensional nucleation. Since a two-dimensional nucleation rate  $J_{\text{nuc}}$  increases exponentially with the supersaturation ratio on a surface, nucleation becomes significant when  $\alpha_{\max}$  exceeds a critical value  $\alpha_{\text{crit}}$ . Thus, the growth modes are determined according to the relationship between  $\alpha_{\max}$  and  $\alpha_{\text{crit}}$  as follows:

$\alpha_{\max} > \alpha_{\text{crit}}$  : two-dimensional nucleation,

$\alpha_{\max} < \alpha_{\text{crit}}$  : step-flow.

Under the critical condition, the following equation is satisfied:

$$\alpha_{\max} = \alpha_{\text{crit}}$$

Using Eq. (2.19), the above equation can be rearranged as

$$\frac{\lambda_0}{4\lambda_s} \tanh\left(\frac{\lambda_0}{4\lambda_s}\right) = \frac{(\alpha_{\text{crit}} - 1) n_{s0}}{2n_0 R} \frac{1}{\tau_s} \quad (2.18)$$

In Eq. (2.20),  $R$  and  $\lambda_0$  are determined by growth condition, and  $n_0$  and  $h$  are inherent parameters of a material. If the values of  $n_{s0}/\tau_s$  and  $\alpha_{\text{crit}}$  are known,  $\lambda_s$  can be calculated from Eq. (2.20). Then, by finding out the critical condition experimentally, the surface diffusion length can be estimated. A critical growth rate can be calculated by Eq. (2.18) if the growth temperature and off-angle of substrates are fixed. Kimoto et al. [46] calculated critical

growth conditions for various off-angle of substrate as shown in Fig. 2.7. As shown, the higher growth rate and lower off-angle are available for step-flow growth at higher growth temperatures.

In 1986 to 1987, Matsunami group [24] and Davis group [25] reported the 6H-SiC epitaxial growth on off-axis 6H-SiC {0001} substrate at low temperatures of 1500 °C, independently. This technique is named "step-controlled epitaxy", because the polytype of epilayer can be controlled by the exposed step sequence of off-axis substrate. Hence, the polytype mixing problem in CVD growth was solved by using off-axis substrate. Today, device-quality SiC epitaxial films have been produced by this technique.

In SiC growth, the step flow results in homoepitaxial growth while the two-dimensional nucleation leads to growth of twinned crystalline 3C-SiC, which is stable at low temperature ( $< 1500$  °C). In the case of two-dimensional nucleation, the growing 3C-SiC can take two possible stacking sequence of ABCABC... and ACBACB..., shown in Fig. 2.8, leading to double positioning boundary (DPB). To enhance step flow, the step density and terrace width should be large and small, respectively. This is the reason why several degree off-axis substrate is used for homoepitaxy of SiC. The technique of step-controlled epitaxy is utilized for growth of 6H-SiC, 4H-SiC, and 15R-SiC.

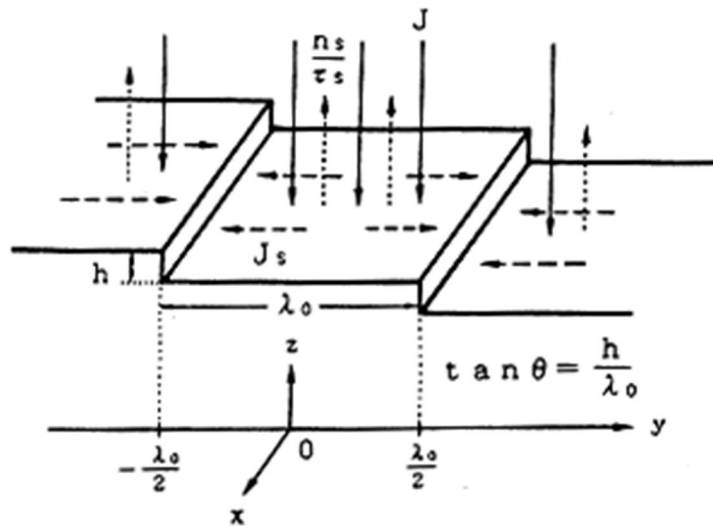


Fig. 2.5. Schematic illustration of simple surface diffusion model, where steps with a height  $h$  are separated by an equal distance. [46]

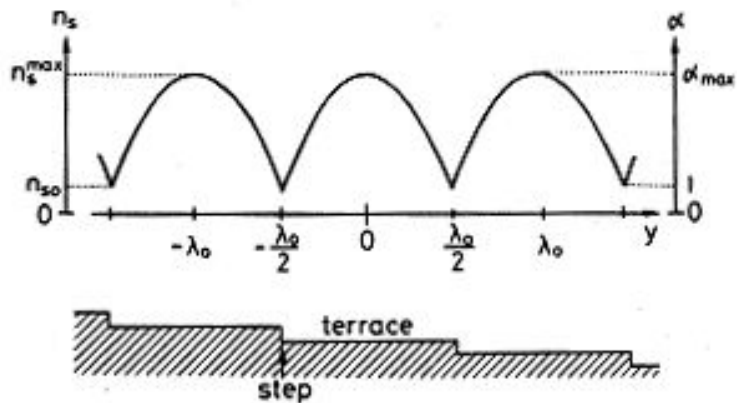


Fig. 2.6. The distribution of adatom concentration and supersaturation ratio  $\alpha$  ( $= n_s/n_s0$ ) on off-axis surface. [46]

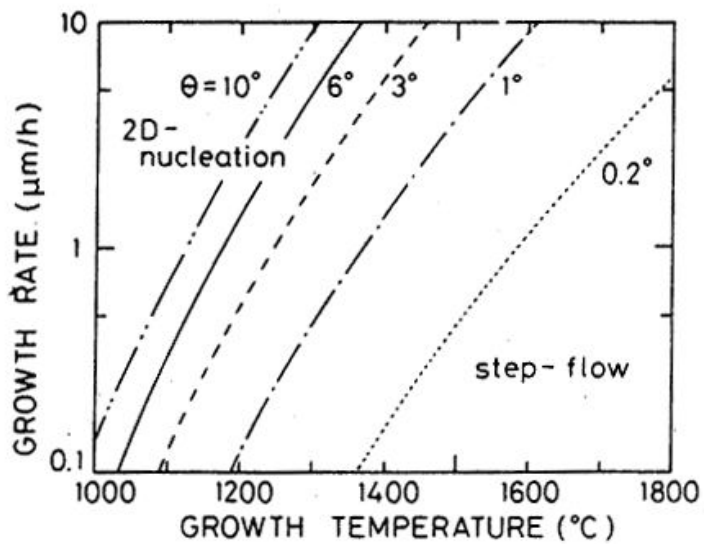


Fig. 2.7. Critical growth conditions as a function of growth temperature, growth rate, and off-angles of the substrate ( $\theta= 0.2^\circ, 1^\circ, 3^\circ, 6^\circ,$  and  $10^\circ$ ). The top-left and bottom-left regions from the curves correspond to two-dimensional nucleation and step-flow growth conditions respectively. [46]

### 2.2.1.5 Structural Properties of $\alpha$ -SiC

The surface of SiC epitaxial layers can contain a large number of imperfections. Surface defects observed in SiC CVD layers are growth pits, polytype inclusions (which sometimes appear as triangular features), macrosteps (often referred to as step bunching), and micropipes. Some of these defects are relatively large (tens of microns), while others have an average size of less than 1  $\mu\text{m}$ . Attempts to understand the nature of surface defects in SiC CVD layers have appeared in several studies [48-54]. A large number of factors influence the production and density of surface defects. These include substrate characteristics (orientation, face polarity, tilt angle, crystallographic direction of the misorientation), mechanical and chemical treatment of the substrate before the epitaxy, substrate pregrowth treatment in the reactor (hydrogen etching process), and growth conditions such as Si/C ratio, growth rate. Growth pits are a common morphological defect observed in the growth of SiC. The relationship between growth pits on the epitaxial layer and surface imperfections in the starting substrates has been studied by Powell et al. [50] It was concluded that main factor in the formation of growth pits is the polishing and preparation of the substrate rather than bulk defects such as micropipes, and dislocations. This conclusion has led to improved substrate polishing techniques, such as the use of colloidal silica for

chemomechanical polishing [55]. Step bunching (which is the combination of atomic steps on the surface to form large macrosteps) often occurs in the CVD growth of SiC. Results on the initial investigations of step bunching on 6H-SiC epitaxy was discussed by Kong et al [56].

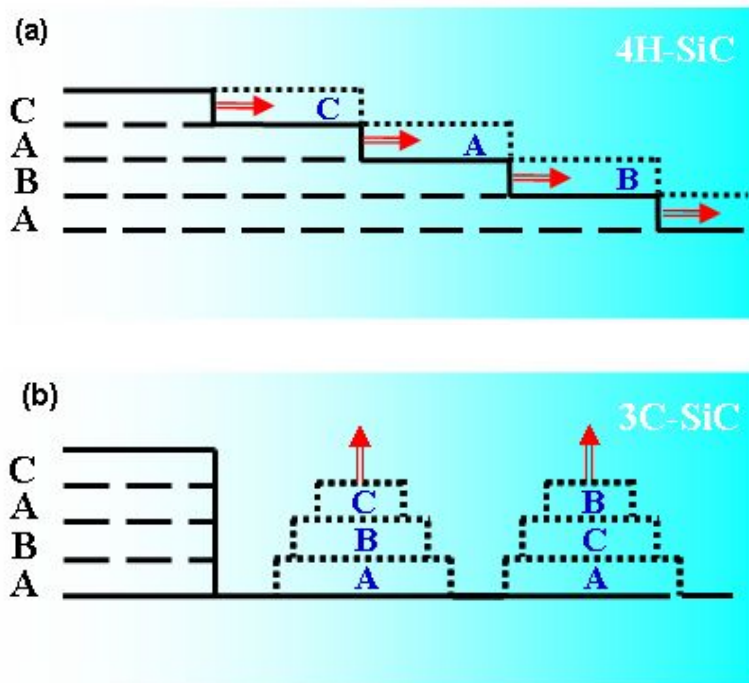


Fig. 2.8. Schematic images of the relationship between growth modes and polytypes of grown layers. Homoepitaxy of 4H-SiC is achieved owing to step flow growth (a), and 3C-SiC is grown through two-dimensional nucleation (b).

Step bunching in 6H- and 4H-SiC growth by step-controlled CVD on misorientated  $\{0001\}$  substrates was investigated by AFM and TEM techniques [49].

Typical 4H- and 6H-SiC epitaxial layers also contain dislocations and micropipes. In all cases in which micropipes were observed at a layer-substrate interface, the micropipes originated in the substrate and propagated into the epitaxial layer. This result implies that if micropipes in the substrate are eliminated or closed, the epitaxial films will be micropipe-free.

Polytype inclusions are a common type of crystalline defect in 6H- and 4H-SiC epitaxial layers grown by CVD. These polytype inclusions (usually 3C-SiC) are formed due to nucleation on terraces or dislocation sites. It was found that with proper pregrowth surface treatment with HCl etching, 6H-SiC layers without 3C-SiC inclusions can be grown by CVD on  $\{0001\}$  6H-SiC substrates with small tilt angles. The etching process appears to be effective in removing unintentional 3C nucleation sites on 6H-SiC wafer. However, deviation from the optimal etching conditions led to 3C-SiC growth on the 6H-SiC substrates. It was also found that 4H-SiC homoepitaxial layers are more susceptible than 6H layers to 3C inclusion [50]. The mechanism of cubic SiC nucleation on off-axis 6H and 4H substrates has been investigated by Hallin et al [57]. These investigators showed that the 3C-SiC nucleation occurs via the formation of triangular stacking faults at substrate

imperfections. In 6H-SiC, these defects are usually found in on-axis material where the probability for two-dimensional nucleation of 3C-SiC is increased. In 4H-SiC epitaxial layers, 3C-SiC inclusions having a triangle shape are found even if substrates have a tilt angle of  $3.5^\circ$  [58]. To reduce the density of inclusions in 4H material, an  $8^\circ$  tilt angle was found to be necessary. In the 4H-SiC epitaxial layers grown  $8^\circ$  off-axis substrates, the 3C-SiC inclusions are almost eliminated.

Although some progress has been made in understanding the nature and cause of structural defects such as step bunching and polytype inclusions, the origin and control of many defects in epitaxial SiC remain to be investigated.

#### 2.2.1.6 Growth Equipment and Precursor Materials for CVD

Three types of typical growth apparatus are used for SiC CVD. (1) Cold-wall horizontal atmospheric pressure reactors have been used for many years. This system uses low pressure and a specially designed inner susceptor to maintain laminar gas flow. (2) Hot-wall horizontal atmospheric pressure reactors have been designed at Linköping University [59]. (3) Cold-wall vertical low-pressure reactors have been built commercially and used. In this reactors, laminar flow is obtained by a high-speed rotating disk (in conjunction with high gas-flow velocities), which produces a pumping action.

High temperatures in SiC epitaxial reactors can be obtained with rf heating. In most systems, the susceptor is made from graphite and coated with SiC because of the reaction between graphite and  $H_2$  at temperatures in excess of

1300 °C. Unintentional incorporation of contaminants from the susceptor during SiC CVD was studied by Karmann and co-workers [60]. In a low-pressure vertical reactor with high-speed substrate rotation, SiC with background concentration in the  $10^{14}$  cm<sup>-3</sup> range was demonstrated without use of SiC-coated parts [53]. This low amount of contamination is attributed to the favorable gas-flow patterns generated in this reactor.

Temperature measurement is a major equipment issue for CVD growth at high temperatures. During growth, substrate temperature is usually measured by optical pyrometer calibrated by melting of Si or Ge. The temperature of the susceptor typically is found to be 50 to 100 °C higher than that of the SiC substrate.

A number of precursors have been used for the growth of SiC. For transport of the Si species, the most popular choice is SiH<sub>4</sub>, along with Si<sub>2</sub>H<sub>6</sub> [61] and SiCl<sub>4</sub> [62] which have also been used. For growth of SiC, the hydrocarbon species most reported is C<sub>3</sub>H<sub>8</sub>. However, there are also reports of SiC growth using C<sub>2</sub>H<sub>2</sub> [63], CH<sub>3</sub>Cl [64], CH<sub>4</sub> [65] as carbon sources. In the case of 3C-SiC heteroepitaxial growth on silicon, single precursor materials such as methyltrichlorosilane (MTS) [66], silacyclobutane (SCB) [63], hexamethyldisilane (HMDS) [67, 68], methylsilane [69], and BTMSM [65] to reduce the deposition temperature. However, in the case of homoepitaxial growth for 4H-SiC and 6H-SiC, there is no systematic investigation using single precursor material. In this thesis, BTMSM source material was used for the 4H-SiC homoepitaxial growth.

### **2.3. SiC Doping**

Wide band-gap materials are difficult to dope due to the large ionization energies and self-compensation effects of most substitutional impurities. Fortunately, in the case of SiC, an excellent donor atom (nitrogen) exists and a workable acceptor atom (aluminum) also exists. Progress in SiC technology has resulted in a wide doping range for both n- and p-type conductivity. The three doping techniques are doping during growth, diffusion, and ion implantation.

Impurities for SiC doping have been found for: (1) donors (mainly nitrogen), (2) acceptors (mainly aluminum), and (3) deep-level impurities to form semi-insulating material (practically vanadium). Recently, Er was introduced in SiC and preliminary results for IR emission [70] look promising. There have been few attempts to study isoelectronic traps in SiC, but the subject requires further investigation. The doping development for SiC is complicated because the doping process depends not only on the surface orientation, doping technology, and doping concentration, but also on polytype structure. So, the information on impurity properties in SiC is limited even for impurities such as nitrogen and aluminum.

### 2.3.1. Site-competition Epitaxy

In 1993, Larkin et al. [71] demonstrated a dependence of dopant incorporation efficiency on input Si/C ratio (analogous to the impact of III/V ratio in that compound semiconductor family [72]) helping to both reduce background doping density and extend the range of intentional doping into epilayers. So-called site-competition epitaxy has been used for the control of nitrogen, phosphorus, aluminum, and boron incorporation in 6H-SiC and 4H-SiC films. For example, in the case of nitrogen doping, the growth under a higher C/Si ratio leads to the lower N concentration in the epilayers. This phenomenon can be explained by the fact that the higher C atom coverage on a growing surface prevents the incorporation of N atom, which substitute at the C site, into crystal.

Impurity memory effect on dopant concentration profiles in 4H- and 6H-SiC were investigated by SIMS [73]. It was found that dopants were absorbed by the reactor walls and re-evaporated after the dopant precursor flow was switch off. These memory effects limit the doping control range to about three orders of magnitude for aluminum and two orders of magnitude for boron. The dynamic range for Al doping was increased up to five orders of magnitude by controlling the Si/C ratio and using HCl etching during the 10 min growth interruption after gas switching. For boron, a dynamic range of more than three orders of magnitude was obtained. Doping spikes between the substrate and epilayer were also reduced by an in-situ HCl etch [74].

### **2.3.2. Diffusion of Impurities in SiC**

Impurities diffusion is one of the principal methods of doping. Although the effective diffusion coefficients for most of the major impurities in SiC is too small for practical applications, it is nevertheless important to understand diffusion process in SiC, as these processes may take place during bulk and epitaxial growth, as well as during heat treatments. Diffusion coefficients for different impurities in 6H-SiC are shown in Fig. 2.9 [75]. Boron and aluminum diffusion has been used for SiC device fabrication. Boron diffusion has produced yellow and green [76] light-emitting diodes, while field effect transistors were fabricated by aluminum diffusion [77].

### **2.3.3. Ion Implantation**

Ion implantation is a materials engineering process by which ions of a material can be implanted into another solid, thereby changing the physical properties of the solid. Ion implantation is used in semiconductor device fabrication and in metal finishing, as well as various applications. Especially, Ion implantation is the only technique for the selective doping and is widely used in SiC device technology. Ion implantation has been used for: (1) p-n junction formation [78], (2) light emitting diode fabrication [79], (3) highly doped contact layers [80, 81], (4) field effect transistor channels [82], and (5) device isolation and termination [83]. Ion-implanted dopant activation is achieved by thermal annealing using resistively or rf-heated furnaces [84].

Excimer laser activation has also been reported [85]. Simulation of implantation profiles in SiC and their comparison with experimental results have been performed [86].

N-type doping by ion implantation has been developed into a production process. Annealing of nitrogen implantation has, in general, resulted in low residual damage due to the small size of nitrogen atom. Nitrogen ion implantation is usually performed in 6H-SiC at elevated temperatures. Annealing at 1500 and 1600 °C for 15 min, performed in SiC crucibles, results in Rutherford back-scattering yields at the virgin crystal level, indicating a good recovery of the crystalline quality. Recently, activation process of high-dose ( $3.8 \times 10^{15}$  and  $7.1 \times 10^{15}$  cm<sup>-2</sup>) nitrogen implants into 6H-SiC have been investigated [87]. It was shown that low resistivity of the implanted material can be obtained after long-time (2000 min) anneals at 900 °C.

One of the current problem in ion implantation technology is activation of the p-type dopants. Because Al is a large atom, higher annealing temperatures and times are required to produce device-quality p-type layers [88]. Amorphization and recrystallization of Al-implanted 6H-SiC were investigated [89]. Ion implantation was performed in n-type 6H-SiC in the temperature range of room temperature to 1000 °C. Aluminum ions were implanted with a dose range of  $5 \times 10^{13}$  to  $5 \times 10^{16}$  cm<sup>-2</sup> and implant energies of 180 and 360 keV into 6H-SiC epitaxial layers having doping concentration of  $1 \times 10^{16}$  cm<sup>-3</sup>. After implantation, the samples were annealed between 800 and 1600 °C for 30 min in an Ar flow. It was shown that density of defects

induced by implantation decreased exponentially with increasing implantation temperature. However, residual defects were detected even after annealing at 1600 °C. At a 1600 °C anneal temperature sublimation of SiC was observed. Carrier concentration and mobility were found to be independent of the implantation temperature, and the carrier concentrations at room temperature were measured to be about 5% of implanted dopant. The measured hole mobility was less than 1 cm<sup>2</sup>/Vs (300 K). Annealing p-type implants at lower temperatures has proven ineffective. For example, annealing at 1400 °C [90] resulted in a hole concentration of 5×10<sup>17</sup> cm<sup>-3</sup>. Also, C or Si co-implantation also did not improve Al activation efficiency [91]. Experimental data on ion implantation in other than the 6H polytype are limited.

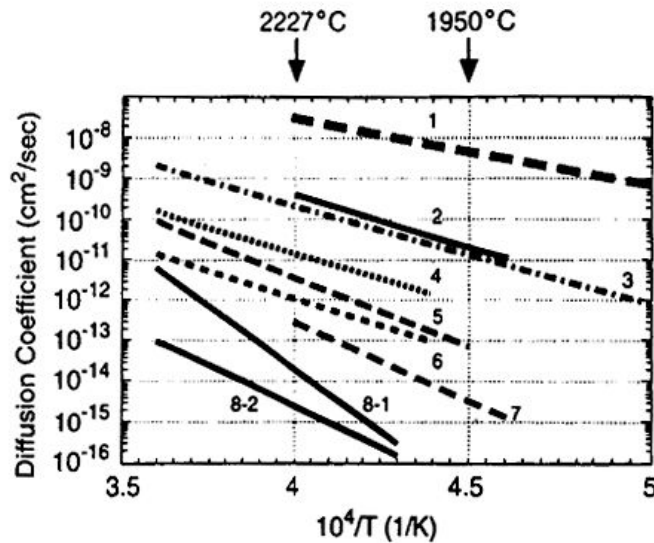


Fig. 2.9. Diffusion coefficients for different impurities in 6H-SiC. [1:Be (bulk

diffusion), 2: Be (diffusion in the surface region), 3: B (Bulk diffusion), 4: B (diffusion in the surface region), 5: Al, 6: Ga, 7: oxygen, 8-1 and 8-2: nitrogen] [75]

## 2.4. Step Kinetics on Vicinal Surface

Step bunching in 4H-SiC homoepitaxial growth is widely investigated because the use of off-axis substrate in 4H-SiC epitaxy. Micro-step bunching is well explained by surface energy minimization by Kimoto et al. [46], but macro-step bunching is still not well explained. Here the step kinetics during film growth could be a clue for the behavior of macro-step bunching because macro-step bunching during 4H-SiC epitaxy is affected by process parameters. The step kinetics on vicinal surface is quoted from Ki-Ha Hong's Ph. D. Thesis [92]. Step bunching is famous unstable step structure appeared during growth of vicinal surface. Though many origins, the lattice strain effects and diffusion asymmetric kinetics at step-edge is introduced.

The theory of the growth of a stepped surface by molecular beam epitaxy (MBE) was devised by Burton, Cabrera and Frank [47]. Considering the growth by MBE of an infinite vicinal surface, formed by terraces of high-symmetry orientation separated by parallel, equidistance steps, following diffusion equation can be obtained.

$$\frac{\partial \eta}{\partial t} = D \frac{d}{dx^2} \eta + F \quad (2.19)$$

$\eta$  is adatom density per unit site,  $D$  is adatom diffusion coefficient, and  $F$  is adatom flux. In this study, we consider step flow growth mode and the atom diffusion is generally much faster than step motion in this case. Therefore, it is a good approximation to neglect time derivative of  $\eta$ . This is called quasi-static approximation [93].

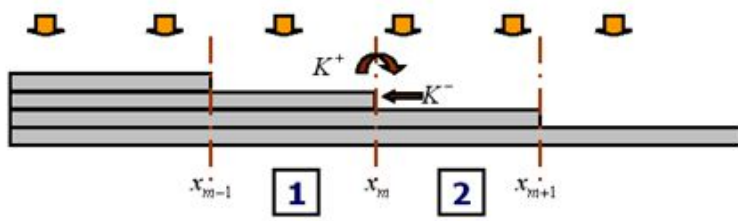


Fig. 2.10. One dimensional picture of the step flow growth. Region 1 indicate upper terrace region and region 2 indicates lower terrace region.  $K^-$  and  $K^+$  is kinetic coefficient influencing asymmetric kinetics at step edge. [94]

At region 1 in Fig. 2.10, the governing equation for adatom concentration is

$$D \frac{d}{dx^2} \eta + F = 0$$

and the boundary conditions are:  $D \frac{d\eta}{dx} \Big|_{x_{m-1}^+} = K^- (\eta - \eta_0(x_{m-1}))$  at  $x_{m-1}$  and  $-D \frac{d\eta}{dx} \Big|_{x_m^-} = K^+ (\eta - \eta_0(x_m))$  at  $x_m$ , which comes from assumption of that diffusion flux at step-edge is proportional to difference between adatom density  $\eta$  and equilibrium density  $\eta_0$  at step-edge.  $K^-$  and  $K^+$

is kinetic coefficient influencing asymmetric kinetics at step edge. In the absence of ES barrier,  $K^- = K^+ = \infty$ , and this is also assumed by Tersoff et al. [94]

At region 2, the governing equation is also

$$D \frac{d}{dx^2} \eta + F = 0$$

And the boundary conditions are:  $D \frac{d\eta}{dx} \Big|_{x_m^+0} = K^- (\eta - \eta_0(x_m))$  at  $x_m$

and at  $x_{m+1}$ .

Then, the velocity of the  $m$ th step becomes

$$v_m = D \left[ \frac{d\eta}{dx} \Big|_{x_m^+0} - \frac{d\eta}{dx} \Big|_{x_m^-0} \right] \quad (2. 20)$$

If one knows the adatom density at the  $m$ th step, velocity of the each step can be determined by the Eq. (2.20). There are two factors to affect the adatom density at  $m$ th step. One is the adatom formation energy from at step ( $E_1$ ) and the other is elastic force exerted on a step ( $f_m$ ). There are two kinds of elastic interactions between steps [95]. The one is monopole force induced by bulk stress. In a strained layer, the lateral force from the strained material on one side of the step is not balanced by and equal force from the other side. This force attracting steps of which direction normal is same. The other is dipole force induced by the intrinsic strain due to asymmetric neighborhood at step edge. Dipole force repels steps with each other. Elastic force exerted on step  $m$  is expressed as follows:

$$f_m = \sum_{n \neq m} \left( \frac{\alpha_1}{(x_n - x_m)} - \frac{\alpha_2}{(x_n - x_m)^3} \right) \quad (2. 21)$$

Where  $\alpha_1 = \sigma_2 h_2 / M$ ,  $M$  being an elastic constant and  $\alpha_2$  is the strength of

dipole,  $x_m$  is the position of the  $m_{th}$  step in the direction perpendicular to the steps. The first term represents monopole-monopole interaction induced by lattice strain and this term generates attractive force between steps of which direction normal is same. The second term makes repulsion force between steps. Then equilibrium adatom concentration can be expressed as follows [94]:

$$\eta_0(x_m) = \eta_e e^{-f_m A/kT} \quad (2.22)$$

$E_1$  is the formation energy of an adatom (the energy to dissociate an adatom from a step) and  $A$  is the area per surface site. Inserting Eq. (2.22) and boundary condition into Eq. (2.20), one can obtain following step velocity equation.

$$v_m = v_m^k + v_m^E \quad (2.23)$$

Where

$$v_m^k = \frac{F\left\{\frac{D}{K^+}x_{m+1} + \frac{D}{K^-}x_m + \frac{1}{2}(x_{m+1}^2 - x_m^2)\right\}}{\frac{D}{K^+} + \frac{D}{K^-} + (x_{m+1} - x_m)} - \frac{F\left\{\frac{D}{K^+}x_m + \frac{D}{K^-}x_{m-1} + \frac{1}{2}(x_m^2 - x_{m-1}^2)\right\}}{\frac{D}{K^+} + \frac{D}{K^-} + (x_m - x_{m-1})} \quad (2.24)$$

And

$$v_m^E = -\frac{D\eta_0 A}{kT} \left\{ \frac{f_{m+1} - f_m}{P + (x_{m+1} - x_m)} - \frac{f_m - f_{m-1}}{P + (x_m - x_{m-1})} \right\} \quad (2.25)$$

Where

$$P = \frac{D}{K^+} + \frac{D}{K^-} \quad (2.26)$$

With Eq. (2.23), we can analyze step dynamics under stress within step flow regime and the step structure change during step flow growth will be shown.

The existence of bunching instability can be determined by linear stability analysis that perturbing the steps from their initial equidistant positions and calculating the linear response. Let  $u_m(t)$  denote the deviation of the step from the position it would have under ideal step flow, i.e.,

$$u_m(t) = x_m(t) - L_{av}(m + Ft) \quad (2.27)$$

where  $L_{av}$  is the average step separations. For a perturbation of amplitude  $\Delta$  and period  $N$  steps, we substitute  $u_m(t=0) = \Delta \cos(2\pi m/N)$  into Eq. (2.23) and integrate the velocity. Resulted fluctuation for small intervals within first order in  $\Delta$  is

$$u_m(t) \approx e^{rt} \Delta \cos(km + \Xi(t)) \quad (2.28)$$

where  $\Xi(t) = Ft [P^2 + L_{av} (2P + L_{av})] \sin k / (P + L_{av})^2$ .

$r$  is defined as follows within linear stability.

$$r = \left(1 - \cos \frac{2\pi}{N}\right) \left[ B \frac{\alpha_1}{L_{av}^3} \frac{4\pi^2}{N^2} (N-1) - B \frac{4\alpha_2\pi^4}{L_{av}^5 N^4} (N-1)^2 - \frac{F \left[ \left( \frac{D}{K^+} \right)^2 - \left( \frac{D}{K^-} \right)^2 \right]}{(P+L_{av})^2} \right] \quad (2.29)$$

where,  $B = \frac{DA}{2kT} e^{-E_1/kT} N$  is period of the sinusoidal perturbation. If  $r > 0$ , the perturbation will be amplified and it means that there are step bunching instability. Though Tersoff et al's model [94] is only valid in the condition that  $N$  is very large, this model is valid for whole range of  $N$  and moreover, this model contains the effect of surface kinetics. The first term within a brace in Eq. (2.29) cannot be minus value, only second term surrounded with bracket determines the sign of  $r$ . There are three terms determining step bunching instability in the bracket. The first term in the bracket is related with the

monopole interaction and this promotes bunching instability. The second is related with dipole interaction and this stabilizes equidistant step structure. The third is originated from ES barrier and this can make several interesting phenomena. For normal ES barrier,  $D / K^+$  has finite value because it needs excess energy for interstep diffusion and  $D / K^-$  becomes almost '0'. In this case, the third term has positive value and hinders step bunching instability. This term is closely related with flux which is expected to stabilize step flow growth in this case. But there was a report on a possibility of inverse ES barrier for homoepitaxy on Si (0001). Inverse ES barrier means that there are excess energy barrier of adatom attachment to step edge from terrace [95]. In the case of inverse ES barrier, the third term has negative value and adatom flux can promotes step bunching which are opposite with normal ES barrier condition. This model has important physical meaning in points of that it can analyze competition between elastic interaction and interstep diffusion kinetics and also predicts the kinetic bunching induced by inverse ES barrier.

There are so many factors to determine the growth characteristics. Eq. (2.29) says that step bunching can be affected by step-step interaction, average step distance (miscut angle), flux, ES barrier and temperature. Energy configuration of normal ES barrier and inverse ES barrier is plotted in Fig. 2.11.

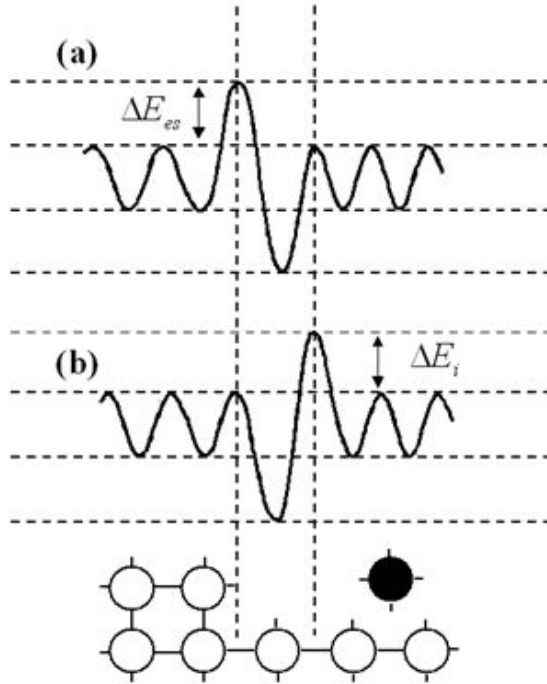


Fig. 2.11. Model potential for adatoms near a step edge. (a) Normal and (b) inverse ES barrier. [95]

## 2.5. SiC Power Device Application

SiC can withstand a voltage gradient (or electric field) over eight times greater than Si or GaAs without undergoing avalanche breakdown. This high breakdown electric field enables the fabrication of very high voltage, high-power devices such as diode, power transistors, power thyristors and surge suppressors, as well as high power microwave devices. [13,14,99] Additionally, it allows the devices to be placed very close together, providing high device packaging density for integrated circuits (Fig. 2.12). SiC is an excellent thermal conductor (SiC possess high thermal conductivity). Heat will flow more readily through SiC than other semiconductor materials. In fact, at room temperature, SiC has a higher thermal conductivity than any metal. This property enables SiC devices to operate at extremely high power levels and still dissipate the large amounts of excess heat generated. The high saturated electron drift velocity explain why SiC devices can operate at high frequencies (RF and microwave).

Power semiconductor devices are a critical element of smart power electronics technology. Today, utilities generate on average 20% more electricity than is consumed at any given time. This excess power reserve is needed to ensure that electric service is reliably immune to everyday load changes and component failures that cause electrical glitches throughout the power grid. The incorporation of solid state smart power electronics into the power grid should significantly reduce the power reserve margin necessary for compensate for local glitches. It has been estimated that a mere 5% reduction

in power reserve margin would eliminate the need for \$ 50 billion worth of new power plants within the next 25 years. This same smart power technology would also enable as much as 50% larger power capacities to be carried over existing power lines. Presently, these devices are all implemented in conventional silicon based semiconductor technology. The faster switching speed not only increases conversion efficiency of power system, but it also enables the use of smaller transformers and capacitors to greatly shrink the overall size and weight of the system. Furthermore, the high temperature capability of SiC greatly reduces cooling requirements that are also a substantial portion of the total size and cost of a power conversion and distribution system (Fig. 2.13). Recent developments in SiC device technology have opened up the hybrid electric vehicles or the fuel cell electric vehicle for SiC based power electronics, where these devices could be utilized for substantial weight savings and enhanced electric vehicles performance (Fig. 2.14) [98]. SiC devices are therefore expected to drastically improve the distribution and efficient usage of electric power in the 21<sup>st</sup> century.

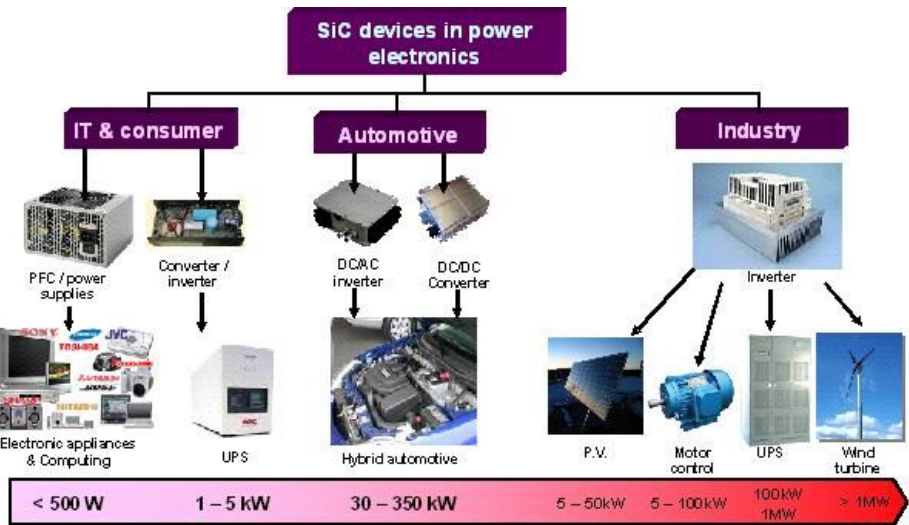


Fig. 2.12. Schematic of SiC high power electronic devices. [96]

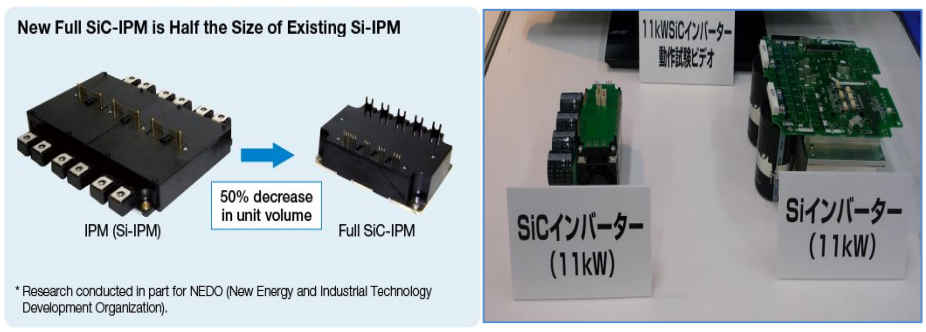


Fig. 2.13. Comparison SiC-IPM with Si IPM. [97]

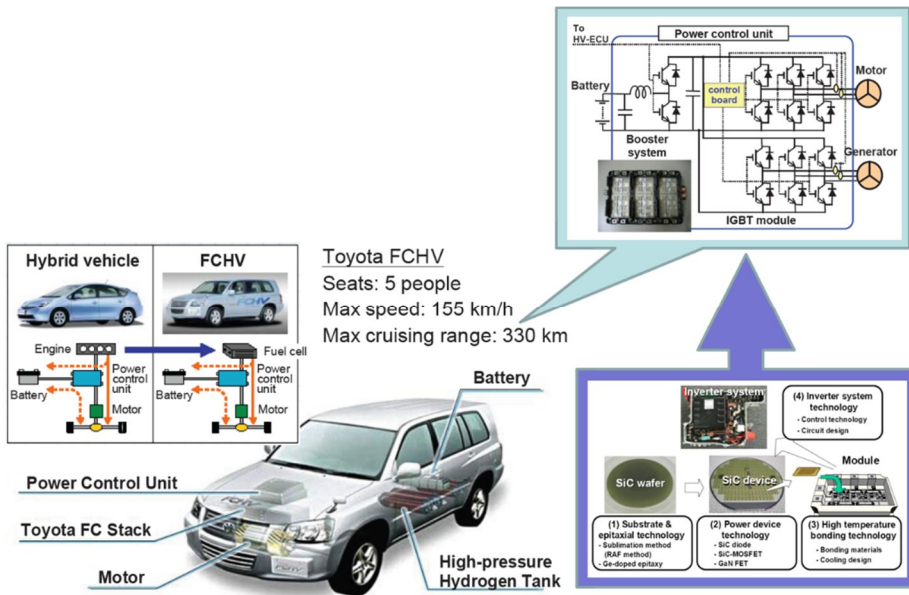


Fig. 2.14. Schematic of SiC high power electronics devices for Toyota's HEV (Hybrid electric Vehicle), FCEV (Fuel Cell Hybrid Vehicle). [98]

## Bibliography

- [1] A. R. Verma, Ed. P. Krishna, *Polymorphism and Polytypism in Crystals*, Wiley, New York (1966).
- [2] J. A. Powell, D. J. Larkin, L. G. Matus, W. J. Choyke, J. L. Bradshaw, L. Henderson, M. Yoganathan, J. Yang, and P. Pirouz, *Appl. Phys. Lett.* 56 (14), 1353 (1990).
- [3] G. R. Fisher and P. Barnes, *Phil. Mag. B* 61, 217 (1990).
- [4] L.S. Ramsdell, *Amer. Mineral.* 32, 64 (1947).
- [5] P. Kackell, B. Wenzien, and F. Bechstedt. *Phys. Rev. B* 50, 17037 (1994).
- [6] F. Bechstedt, P. Kackell, A. Zywietz, K. Karch, B. Adolph, K. Tenelsen, and J. Furthmuller. *Phys. Stat. Sol. (b)* 202, 35 (1997).
- [7] R. F. Adamsky and K. M. Merz, *Z. Krist.* 111, 350 (1959).
- [8] Landolt-Bornstein: Numerical Data and Functional Relationships in Science and Technology, Vol. 17a, new Series, Ed. K. H. Hellwege and O. Madelung, Spring-Verlag, Berlin (1982).
- [9] A. Bauer, J. Krausslich, L. Dressler, P. Kuschnerus, J. Wolf, K. Goetz, P. Kackell, J. Furthmuller, and F. Bechstedt, *Phys. Rev. B.* 57, 2647 (1988).
- [10] J. B. Casady and R. W. Johnson, *Solid-state Electron.* 39, 1409 (1996).
- [11] Y. S. Park, *SiC Materials and Devices*, Academic press, San Diego (1998).
- [12] A. Taylor, and R. M. Jones, in *Silicon Carbide - A High Temperature Semiconductor*, Eds. J. R. O'Connor and J. Smiltens, Pergamon Press: Oxford. p.147 (1960).
- [13] R. B. Campbell, *IEEE Trans. Indus. Electron.* IE-29, 124 (1982).

- [14] E. O. Johnson, RCA Rev. 26, 163 (1965).
- [15] R. W. Keyes, Proc. IEEE 60, 225 (1972).
- [16] M. S. Shur, SiC Transistor- SiC Materials and Devices, Eds. Y. S. Park, Academic Press p.161 (1998).
- [17] M. Shur and A. Khan, GaN based field transistors, in "High Temperature Electronics", Eds. M. Willander and H. Hartnagel, Chapman, London (1996).
- [18] R. B. Campbell, and T. L. Chu, J. Electrochem. Soc. 113, 825 (1966).
- [19] V. L. Jennings, A. Sommer, and H. C. J. Electrochem. Soc. 113, 728 (1966).
- [20] J. T. Kendall, J. Chem. Phys. 21, 821 (1953).
- [21] H. Matsunami, S. Nishino, M. Odaka, and T. Tanaka, J. Cryst. Growth 31, 72 (1975).
- [22] S. Minagawa, and H. C. Gatos, Jpn. J. Appl. Phys. 10, 1680 (1971).
- [23] H. S. Kong, J. T. Glass, and R. F. Davis, J. Appl. Phys. 64, 2672 (1988).
- [24] H. Matsunami, K. Shibahara, N. Kudora, and S. Nishino, in Amorphous and Crystalline Silicon Carbide, Eds. G. L. Harris and C. Y. Yang (Springer-Verlag, Berlin, Heidelberg, p.34-39 (1989)
- [25] H. J. Kim and R. F. Davis, J. Appl. Phys., 60, 2897 (1986).
- [26] H. J. Kim and R. F. Davis, J. Electrochem. Soc., 133, 2350 (1986).
- [27] H. S. Kong, J. T. Glass, and R. F. Davis, U.S. Patent No. 5011549 (1991).
- [28] O. Kordina, C. Hallin, R. C. Glass, and E. Janzen, Inst. Phys. Conf. Ser. No. 137, 305 (1994).
- [29] R. Rupp, P. Lanig, J. Volkl, and D. Stephani, J. Cryst. Growth 146, 37 (1995).

- [30] S. Karmann, L. Di Cioccio, B. Blanchard, T. Ouisse, D. Muyard, and C. Jaussaud, *Mater. Sci. Eng. B* 29, 134 (1995).
- [31] D. J. Tritton, *Physical Fluid Dynamics*, second edition, Oxford Science Publications (1988).
- [32] P. Pirouz, in *Polycrystalline Semiconductors*, Eds. J. H. Werner, H. J. Moller, and H. P. Strunk (*Springer Proceedings in Physics*), Vol. 35, p. 200. (1989)
- [33] F. R. Chien, S. R. Nutt, and D. Cummings, *Philos. Mag. A* 68, 325 (1993).
- [34] J. D. Parsons, R. F. Bunshah, and O. M. Stafsuud, *Solid State Technol.* 11, 133 (1995).
- [35] H. S. Kong, B. L. Jiang, J. T. Glass, G. A. Rozgonyi, and K. L. More, *J. Appl. Phys.* 63, 2645, (1988).
- [36] J. A. Powell, D. J. Larkin, L. G. Matus, W. J. Choyke, J. L. Bradshaw, L. Henderson, M. Yoganathan, J. Yang, and P. Pirouz, *Appl. Phys. Lett.* 56, 1353 (1990).
- [37] K. Nishino, T. Kimoto, and H. Matsunami, *Kyoto ICSCRM*, p. 89 (1995).
- [38] R. W. Barlett, and R. A. Mueller, *Mat. Res. Bull.* 4, 341 (1969).
- [39] S. Yoshida, E. Sakuma, H. Okaumura, S. Misawaand, and K. Kondo, *J. Appl. Phys.* 62, 303 (1987).
- [40] K. Semmelroth, M. Krieger, G. Pensl, H. Nagasawa, R. Pusche, H. Hundhausen, L. Ley, M. Nerding, and P. Strunk, *Mat. Sci. Forum*, 457-460, 151 (2004).
- [41] W. K. Burton, N. Cabrera, and F. C. Frank, *Philos. Trans. R. Soc. London A* 243, 299 (1951).

- [42] R. L. Schwoebel, *J. Appl. Phys.* 37, 3682 (1966).
- [43] K. Voigtlaender, H. Risken, and E. Kasper, *Appl. Phys. A* 39, 31 (1986).
- [44] E. Kasper, *Appl. Phys. A* 28, 129 (1982).
- [45] T. Shitara and T. Nishinaga, *Jpn. J. Appl. Phys.* 28, 1212 (1989).
- [46] T. Kimoto, and H. Matsunami, *J. Appl. Phys.* 75, 850 (1994).
- [47] W. K. Burton, N. Cabrera, and F. C. Frank, *Philos. Trans. R. Soc. London A* 243, 299 (1951).
- [48] A. A. Burk Jr., L. B. Rowland, G. Augustine, H. M. Hobgood, and R. H. Hopkins, *Mat. Res. Soc. Symp. Proc.* 423, 275 (1996).
- [49] T. Kimoto, A. Itoh, and H. Matsunami, *Washington ICSCRM*, p. 95 (1993).
- [50] J. A. Powell, D. J. Larkin, and P. B. Abel, *J. Electron. Mater.* 24, 295 (1995).
- [51] J. A. Powell, D. J. Larkin, and P. B. Abel, *Kyoto ICSCRM*, p. 77 (1995).
- [52] J. A. Powell, D. J. Larkin, L. Zhou, and P. Pirouz, *Transactions of the Third Int. High Temperature Electronics Conference*, Albuquerque, NM, June 9-14, II-3 (1996).
- [53] R. Rupp, P. Lanig, R. Schorner, K. O. Dohnke, J. Volkl, and D. Stephani, *Kyoto ICSCRM*, p. 185 (1995).
- [54] R. Rupp, P. Lanig, J. Volkl, and D. Stephani, *J. Cryst. Growth* 146, 37 (1995).
- [55] J. A. Powell, P. Neudeck, *DARPA SiC High-Power Electronic Materials Program Review*, Arlington, VA, February 10, (1997).
- [56] H. S. Kong, J. T. Glass, R. F. Davis, *J. Appl. Phys.* 64, 2672 (1988).

- [57] J. C. Hallin, A. O. Konstantinov, O. Kordina, E. Janzen, Kyoto ICSCRM, p. 85 (1995)
- [58] W. Si, M. Dudley, H. Kong, J. Sumakeris, and C. Carter Jr., *J. Electron. Mater.* 26, 151 (1997).
- [59] O. Kordina, C. Hallin, R. C. Glass, A. Henry, and E. Jazen, Washington ICSCRM, p. 41 (1993).
- [60] S. Karmann, L. Di Cioccio, B. Blanchard, T. Ouisse, D. Muyard, and C. Jaussaud, *Mater Sci. Eng. B* 29, 134 (1995).
- [61] S. Nishino, and J. Saraie, *Springer Proc. in Physics*, vol. 34, Eds. G. L. Harris, and C. Y. Yang (Springer, Berlin) p. 45 (1989).
- [62] W. V. Muench and I. Pfaffeneder, *Thin Solid Films* 31, 39 (1976).
- [63] A. L. Steckl. C. Yuan, J. P. Li, and M. L. Loboda, *Appl. Phys. Lett.* 63, 3347 (1993).
- [64] K. Ikoma, M. Yamanaka, H. Yamaguchi, and Y. Shichi, *J. Electrochem. Soc.* 138, 3031 (1991).
- [65] W. Bahng and H. J. Kim, *Appl. Phys. Lett.* 69, 4053 (1996).
- [66] C. C. Chiu, S. B. Desu, and C. Y. Tsai, *J. Mater. Res.* 8, 2617 (1993).
- [67] N. Nordell, S. Nishino, JW. Yang, C. Jacob, and P. Pirouz, *J. Electrochem. Soc.* 142, 565 (1995).
- [68] K. Takahashi, S. Nishino, and J. Saraie, *J. Electrochem. Soc.* 139, 3565 (1992).
- [69] I. Golecki, F. Reidinger, and J. Marti, *Appl. Phys. Lett.* 60, 1703 (1992).
- [70] W. J. Choyke, R. P. Devaty, L. L. Clemen, M. Yoganathan, G. Pensl, and G. Hassler, *Appl. Phys. Lett.* 65, 1668 (1994).

- [71] D. J. Larkin, P. G. Neudeck, J. A. Powell, and L. G. Matus, *Appl. Phys. Lett.* 65, 1659, (1994).
- [72] S. Takagishi and H. Mori, *Jpn. J. Appl. Phys.* 22, L100 (1984).
- [73] N. Nordell, S. Schoner, and M. K. Linnarsson, *J. Electron. Mater.* 26, 187 (1997).
- [74] A. A. Burk, and L. B. Rowland, *Appl. Phys. Lett.* 68, 382 (1996).
- [75] E. N. Mokhov, Y. A. Vodakov, and G. A. Lomakina, in *Problems of Physics and Technology of Wide Band Gap Semiconductors (LIYaF, Leningrad)* p. 136 (1980)
- [76] A. S. Barash, Yu A. Vodakov, E. N. Kol'tsova, A. A. Mal'tsev, E. N. Mokhov, and A. D. Roenkov, *Sov. Phys. Techn. Lett.* 14, 2222 (1988).
- [77] R. B. Campbell, and H. S. Berman, *Mat. Res. Bull.* 4, S211 (1969).
- [78] P. M. Shenoy and B. J. Baliga, *Kyoto ICSCRM*, p.717 (1995).
- [79] V. M. Gusev, K. D. Demakov, and V. G. Stolyarova, *Radiation Effects* 69, 307 (1983).
- [80] D. B. Slater, L. A. Likpin, G. M. Johnson, A. V. Suvorov, and J. W. Palmour, *Kyoto ICSCRM*, p.805 (1995).
- [81] L. Spieb, O. Nennowitz, and J. Pezoldt, *Kyoto ICSCRM*, p.585 (1995).
- [82] D. Alok, and B. J. Baliga, *Kyoto ICSCRM*, p.749 (1995).
- [83] R. K. Nadella, M. A. Capono, *Appl. Phys. Lett.* 70, 886 (1997).
- [84] J. A. Gardner, M. V. Rao, Y. L. Tian, O. W. Holland, E. G. Roth, P. H. Chi, and I. Ahmad, *J. Electron. Mater.* 26, 144 (1997).
- [85] S. Ahmed, C. J. Barbero, and T. W. Sigmon, *Appl. Phys. Lett.* 66, 712 (1995).

- [86] S. Ahmed, C. J. Barbero, T. W. Sigmon, and J. W. Ericson, *J. Appl. Phys.* 77, 6194 (1995).
- [87] C. D. Brandt, A. K. Agarwal, G. Augustine, R. R. Barron, A. A. Burk, R. C. Clarke, R. C. Glass, H. M. Hobgood, A. W. Morse, L. B. Rowland, S. Seshadri, R. R. Siergiej, T. J. Smith, S. Sriram, M. C. Driver, and R. H. Hopkins, *Kyoto ICSCRM*, p.659 (1995).
- [88] T. Kimoto, A. Itoh, H. Matsunami, T. Nakata, and M. Watanabe, *J. Electron. Mater.* 25, 879 (1996).
- [89] D. Kawase, T. Ohno, T. Iwasaki, and T. Yatsuo, *Kyoto ICSCRM*, p.177 (1995).
- [90] M. V. Rao, J. Gardner, O. W. Holland, G. Kelner, M. Ghezzi, D. S. Simons, and P. H. Chi, *Kyoto ICSCRM*, p.521 (1995).
- [91] M. V. Rao, P. Griffiths, O. W. Holland, G. Kelner, J. A. Freitas, D. S. Simons, P. H. Chi, M. V. Rao, J. Gardner, O. W. Holland, G. Kelner, D. S. Simons, and P. H. Chi, and M. Ghezzi, *J. Appl. Phys.* 77, 2479 (1995).
- [92] Ki-Ha Hong, Ph. D. Thesis, p. 57-62, Seoul National University (2004).
- [93] A. Pimpinelli, *Physics of Crystal Growth*, Cambridge University Press (1998).
- [94] J. Tersoff, Y.H. Phang, Z. Zhang, and M.G. Lagally, *Phys. Rev. Lett.* 75, 2730 (1995).
- [95] O.L. Alerhand, D. Vanderbilt, R.D. Meade, and J.D. Joannopoulos, *Phys.Rev. Lett.* 61, 1973 (1998).
- [96] Yole development, *SiC devices in power electronics* (2010).
- [97] Mitsubishi electric corporation, *Mitsubishi product report* (2011).

[98] H. Kimimori, Mater. Sci. Forum 600-603, 889 (2008).

[99] J. K. Jeong, Ph. D. Dissertation, Department of Material Science and Engineering, Seoul National University, Seoul, Korea (2002).

## **3. EXPERIMENTAL PROCEDURE**

### **3.1. CVD System**

The CVD system consist of (1) the reaction chamber made in quartz, (2) the vacuum system which includes two mechanical pump and one turbo molecular pump, (3) the gas inlet and exhaust lines, and (4) the control panel including the pressure control system. Fig. 3.1 shows the schematic diagram of cold-wall, horizontal-type CVD system. Fig. 3.2 shows the schematic diagram of the SiC-coated graphite susceptor and quartz boat. This system is almost the same as that described in detail by W. Bhang [1].

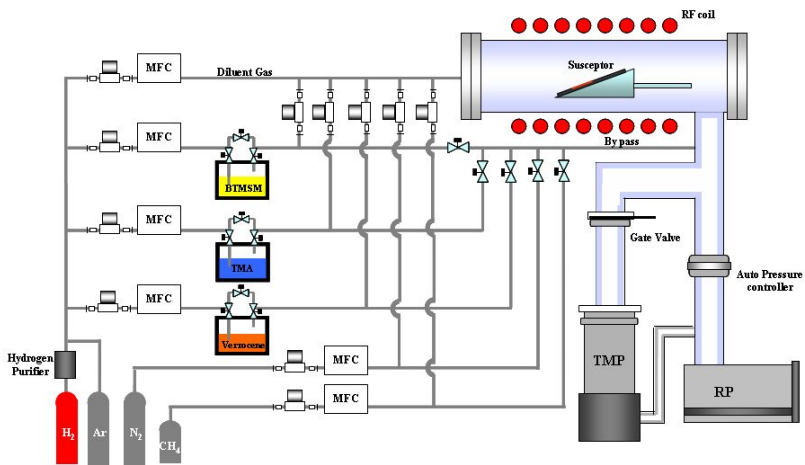


Fig. 3.1 Schematic diagram of MOCVD system

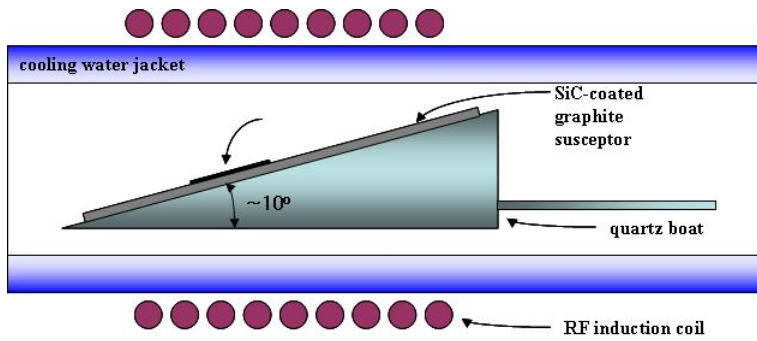


Fig. 3.2. The schematic diagram of the reactor chamber of CVD system.

### 3.2. Procedure for the Growth of 4H-SiC Epitaxial Layer

The 4H-SiC epitaxial films were deposited on the n-type 4° off-axis 4H-SiC Si-face, C-face, and on-axis substrates by low-pressure chemical vapor deposition (CVD). A horizontal cold wall system with a SiC coated graphite susceptor was used, which was inductively heated by an RF generator. The substrates were double-side polished n-type 4H-SiC Si-face and C-face wafers with 4° off-orientation toward the  $[11\bar{2}0]$  direction. The substrate temperature was measured using an optical pyrometer which was calibrated with the melting temperature of Si (1418 °C). Prior to the growth, the substrates were sequentially cleaned with acetone, methanol,  $\text{H}_2\text{SO}_4/\text{H}_2\text{O}_2 = 4:1$  at 130 °C, and diluted HF, and then rinsed with deionized water in order to remove the surface contamination and native oxide layer. Before the epitaxial growth, *in situ*  $\text{H}_2$  pre-etching was done for 10 min to remove the damaged scratches and substrate imperfections such as voids and dislocations. The  $\text{H}_2$  pre-etching temperature and pressure were 1450–1500 °C and 180 Torr, respectively. The growth temperature and the bubbling gas flow rate of BTMSM source ranged between 1240 °C and 1550 °C and 5 sccm to 20 sccm, respectively. The BTMSM canister was immersed into a water bath and maintained at 24 °C, which was controlled by a thermostat device with a circulation pump (LAUDA E100, temperature control  $\pm 0.02$  °C). The vapor

pressure of BTMSM source at 24 °C was roughly estimated to be 13.55 torr by using Clausius-Clapeyron equation. The actual flow rates of BTMSM with H<sub>2</sub> bubbling gas flow rate of 5–20 sccm were also calculated to be 0.41–1.63 sccm, respectively. The input flow rate of the diluent gas, H<sub>2</sub>, was maintained at 3000 sccm and the pressure in the growth chamber was fixed at 180 Torr. The epitaxial growth was performed for 1-2 hr.

### **3.3. Characterization Method**

#### **3.3.1 Thickness Evaluation**

The thickness of SiC epilayer is very important parameter because it is essential parameter in various SiC based devices. For confirmation of the exact thickness, testing epilayers were grown on the porous substrate due to its clear visibility of interface between the epilayer and substrate. The thickness of epilayers was observed by the scanning electron microscopy.

#### **3.3.2. Surface Morphology**

The surface morphology of *in situ* H<sub>2</sub>-etched substrates and epitaxial films was observed using a Nomarski microscope (NMS; Nikon, Eclipse LV100D), atomic force microscopy (AFM; JEOL, JSPM-5200), and scanning electron microscopy (SEM; Hitachi, S-48000).

### 3.3.3. Structure and Defect Analysis

X-ray diffraction (XRD) analysis was conducted by a PANalytical high resolution X-ray diffractometer with a 2 kW Cu radiation source. Double-axis crystal XRD was used to evaluate the crystallinity. The chemical structure of the hydrogen etched SiC layers was evaluated by X-ray photoelectron spectroscopy (XPS; Sigma Probe, ThermoVG, U.K.). Micro-Raman spectroscopy was performed to determine the existence of polytype conversion using a Horiba Jobin-Yvon LabRam HR spectrometer and detected with a liquid-nitrogen-cooled CCD detector. The 514.5-nm line of an Ar-ion laser was used as an excitation source, and the laser power on the sample was maintained at around 100  $\mu$ W to avoid heating of the sample by the measuring laser beam. The laser spot diameter was about 1  $\mu$ m. The Raman signal was collected in a backscattering geometry using a  $\times$ 100 microscope objective lens. The film uniformity were examined by electron back scattering diffraction pattern (EBSP, Oxford instruments Ltd.), which is a map of the angular variations (Kikuchi lines) in intensity of electrons back-scattered from a crystalline specimen after incident electron beam has been diffracted. The crystallographic relationships between domains were also examined by EBSD. Because EBSD is an add-on package to SEM, it has the capability of diffraction and imaging in real time with a spatial resolution of 0.5 $\mu$ m. Because the escape depth of the electron beam is approximately 10 nm, it was used to determine whether the very thin layer is amorphous or crystalline.

### 3.3.4. Electrical Properties

Capacitance-voltage (C-V), current-voltage (I-V), and Hall effect measurements were employed to measure the electrical properties of the 4H-SiC films. Although four-point probe is a convenient tool for the measuring sheet resistivities of thin films, it is difficult to measure the sheet resistivity for low-doped epilayer due to high contact resistance and resistivity. Capacitance-Voltage measurement, which uses the voltage dependence of the depletion layer capacitance of Schottky contacts, is a method for reliable characterization of the epilayer in terms of carrier concentration as a function of epitaxial layer thickness. The carrier concentration can be written:

$$N_D(x_d) = \frac{-2}{qK_S\epsilon_0[d(1/C^2) / dV_A] x_d A^2} \quad (3.1)$$

Where,  $q = 1.6 \times 10^{-19} \text{C}$ ,  $K_S = 10.03(4\text{H} - \text{SiC})$ ,  $\epsilon_0 = 8.85 \times 10^{-12} (\text{F}/\text{m})$  and A: area of Schottky contact. In case of n-type 4H-SiC, the ohmic contacts are prepared by e-beam evaporation of Ni (500 Å) with subsequent Rapid Thermal Processing (RTP) annealing at 1000 °C for 2 min and the Schottky contacts (diameter: 300 µm) formed by the evaporation of Ni (1000 Å). In case of p-type 4H-SiC, the ohmic contacts are prepared by e-beam evaporation of Al (1000 Å) with subsequent RTP annealing at 1000 °C for 3 min and the Schottky contacts (diameter: 300 µm) formed by the evaporation of Al (1000 Å). Hall effect measurement gives the accurate carrier concentration, doping type (p or n), and the Hall mobility of the epilayers. For Hall effect measurements, square sample of  $8 \times 8 \text{ mm}^2$  size was used. Ohmic

contacts in the corner of each sample (van der Pauw arrangement) are prepared by e-beam evaporation of Ni or Al followed by RTP annealing. The carrier concentration and Hall mobilities of the 4H-SiC epilayers were measured using a Bio-Rad HL5500 system (temperature range from 77 to 300 K).

### **3.4. Precursor for Homoepitaxial Growth of 4H-SiC**

The precursor for homoepitaxial growth of SiC is bis-trimethylsilylmethane [ $((\text{CH}_3)_3\text{Si})_2\text{CH}_2$ , BTMSM], which is purchased from United Chemical Inc. The boiling temperature and freezing temperature of BTMSM were 137 °C (410 K) and -71 °C (202 K), respectively. Therefore, the BTMSM is liquid phase at room temperature. The source material is feed into the reaction chamber by the carrier gas,  $\text{H}_2$ , which flows through liquid BTMSM source in the bubbler. The BTMSM source bubbler was immersed into water bath. The bubbler bath maintained a constant temperature of 24 °C by thermostat device with circulation pump. This material has the advantage of non-toxic and non-flammable source, compared to  $\text{SiH}_4$ , which is conventional gas for Si supply.

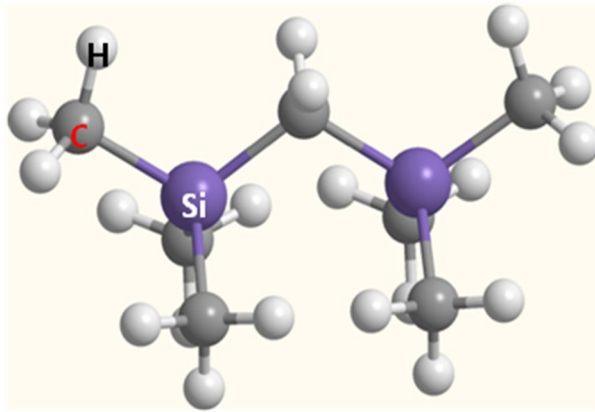


Fig. 3.3. The structure of bis-trimethylsilylmethane. Silicon atoms bonded tetrahedrally with carbon atoms, which is the same structure of SiC crystal.

### 3.4.1 Estimation of BTMSM vapor pressure and actual flow rate

[2]

Because BTMSM source material is in its liquid phase, source material was fed into the reactor by the carrier gas  $H_2$ , which flows through liquid source in the bubbler. A plot of  $\Delta H_v$  (the molar heat of evaporation at the boiling temperature,  $T_b$ ) versus  $T_b$  indicates that  $\Delta H_v/T_b$  lies in the vicinity of  $88J/^\circ C$ , which is known as Trouton's rule. That is,

$$\frac{\Delta H_v}{T_b} = \Delta S_b = 88J/^\circ C \quad (3.2)$$

Trouton's rule can be used to estimated the value of  $\Delta H_v$  for a substance based on the boiling temperature of the liquid.

Let's consider the following chemical reaction:



Since  $\Delta V = V_{\text{vap}} - V_{\text{liq}} \doteq V_{\text{vap}}$ , Clapeyron equation can be written:

$$\left(\frac{dP}{dT}\right)_{\text{eq}} = \frac{\Delta H_v}{T\Delta V} = \frac{\Delta H_v}{T V_{(v)}} \quad (3.4)$$

If it is further assumed that the vapor in equilibrium with the condensed phase behaves ideally, that is,  $PV=RT$ , then

$$\left(\frac{dP}{dT}\right)_{\text{eq}} = \frac{P\Delta H_v}{R T^2} \quad (3.5)$$

rearrangement of which gives:

$$d \ln P = \frac{\Delta H_v}{R T^2} dT \quad (3.6)$$

Above Equation is known as Clausius-Clapeyron equation. If  $\Delta H$  is independent of temperature, that is, if  $c_p(\text{vapor}) = c_p(\text{liq})$ , then integration of Eq. yields the vapor pressure as a function of temperature.

$$\ln P = \frac{\Delta H_v}{R} \left( -\frac{1}{T_b} - \frac{1}{T} \right) = \frac{88(\text{J/K}) \times 410(\text{K})}{8.3144} \left( -\frac{1}{410} - \frac{1}{T} \right) \quad (3.7)$$

If the bubbler temperature of source material is kept at 24 °C, vapor pressure of BTMSM is approximately 0.017829 atm (13.55 Torr). Therefore, the actual flow rate of BTMSM source material can be calculated:

$$\text{Flow rate of BTMSM} = \text{Flow rate of } H_2 \times \frac{P_v}{P_{\text{chamber}} - P_v} \quad (3.8)$$

In the case of 10 sccm of  $H_2$  carrier gas and chamber pressure of 180 torr, which is typical deposition condition, the actual flow rate of BTMSM is approximately 0.81 sccm.

## **Bibliography**

- [1] W. Bhang, Ph. D. dissertation, Seoul National University (1997)
- [2] J. K. Jeong, Ph. D. Dissertation, Department of Material Science and Engineering, Seoul National University, Seoul, Korea (2002).

## **4. Results and Discussions**

### **4.1. Comparative Study of 4H-SiC Epitaxial Layers Grown on 4° off-axis Si- and C-face Substrates using BTMSM**

#### **4.1.1. Introduction**

Silicon carbide (SiC) has been considered as a promising wide bandgap material for high power, high frequency, and high temperature devices owing to its high breakdown field ( $\sim 3 \times 10^6$  V/cm), high thermal conductivity, high saturated electron drift velocity ( $\sim 2 \times 10^7$  cm/s), and chemical stability. [1,2] Due to the commercialization of its large single-crystal wafer up to size of 6 inch and excellent epitaxial growth technique, SiC become a better candidate for application in high-power and high-frequency electronic devices compared to the other wide-bandgap materials such as GaN, ZnO, and diamond. Among the many SiC polytypes, most of the recent work has focused on 4H-SiC owing to its high saturated electron drift velocity [3] and commercial availability.

Recently, the off-angle reduction from 8° to on-axis substrate has attracted much attention, [4,5] because of two main advantages. First, it can reduce basal plane dislocations (BPDs), which are known as killer defects for power

device applications. Second, it can diminish crystal waste in slicing ingots for producing wafers. However, the epitaxial growth on low off-angle 4H-SiC substrates exhibits a difficulty in controlling the morphology of epitaxial film, especially macro step-bunching. The step-bunching behavior of 4H-SiC is one of the major problems that should be eliminated, and there has been a lot of research in this area. Step-bunching with large surface roughness induces a high leakage current as well as a low breakdown voltage of Schottky barrier diodes. [6,7] From this point of view, a major advantage of C-face SiC films over Si-face SiC films is that a smoother surface morphology can be achieved after epitaxial growth and post-implant annealing. [8,9] Fukuda et al. proposed the C-face SiC as a promising candidate instead of the Si-face for fabricating high-performance power MOSFETs with markedly enhanced channel mobility. [10] Furthermore, additional advantages of the C-face epitaxial films compared to the Si-face films have been reported: a micropipe dissociation with a wider range of C/Si ratios, [11] a higher conversion efficiency of BPDs into threading edge dislocations, [12] and a 10-times higher thermal oxidation rate. [13] In addition, the C-face seed crystal does not produce 6H polytype inclusions in the bulk growth of 4H-SiC, as opposed to the Si-face seed crystal [14] indicating that the C-face has a better polytype stability during the crystal growth of 4H-SiC compared to the Si-face. Therefore, it is essential to determine the dependence of the quality of epitaxial layers on substrate polarity. Although many researchers using organosilicon source material precursors have reported the epitaxy of SiC, [15-19] there has been no systematic report for the 4H-SiC substrates having

two different polar properties.

In this chapter, we investigate the homoepitaxial growth of 4H-SiC on the 4° off-axis Si-face and C-face substrates using an organosilicon source material, bistrimethylsilylmethane (BTMSM;  $C_7H_{20}Si_2$ ). BTMSM, containing both C and Si components, is nontoxic and nonflammable. It also makes lower temperature growth possible compared to a silane ( $SiH_4$ ) source. [15] Our research group previously performed SiC epitaxial growth using BTMSM as a precursor, but most efforts have been focused on Si-face substrates. [15-17] The effects of the growth conditions, such as growth temperature and source flow rate on the surface morphology, crystallinity, polytype conversion, defect generation, and structural imperfection of the epilayers on different polar surfaces, were investigated. This study has successfully identified the optimized experimental conditions for *in situ* surface preparation and epitaxial growth on C-face as well as Si-face substrates using the BTMSM.

#### **4.1.2. *In situ* Surface Preparation of 4° off-axis Si-face and C-face SiC Substrates using Hydrogen**

H<sub>2</sub> etching of substrates, prior to the epitaxial growth, is a prerequisite process to gain the optimal surface; the process removes the damaged layer, surface native scratches, and incomplete nucleation generation site. [20,21] The experiment was conducted for 10 min, while the etching temperatures were 1450 °C and 1500 °C to reveal the different characteristics between each face of the substrates. Figure 4.1 presents AFM images of 4° off-axis Si-face and C-face 4H-SiC wafers and hydrogen etched wafers obtained at 1450 °C and 1500 °C. Figure 4.1 (a) and (b) present the bare substrates of the Si-face and C-face, showing native scratches. Root-mean-square (RMS) roughnesses of the substrates were 0.94 nm and 0.67 nm, respectively. Figure 4.1 (c) shows irregular macro step-bunching morphology and an RMS roughness of 5.32 nm when the surface of the Si-face was etched at 1500 °C, whereas a smooth surface without scratch or step-bunching and having an RMS roughness of 0.4 nm could be obtained at 1450 °C (Fig. 4.1 (e)). There was no step-bunching on C-face SiC at 1500 °C (Fig. 4.1 (d)) with an RMS roughness of 1.84 nm, but some clusters, which cause several defects in epitaxial growth, were found. Nevertheless, with a hydrogen etching temperature of 1450 °C, no step-bunching nor clusters were observed with an RMS roughness of 0.45nm (Fig. 4.1 (f)). As shown in the Figure 4.1, macro step-bunching only occurred on

the Si-face SiC when the etching temperature was 1500 °C. It is believed that step bunching occurs as a result of enhanced surface etching under high temperatures in a hydrogen atmosphere. Since the Si-face possesses high surface-free energy, surface expands in order to reduce the energy during the etching process, resulting in the formation of step-bunching. Because the C-face is more chemically active than the Si-face, [9] the high temperature of 1500 °C in the hydrogen etching process may generate more clusters on C-face than on the Si-face. Such clusters should be removed, since such clusters are the origin of crystallographic defects during epitaxial growth.

Therefore, in order to acquire smooth layers on the two different faces, we conducted the surface preparation at a temperature of 1450 °C in a hydrogen environment for 10 min prior to the epitaxial growth.

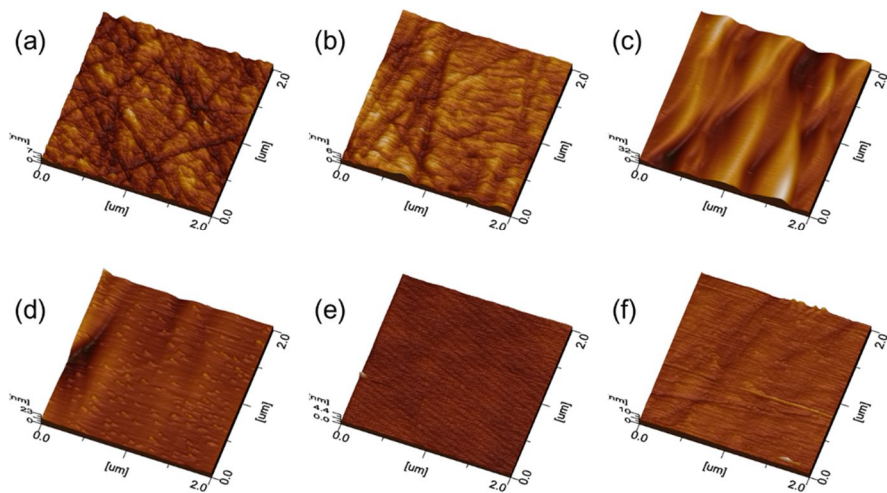


Fig. 4.1. AFM images of (a) Si-face (b) C-face bare substrate, (c) Si-face (d) C-face substrate after  $H_2$  etching at 1500 °C, and (e) Si-face (f) C-face substrate after  $H_2$  etching at 1450 °C.

### 4.1.3. 4H-SiC Epitaxial Layers Grown on 4° off-axis Si-face Substrates using BTMSM

Figure 4.2 shows the Nomarski micrograph and AFM image of the 4H-SiC epitaxial layer grown on a Si-face substrate at 1400 °C. The BTMSM carrier gas flow rate was 10 sccm. By using BTMSM source, which operates at a temperature 200–300 °C lower than the usual SiC epitaxial growth temperature of 1600 °C using a gas source including SiH<sub>4</sub> and C<sub>3</sub>H<sub>8</sub>, a good surface morphology without defects or step-bunching and having a low RMS roughness of 0.2–0.8 nm could be obtained over a broad temperature range of 1320 to 1440 °C. Unlike the report on the increasing density of defects with a lower growth temperature, [22] the epitaxial layer grown in this experiment showed no defects on the surface. It is believed that the smooth surface is obtained owing to the bonding characteristics of the BTMSM source, which has an alternate and tetrahedral Si–C bonding structure like the crystal phase of SiC. [15]

Figure 4.3 presents the AFM step profiling of SiC epilayers grown at 1280, 1360, and 1440 °C. The step morphology at the growth temperature of 1280 °C illustrates high RMS roughness of 20–30 nm owing to 3D nucleation and growth. Layer-by-layer growth or step-flow growth occurred with the growth temperature of 1360 °C, resulting an RMS roughness of 0.7–0.8 nm; and growth temperature of 1440 °C, resulting an RMS roughness of 0.2–0.3 nm, respectively.

Figure 4.4 shows the RMS roughness determined from the AFM image of

the 4H-SiC epitaxial layer, which was grown at various growth temperatures and flow rate of BTMSM carrier gas. We evaluated the RMS roughnesses five times for each sample in order to ensure reliability. As the growth temperature decreases or the carrier source flow rate increases above 15 sccm, the RMS roughness of the epitaxial layers increases by 10–100 times, rendering a non-specular and rough surface. It is assumed that there was insufficient step flow growth, and some parts of the terrace were affected by 3D nucleation and growth.

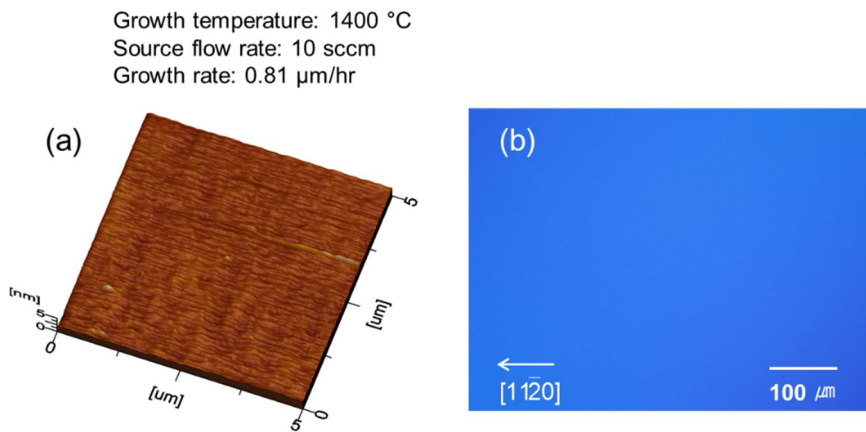


Fig. 4.2. (a) AFM image and (b) Nomarski micrograph of 4H-SiC epitaxial layer grown at 1400 °C on 4° off-axis Si-face substrates. (BTMSM Source flow rate: 10 sccm)

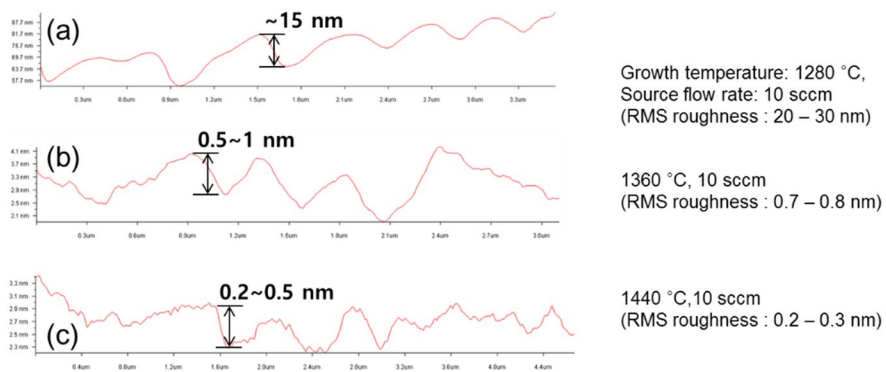


Fig. 4.3. Peak to valley of height profile data of AFM images of 4H-SiC epilayers grown on 4° off-axis Si-face substrates at various conditions.

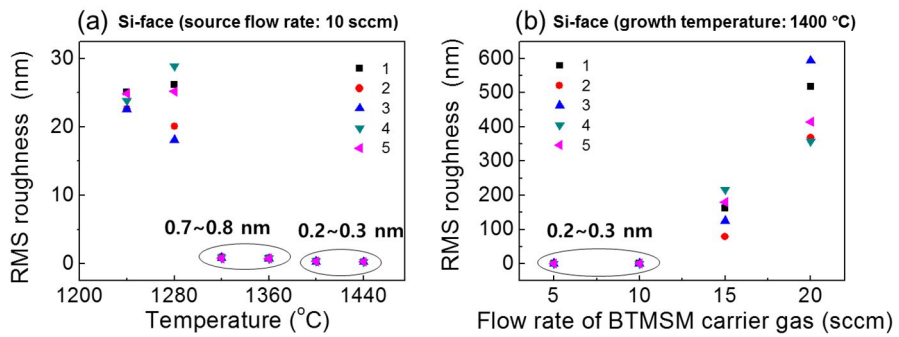


Fig. 4.4. RMS roughness of AFM image in 4H-SiC epitaxial layer, which was grown at various growth temperatures and flow rates of BTMSM carrier gas.

Micro-Raman spectroscopy was conducted to verify the formation of the single polytype. As a result, we could observe that the 4H-SiC polytype was fairly well grown at a growth temperature of 1320–1440 °C, as seen in Figure 4.5. However, macro step-bunching, which have a step height of 5–7 nm, occurred with a growth temperature of 1500 °C, as shown in Fig. 4.6. The main reasons for the step-bunching are minimization of the surface energy, impurity effect, and step kinetics. [23] It is therefore assumed that the higher surface free energy of the Si-face generated step-bunching. In addition, step-kinetics explain the phenomenon in terms of our epitaxial growth, that is, the Schwoebel effect. [24] The atoms during the growth and etching processes are usually influenced by the Ehrlich–Schwoebel (ES) barriers of materials. [24,25] Since SiC is a material with a normal ES barrier, adatoms naturally move into the internal site of the step, which is called a kink site. Therefore, more atoms would flow into the larger terraces during the growth process to reduce the step-bunching, while increasing etching atoms during the etching process would induce step-bunching. In summary, materials with the normal ES barrier generate more step-bunching during etching, rather than the growth process. In our experiment, epitaxial growth was carried out under 1500 °C as sources were sufficiently supplied, but hydrogen etching was excessively performed to generate step-bunching. Additionally, macro step-bunching on the Si-face, during the hydrogen etching process at 1500 °C, is observed before epitaxial growth. Thus, if the growth process is conducted under 1500 °C, there would be no step-bunching generated by excessive hydrogen etching.

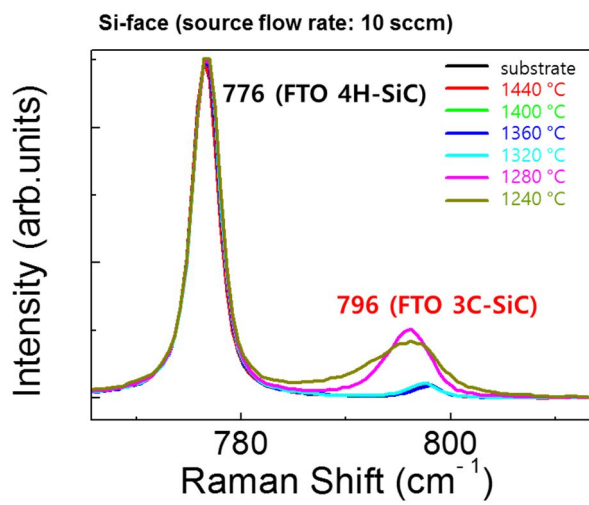


Fig. 4.5. Micro-Raman spectra (FTO phonon mode) of various growth temperatures for epilayers on Si-face substrates.

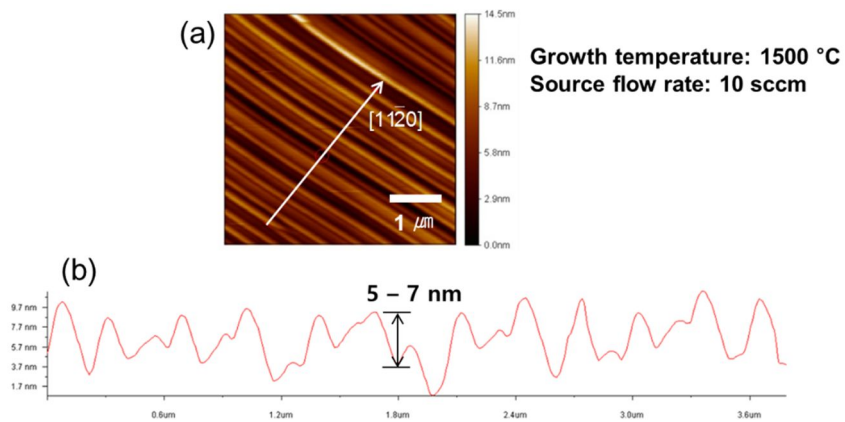


Fig. 4.6. (a) AFM image of 4H-SiC epitaxial layer grown at 1500 °C on 4° off-axis Si-face substrates, and (b) its peak to valley of the height profile data. (BTMSM source flow rate: 10 sccm)

#### **4.1.4. 4H-SiC Epitaxial Layers Grown on 4° off-axis C-face Substrates using BTMSM**

Figure 4.7(a) shows Nomarski micrographs of 4H-SiC epitaxial layers grown at various growth conditions on 4° off-axis C-face substrates. The epilayers show a non-specular surface until the growth temperature increases to 1450 °C, indicating epitaxial growth did not occur. Eventually, the grown layer on the C-face generates epitaxial growth at 1500 °C, which is 100 °C higher than that on the Si-face SiC substrates. Epitaxial growth is influenced by critical supersaturation ratio and surface diffusion length of the adatom on the surface. [8] Critical supersaturation ratio of the C-face SiC shows a markedly lower value than that of the Si-face, irrespective of temperature. This indicates that adatoms generate nucleation easier and more frequently on the C-face substrates. Therefore, it requires atoms to diffuse into the kink site more rapidly to gain step flow growth before 3D growth occurs. Therefore, a higher growth temperature would be necessary to acquire more energy. It is known that the longer length of surface diffusion on the C-face substrate suppresses rapid nucleation and 3D growth. However, considering a higher value of the C/Si ratio decreases the surface diffusion length, [26] and the value of the BTMSM source used in this study has a fairly high value of 3.5, the value of the critical supersaturation ratio rather than the surface diffusion length would play the dominant factor. Thus, the C-face will require a higher growth temperature of 1500 °C compared to the Si-face of 1400 °C.

As shown in Fig. 4.7(a), two types of defects, complex triangular (TD)

defects and inverted pyramid (IP) defects, were observed; TD are planar defects, and IP defects are concave contour-shaped defects with 0.15  $\mu\text{m}$  depth, as shown in the AFM image provided in Fig. 4.7(b). Previous studies reported that C atoms generate more C-C bonding under a C-rich growth environment, resulting in defects. [9] This corresponds with the results of our experiments where BTMSM is a C-rich source with a C/Si value of 3.5. As discussed earlier, clusters were increasingly formed at 1500  $^{\circ}\text{C}$  during the hydrogen etching process. Although the temperature of the hydrogen etching process was conducted at 1450  $^{\circ}\text{C}$ , defects were observed when the growth temperature was 1500  $^{\circ}\text{C}$ . When the growth temperature was further increased to 1550  $^{\circ}\text{C}$ , the density of defects decreased while the sizes became larger. The observed triangular-shaped defects are generally formed owing to interrupted step-flow growth, thus it is assumed that the mobility of the adatoms on the surface increased with higher growth temperature, to make adatoms resistant to interrupted step flow growth. In addition, the reason for bigger defects is that clusters became more influenced during the hydrogen etching process as the growth temperature was 1550  $^{\circ}\text{C}$ . It was possible to decrease the number of these defects by reducing the flow rate of BTMSM carrier gas from 10 sccm to 5 sccm, which resulted in a decrease of C-C bonding. This occurs because the amount of source from the CVD process has decreased while the C/Si ratio remains the same, and the amount of source was low enough to reduce the growth rate and enable stable growth.

Figure 4.8 shows the AFM and the peak to valley of the height profile of the AFM image of 4H-SiC epitaxial layer grown at 1500  $^{\circ}\text{C}$  with a source

flow rate of 10 sccm on 4° off-axis C-face substrates. The peak to valley of the height profile data of the AFM image in Fig. 4.8(b) shows that the grown epitaxial layers have an RMS roughness of 0.501 nm.

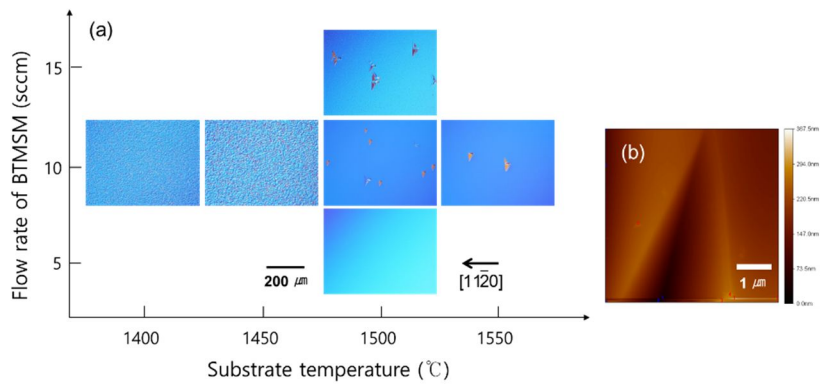


Fig. 4.7. (a) Nomarski micrographs of 4H-SiC epitaxial layers grown at various growth conditions on  $4^\circ$  off-axis C-face substrates. (b) AFM image of the inverted pyramid defect.

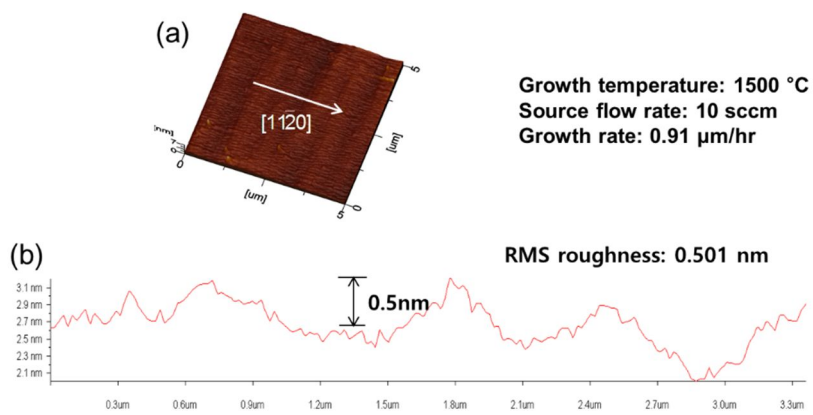


Fig. 4.8. (a) AFM image, and (b) the peak to valley of the height profile of the AFM image of 4H-SiC epitaxial layer grown at 1500 °C on 4° off-axis C-face substrates. (BTMSM source flow rate: 10 sccm)

Figure 4.9 shows the 4H-SiC (0004) full width at half maximum (FWHM) of the rocking curve depending on (a) the growth temperature and (b) the BTMSM source flow rate. For comparison, the rocking curves were taken before and after the epitaxial growth. FWHM of all the substrates lay in the range of 16 to 25 arcsec. The substrates having the strong mosaicity or FWHM more than 25 arcsec were not used for the growth. The FWHM of the rocking curve for the epilayers monotonously decreases with increasing growth temperature from 1350 °C to 1550 °C, indicating better crystallinity at higher temperature (Fig. 4.9(a)). Here, the BTMSM flow rate was fixed at 10 sccm. Moreover, the FWHM of the epilayers grown above 1450 °C are lower than those of the substrates. At 1500 °C, the FWHM of 16.56 arcsec was much lower than that of the substrate, 20.88 arcsec. However, the FWHM of the epilayers grown at a BTMSM flow rate of 15 sccm is slightly higher (22.68 arcsec) than that of the substrates (18 arcsec) (Fig. 4.9(b)). The step-flow growth mode is enhanced with high temperature and low supersaturation, so crystallinity degradation can be prevented by high growth temperature and low supersaturation.

Figure 4.10 shows the Raman spectra of the epilayers grown on C-face substrates at various growth temperatures (BTMSM flow rate of 10 sccm). At a growth temperature of 1300 °C, peaks at 796  $\text{cm}^{-1}$  and 971  $\text{cm}^{-1}$  were observed, indicating the formation of 3C-SiC structures. A single polytype with a non-specular surface was observed at 1400 °C, and sharper FLO peaks, indicating better crystallinity of the grown layers, were observed at 1500 °C.

Figure 4.11 shows that a complex triangular defect was observed at a

BTMSM flow rate of 15 sccm on the C-face grown at 1500 °C. As the source flow rate increased to 15 sccm, a good quality surface was not achieved, as the appearance of black spots generated defects of complex shape. The surface became rougher and the number of defects increased. This is observed as the number of adatoms in terraces reaches a certain level that disturbs the step flow growth. This defect has an overall triangular shape, but left and right-side wings were composed of inverted pyramid defects. In Fig. 4.11(a), the starting point of the complex triangular defects, that is the black spots, reveals peaks related to the 3C-SiC structure. Investigating the FTO peak, the ratio of two peaks was different from that of a surface without defects, indicating the amount of 3C inclusion is much higher (Fig. 4.11(b)). Figure 4.11(c) shows the Raman intensity ratio map of the peak at  $796\text{ cm}^{-1}$  (3C-TO phonon mode) to the peak at  $776\text{ cm}^{-1}$  (4H-TO phonon mode) for the defect. Most of the 3C-SiC structure is possessed in black spots and the central part of the triangular defect exhibits less inclusion but still shows a 3C-SiC structure. The IP defects on both sides of the wings show 4H structures, but a 3C structure could be observed at their edge. In the initial growth process, the step flow growth occurs with an abundant amount of source flow to start nucleation and growth in the middle of the terrace and incur defective regions.

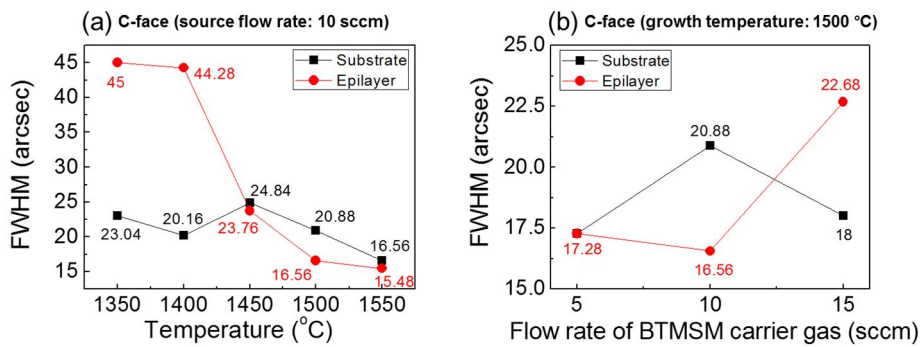


Fig. 4.9. FWHM difference of 4H-SiC (0004) rocking curves before and after the epitaxial grown on the C-face substrates as a function of (a) growth temperature and (b) BTMSM source flow rate.

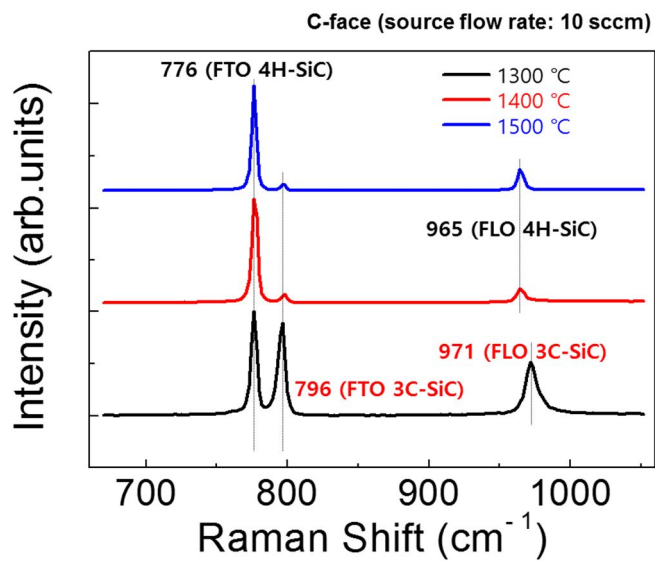


Fig. 4.10. Micro-Raman spectra of various growth temperatures for epilayers on C-face substrates.

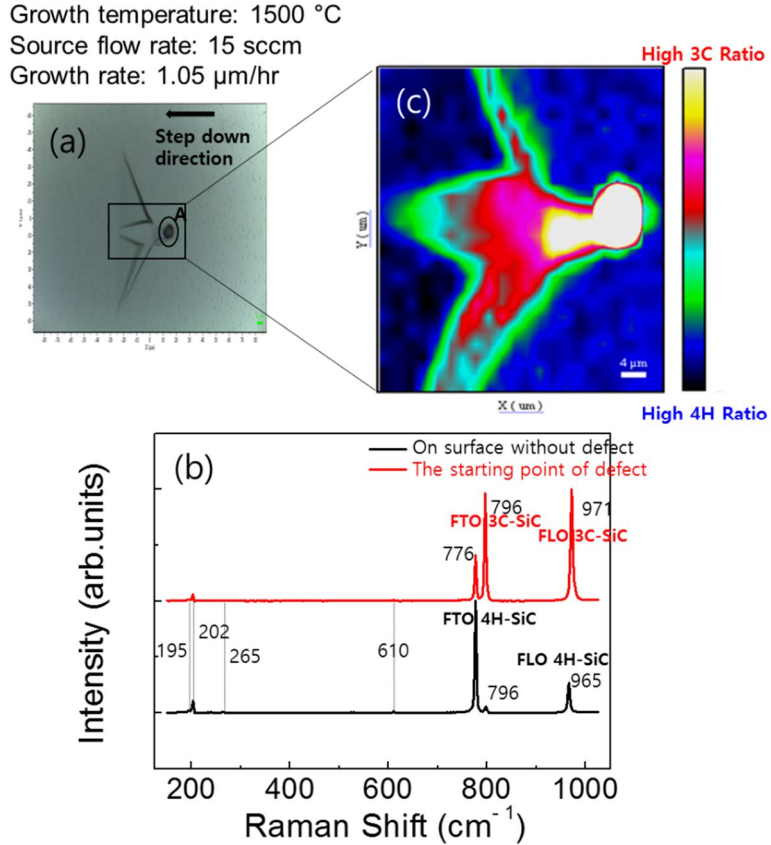


Fig. 4.11. Complex triangular defect occurring with higher BTMSM flow rate of 15 sccm on the C-face. (a) The optical image, (b) Micro-Raman spectra of the point “A” shown in (a), (c) Raman intensity ratio map of the peak at  $796\text{ cm}^{-1}$  (3C-TO phonon mode) to the peak at  $776\text{ cm}^{-1}$  (4H-TO phonon mode) for the defect shown in (a).

The size of the defective region was about 32  $\mu\text{m}$ , as shown in Fig. 4.12(a). Since this study employed  $4^\circ$  off-angle substrates, the thickness of such a defective region can be calculated to be  $\sim 2.2 \mu\text{m}$ . The actual thickness of the epilayer itself was 2.1  $\mu\text{m}$  when observed by SEM. Therefore, it is inferred that such a defect was initiated from the interface between the substrate and epilayer.

The inverted pyramid defect in Fig. 4.13 is called an isolated inverted pyramid, since it was independently generated compared to the complex shaped defects illustrated in Fig. 4.11, when the flow rate of BTMSM carrier gas was 10 sccm. The ratio of the FTO peak was analyzed through micro-Raman spectroscopy to compare defect-free and defective regions. The results revealed the defective region possesses more 3C-SiC structures than the defect-free region, which is contrary to previous reports. Some research groups insisted that defects are composed of 4H, while other research groups insisted that it is composed of 3C. [9,27] This study revealed that the dents in the central area of IP defects, shown in Fig. 4.11(c), were composed of 4H-SiC structures, whereas the edge parts were composed of 3C-SiC structures.

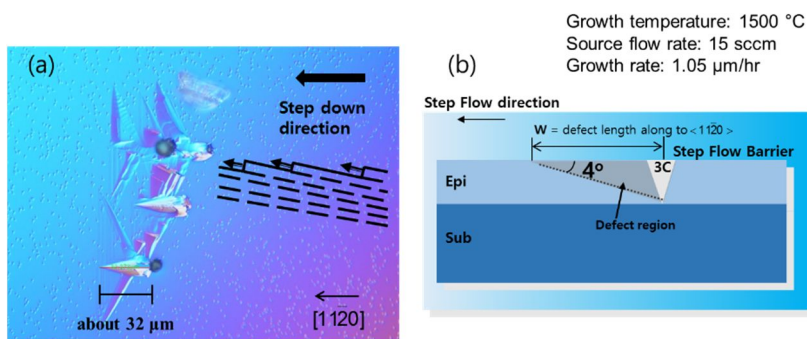


Fig. 4.12. (a) Nomarski micrographs of the defective region of 4H-SiC epitaxial layers grown at temperature of 1500 °C and source flow rate of 15 sccm on 4° off-axis C-face substrates. (b) The schematic diagram of the defective region in (a).

Growth temperature: 1500 °C  
Source flow rate: 10 sccm  
Growth rate: 0.91  $\mu\text{m/hr}$

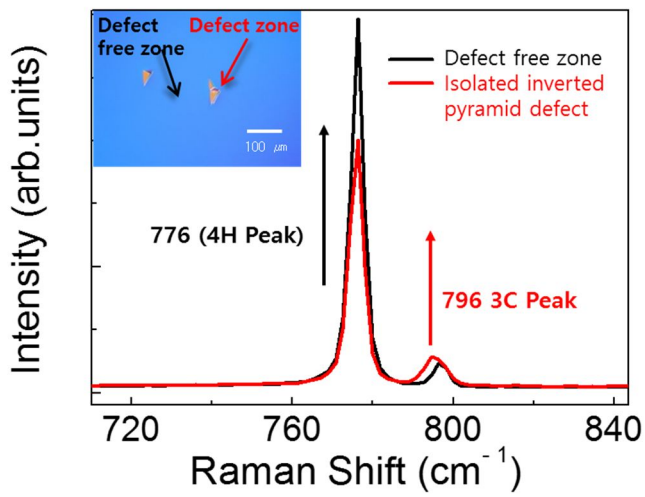


Fig. 4.13. Micro-Raman spectra of the defect free zone and isolated inverted pyramid defect. Inset image is the Nomarski image of the inverted pyramid defect.

#### **4.1.5. Background doping concentration and the growth rate of two polar face substrates**

The background doping concentration of epilayers was determined from capacitance-voltage (C-V) measurements of Ni/SiC Schottky diodes (contact diameter: 300  $\mu\text{m}$ ). Under the optimal condition for Si-face substrates (growth temperature: 1400  $^{\circ}\text{C}$ , flow rate: 10 sccm), background doping concentration of grown epilayer was  $1.67 \times 10^{16} \text{ cm}^{-3}$ , whereas the optimal condition for C-face, whose temperature is 1500  $^{\circ}\text{C}$  and the flow rate is 5 sccm, was  $2.04 \times 10^{16} \text{ cm}^{-3}$ . The result shows higher value of background doping concentration on C-face than Si-face, because the difference between face polarities leads to the easier incorporation of N-impurity. [9] The absolute background doping level is relatively higher than  $\sim 10^{14} \text{ cm}^{-3}$  of the SiC epilayers grown by using  $\text{SiH}_4$  and  $\text{C}_3\text{H}_8$ . [28] This high unintentional doping concentration may be attributed to the impurity of the precursor and the SiC-coated graphite susceptor used in this study. To observe the thickness of epitaxial layers, SEM was utilized to reveal a little increase on growth rate with higher temperature and flow rate of BTMSM carrier gas for both C and Si-faces, although overall level of growth rate was low in this study. In this study, we used BTMSM source under cold-wall reactor, therefore resulted low growth rate about 1.0  $\mu\text{m/hr}$ . However, in the follow-up research, we observed that the growth rate of SiC epilayer on Si-face substrate increased up to  $\sim 5.0 \mu\text{m/hr}$  when using a hot-wall reactor; growth temperature was 1425  $^{\circ}\text{C}$  and the flow rate was 10 sccm. Therefore, it

is assumed that the type of reactor also affects the growth rate of SiC epilayer.

## **4.2. 4H-SiC Epitaxial Growth on SiC substrates**

### **with Various Off-angles using BTMSM**

#### **4.2.1. Introduction**

SiC has shown significant promise for a wide range of electronic device applications, which cannot be achieved by traditional semiconductors. [29] As a result of intensive research efforts in recent years, SiC material quality has been improved to a point where high-performance SiC-based devices are commercially available, including Schottky rectifiers and metal-semiconductor field-effect transistors (MESFET). [30] Forward voltage instability has been a major issue in developing high-voltage bipolar devices in SiC. This instability is caused by the expansion of stacking faults under forward bias conditions. Stacking faults are known to originate from basal plane dislocations (BPDs) that exist in the substrate prior to epigrowth, and then extend into the epilayer during growth. [31] Techniques have been developed to alleviate the forward voltage instability problem. Continuous growth of active device regions has shown to prevent the introduction of interfacial BPDs. [32] Thicker substrate buffer and anode layers have been shown to isolate the device regions with a high level of conductivity modulation from the regions of epilayer with very high BPD densities, and hence to minimize the forward voltage drift. [30]

Research has found that BPDs propagating from substrates can be converted to threading edge dislocations during homoepitaxial growth. [33] Conversion efficiency can be improved by optimization of epitaxial growth processes or by certain pregrowth treatments, such as KOH etching. [30,34] SiC substrates are usually off-cut a few degrees from the (0001) plane to facilitate step-controlled epitaxial growth. It has been known for some time that epitaxial growth on 4H-SiC substrates with 8° off-cut toward the (11-20) direction yields fewer surface defects. However, a larger off-angle reduces the number of wafers that can be sliced from a single boule, which becomes more problematic as wafer diameter scales up. Recently, epitaxial growth on low off-angle substrates has been further explored. [35,36] The beneficial effects of low off-cut angle on BPD conversion have also been realized. [37] However, studies on the effects of off-cut angles on epitaxial growth, especially on BPD reduction, are limited in literature. [35-40] Kojima et al. studied the epitaxial growth of 4H-SiC on on-axis C-face substrates and found that the appearance of BPD can be prevented by using an on-axis substrate. [35] However, epitaxial growth of 4H-SiC on a Si-face on-axis substrate is unpractical due to the difficulty in achieving polytype stability. [38] Tsuchida et al. studied BPD densities on epilayers grown on 3.5° off-angle Si-face substrates, and a reduction of BPD densities has been observed under certain growth conditions. [37] In this chapter, epitaxial growth on Si-face 4H-SiC substrates with 8°, 4° off-cut angle, and on-axis substrates is performed in a home-made cold-wall chemical-CVD reactor.

## **4.2.2. 4H-SiC Epitaxial Layers Grown on 8° off-axis Substrates**

### **4.2.2.1. Morphological Characteristics**

In order to investigate the effect of the carrier gas flow rate on crystal growth through the BTMSM source in the bubbler, SiC thin films were first grown under the following condition: the deposition temperature was kept constant at 1400 °C and the BTMSM source flow rate was altered. The surface of the films grown at 15-20 sccm was milky to the naked eye, but those of the films grown at 5 and 10 sccm were specular. The effect of the BTMSM flow rate on the surface morphology of the thin film is clearly shown in the Nomarski micrographs of Fig. 4.14 and AFM images of Fig. 4.15. Although the surface morphology of the substrate and the film grown at a flow rate of 5 and 10 sccm are almost flat and featureless, the film grown at 15 sccm shows macroscopic step bunching, which implies that lateral growth from the steps occurs. Moreover, the film grown at a flow rate of 20 sccm had a very rough morphology and each flat area was separated by a deep groove.

In the second series of growth experiments, the BTMSM flow rate was kept constant at 10 sccm. All other conditions, except deposition temperature, were also fixed. Figure 4.14 and 4.15 shows the surface morphology of the films grown at deposition temperatures of 1240, 1280, 1320, 1360, 1400 and

1440 °C. The film grown at the low temperature of 1240 °C showed a typical polycrystalline morphology, which was most likely comprised of 3C-SiC and 4H-SiC polytypes. At 1280 °C, a wavy-like pattern was observed. Epitaxial films grown between 1320-1440 °C had a very smooth morphology.

Figure 4.16 shows the RMS roughness determined from the AFM image of the 4H-SiC epitaxial layer, which was grown at various growth temperatures and flow rate of BTMSM carrier gas. We evaluated the RMS roughnesses five times for each sample in order to ensure reliability. As the growth temperature decreases (1240 °C) or the carrier source flow rate increases above 15 sccm, the RMS roughness of the epitaxial layers increases by 10–100 times, rendering a non-specular and rough surface. It is assumed that there was insufficient step flow growth, and some parts of the terrace were affected by 3D nucleation and growth. Epitaxial layer grown on 8° off axis substrate at a relatively low temperature were of high quality and did not show surface morphological defects, and had a low surface roughness.

From the result above, it was found that the morphological stability was influenced not only by the degree of supersaturation of the source material but also by the growth temperature. In fact, the surface morphologies maintain a strong correlation to structural properties such as the polytype formation, which will be discussed as follows.

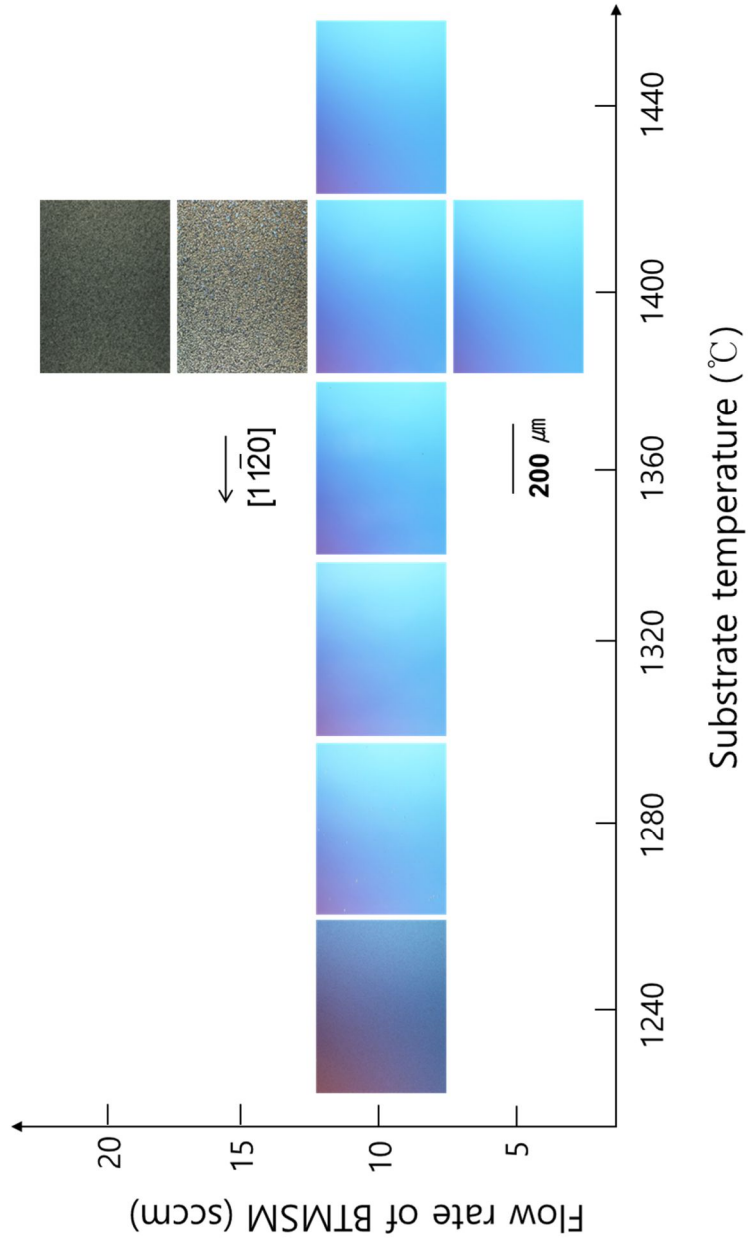


Fig. 4.14. Nomarski micrographs of 4H-SiC epitaxial layers grown at various growth conditions on 8° off-axis substrates.

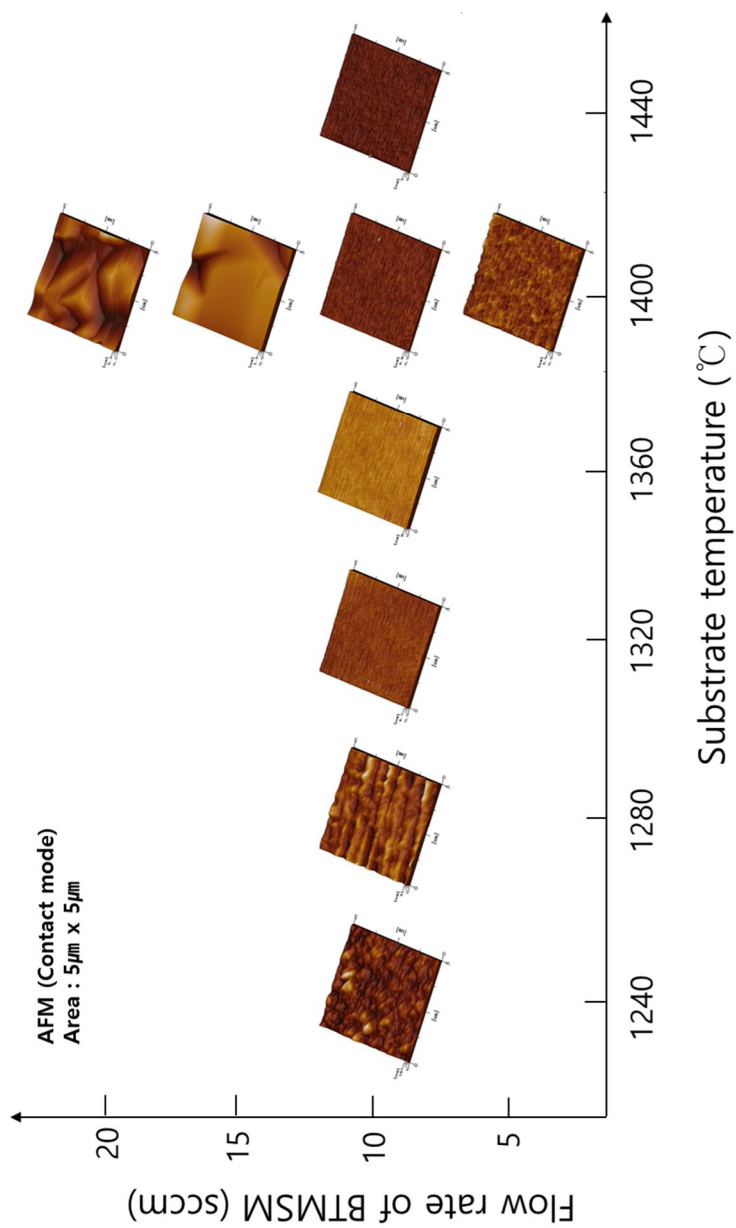


Fig. 4.15. AFM images of 4H-SiC epitaxial layers grown at various growth conditions on 8° off-axis substrates.

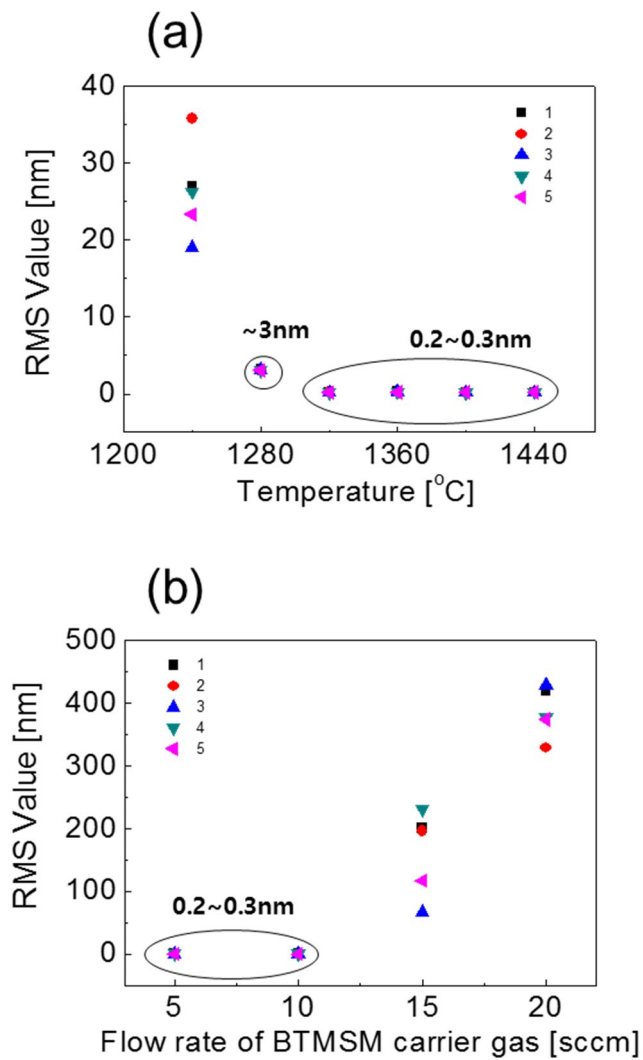


Fig. 4.16. RMS roughness of AFM image in 4H-SiC epitaxial layer, which was grown on 8° off-axis substrates at various (a) growth temperatures and (b) flow rates of BTMSM carrier gas.

#### 4.2.2.2. Structural Characteristics

The FWHM of the rocking curve of the epi-layer is influenced by x-ray extinction, crystal size, in addition to the threading dislocation density. In the case of a reasonably thick layer, the broadening due to crystal size can be neglected. The natural rocking curve width of the (0004) Bragg spot for perfect crystals, as determined by extinction, is also constant for the same x-ray geometry. Therefore, variation of the FWHM of rocking curve is mainly dominated by the threading dislocation density. Dislocations broaden the Bragg spot essentially in two ways: (a) they introduce a rotation of the crystal lattice that gives rise to local variations on the incidence angle such as tilt effect or mosaicity and (b) they are surrounded by a strain field, where the lattice parameter and the corresponding Bragg angle are non-uniform. [41]

In Fig. 4.17, rocking curve for substrate and epilayer grown at 1400 °C on 8° off-axis substrate are shown. The FWHM of the rocking curve of the epilayer was 14.76 arcsec, while that of the substrate was approximately 25 arcsec (Fig. 4.17). Therefore, the structural perfection of the epi-layer is superior to that of the substrate.

Figure 4.18 shows typical EBSD pattern of the SiC homoepitaxial film on 8° off-axis substrate grown at 1320 °C, clear Kikuchi lines were observed from the SiC films, indicating that the SiC films were monocrystalline. EBSD mapping of a 1×1 mm<sup>2</sup> scan area was performed in order to investigate the uniformity of the epi-layer. An epitaxial relationship with respect to the substrate was observed in all scanned areas.

Micro-Raman spectroscopy was conducted to verify the formation of the single polytype. As a result, we could observe that the 4H-SiC polytype was fairly well grown at a growth temperature of 1280–1440 °C, as seen in Figure 4.19. At a low carrier gas flow rate (< 15 sccm), the polytype of the epitaxial film was 4H-SiC, but at the higher flow rate (20sccm), the film contained some 3C-SiC polytype in addition to the 4H-SiC polytype (Fig. 4.20). This result can be explained in terms of supersaturation. At the low flow rate, the impinging atoms can reach the step so that the polytype of the substrate may be duplicated in the epi-layer. A higher supersaturation, however, can enhance the nucleation rate on the terraces, which produces the 3C-SiC polytype which is thermodynamically stable at the growth temperature, hence, resulting in the rough surface morphology. High temperatures are expected to be favorable for high quality epitaxy. At the temperature below 1240 °C, it was found that the 3C-SiC polytype was included in the as-grown films. Under this condition, a low growth temperature prevented the thin film from total replication of the substrate due to the suppressed surface migration of impinging atoms. As the growth temperature is increased, the 4H-SiC crystallinity is improved.

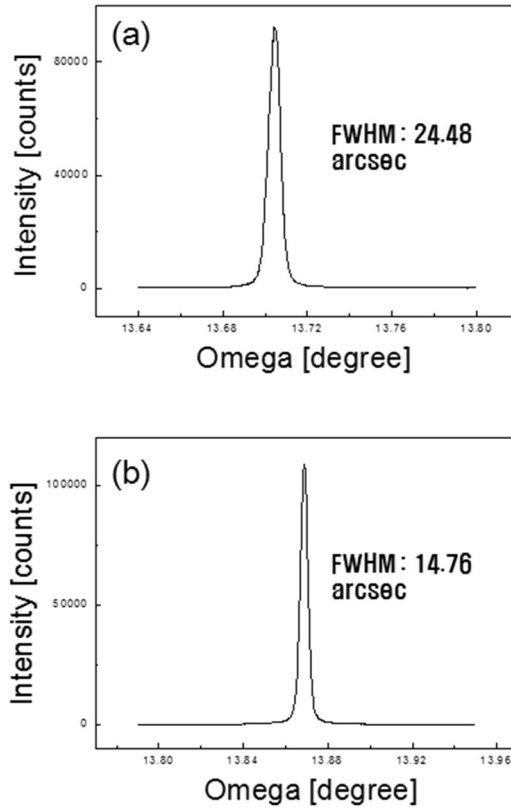


Fig. 4.17.  $\omega$ -Rocking curve for (a) substrate and (b) epilayer grown on  $8^\circ$  off-axis substrate at  $1400^\circ\text{C}$ .

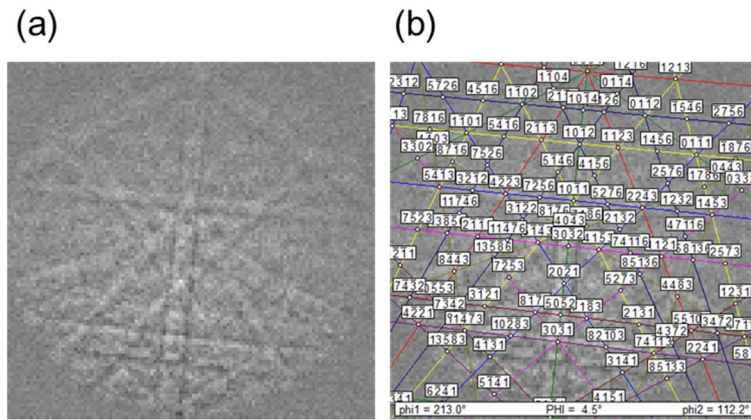


Fig. 4.18. Typical EBSD pattern of the SiC homoepitaxial film on 8° off-axis substrate grown at 1320 °C. (a) Kikuchi diffraction pattern of EBSD, and (b) indexed EBSD pattern.

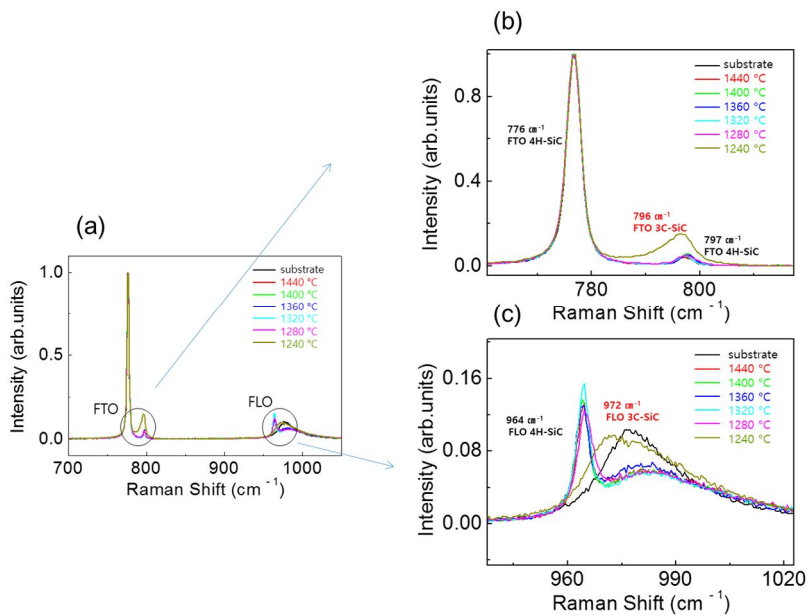


Fig. 4.19. (a) Micro-Raman spectra (FTO, FLO phonon mode) of various growth temperatures for epilayers on  $8^\circ$  off-axis substrates. Magnified view of (b) FTO phonon mode (C) FLO phonon mode.

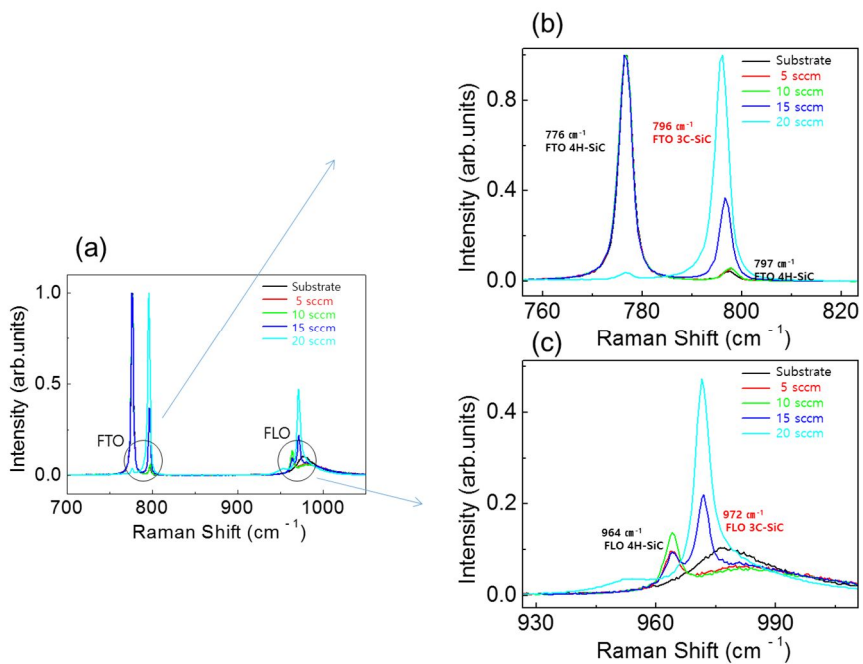


Fig. 4.20. (a) Micro-Raman spectra (FTO, FLO phonon mode) of various flow rates of BTMSM carrier gas for epilayers on  $8^\circ$  off-axis substrates. Magnified view of (b) FTO phonon mode (C) FLO phonon mode.

### 4.2.3. 4H-SiC Epitaxial Layers Grown on 4° off-axis Substrates

#### 4.2.3.1. Morphological Characteristics

In order to investigate the effect of the carrier gas flow rate on crystal growth through the BTMSM source in the bubbler, SiC thin films were first grown under the following condition: the deposition temperature was kept constant at 1400 °C and the BTMSM source flow rate was altered. The surface of the films grown at 15-20 sccm was milky to the naked eye, but those of the films grown at 5 and 10 sccm were specular. The effect of the BTMSM flow rate on the surface morphology of the thin film is clearly shown in the Nomarski micrographs of Fig. 4.21 and AFM images of Fig. 4.22. Although the surface morphology of the substrate and the film grown at a flow rate of 5 and 10 sccm are almost flat and featureless, the film grown at 15 sccm shows macroscopic step bunching, which implies that lateral growth from the steps occurs. Moreover, the film grown at a flow rate of 20 sccm had a very rough morphology and each flat area was separated by a deep groove.

In the second series of growth experiments, the BTMSM flow rate was kept constant at 10 sccm. All other conditions, except deposition temperature, were also fixed. Figure 4.21 and 4.22 shows the surface morphology of the films grown at deposition temperatures of 1240, 1280, 1320, 1360, 1400 and 1440 °C. The film grown at the low temperature of 1280 °C showed a typical polycrystalline morphology, which was most likely comprised of 3C-SiC and 4H-SiC polytypes. Epitaxial films grown between 1320-1440 °C had a very

smooth morphology.

Figure 4.23 shows the RMS roughness determined from the AFM image of the 4H-SiC epitaxial layer, which was grown at various growth temperatures and flow rate of BTMSM carrier gas. We evaluated the RMS roughnesses five times for each sample in order to ensure reliability. As the growth temperature decreases (1280 °C) or the carrier source flow rate increases above 15 sccm, the RMS roughness of the epitaxial layers increases by 10–100 times, rendering a non-specular and rough surface. It is assumed that there was insufficient step flow growth, and some parts of the terrace were affected by 3D nucleation and growth. Epitaxial layer grown on 4° off axis substrate at a relatively low temperature were of high quality and did not show surface morphological defects, and had a low surface roughness.

From the result above, it was found that the morphological stability was influenced not only by the degree of supersaturation of the source material but also by the growth temperature. In fact, the surface morphologies maintain a strong correlation to structural properties such as the polytype formation, which will be discussed as follows.

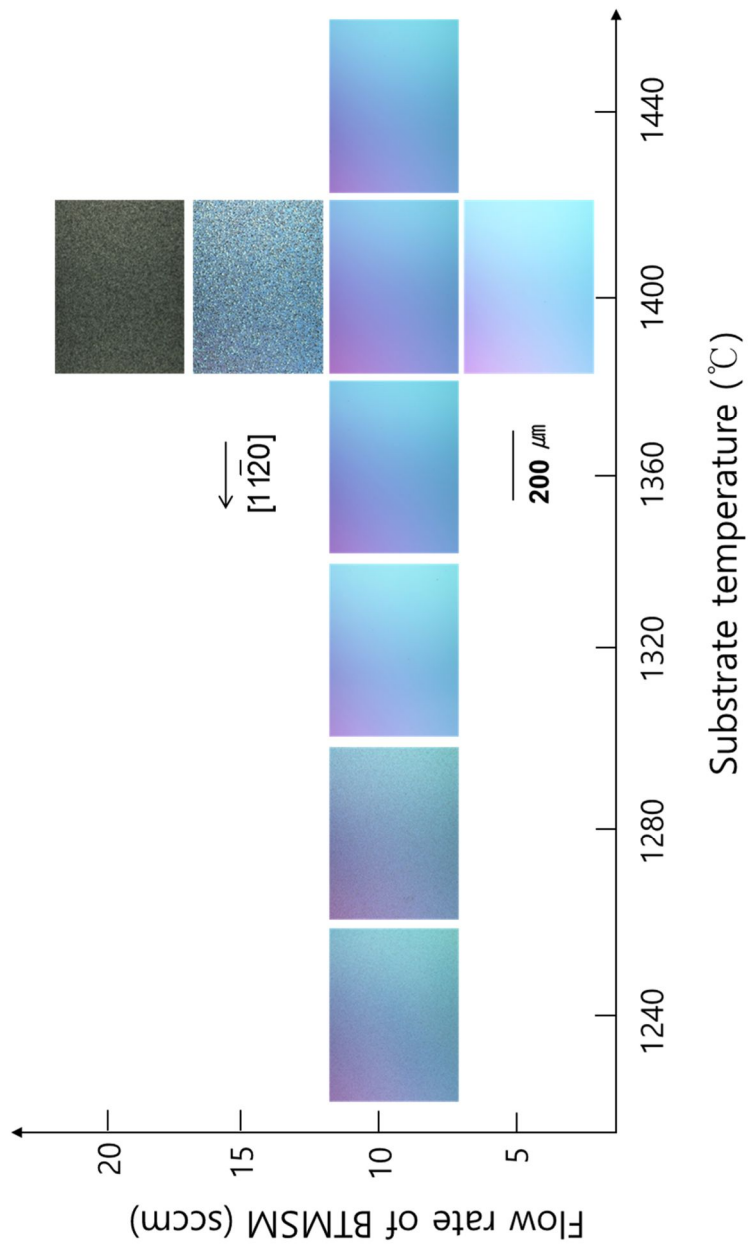


Fig. 4.21. AFM images of 4H-SiC epitaxial layers grown at various growth conditions on  $4^\circ$  off-axis substrates.

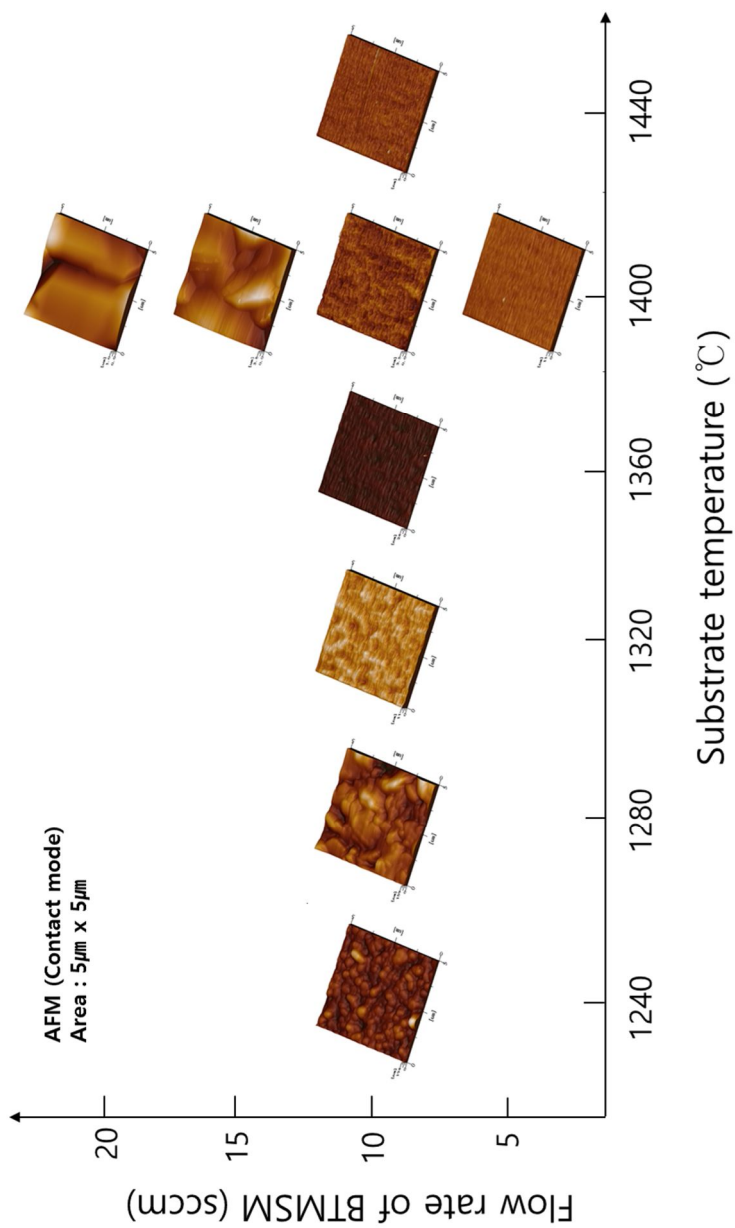


Fig. 4.22. Nomarski micrographs of 4H-SiC epitaxial layers grown at various growth conditions on 4 $^{\circ}$  off-axis substrates.

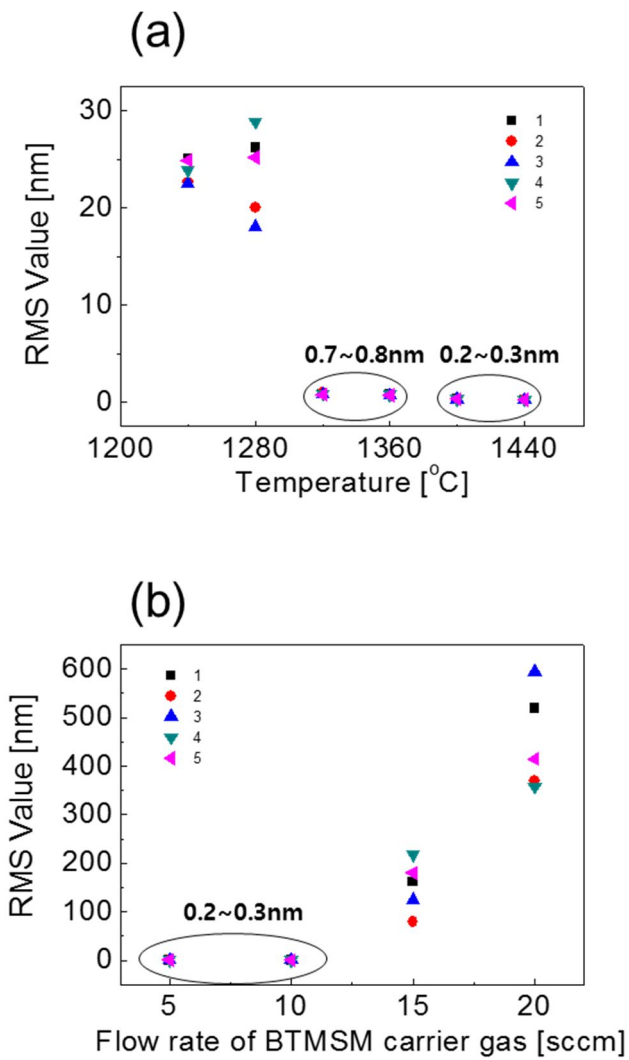


Fig. 4.23. RMS roughness of AFM image in 4H-SiC epitaxial layer, which was grown on 4° off-axis substrates at various (a) growth temperatures and (b) flow rates of BTMSM carrier gas.

#### 4.2.3.2. Structural Characteristics

In Fig. 4.24, rocking curve for substrate and epilayer grown at 1400 °C on 4° off-axis substrate are shown. The FWHM of the rocking curve of the epilayer was 16.56 arcsec, while that of the substrate was 20.88 arcsec (Fig. 4.15). Therefore, the structural perfection of the epilayer is superior to that of the substrate.

Figure 4.25 shows typical EBSD pattern of the SiC homoepitaxial film on 4° off-axis substrate grown at 1400 °C, clear Kikuchi lines were observed from the SiC films, indicating that the SiC films were monocrystalline. EBSD mapping of a 1×1 mm<sup>2</sup> scan area was performed in order to investigate the uniformity of the epilayer. An epitaxial relationship with respect to the substrate was observed in all scanned areas.

Micro-Raman spectroscopy was conducted to verify the formation of the single polytype. As a result, we could observe that the 4H-SiC polytype was fairly well grown at a growth temperature of 1320–1440 °C, as seen in Figure 4.26. At a low carrier gas flow rate (< 15 sccm), the polytype of the epitaxial film was 4H-SiC, but at the higher flow rate (20sccm), the film contained some 3C-SiC polytype in addition to the 4H-SiC polytype (Fig. 4.27). This result can be explained in terms of supersaturation. At the low flow rate, the impinging atoms can reach the step so that the polytype of the substrate may be duplicated in the epilayer. A higher supersaturation, however, can enhance the nucleation rate on the terraces, which produces the 3C-SiC polytype which is thermodynamically stable at the growth temperature, hence, resulting in the

rough surface morphology. High temperatures are expected to be favorable for high quality epitaxy. At the temperature below 1280 °C, it was found that the 3C-SiC polytype was included in the as-grown films. Under this condition, a low growth temperature prevented the thin film from total replication of the substrate due to the suppressed surface migration of impinging atoms. As the growth temperature is increased, the 4H-SiC crystallinity is improved.

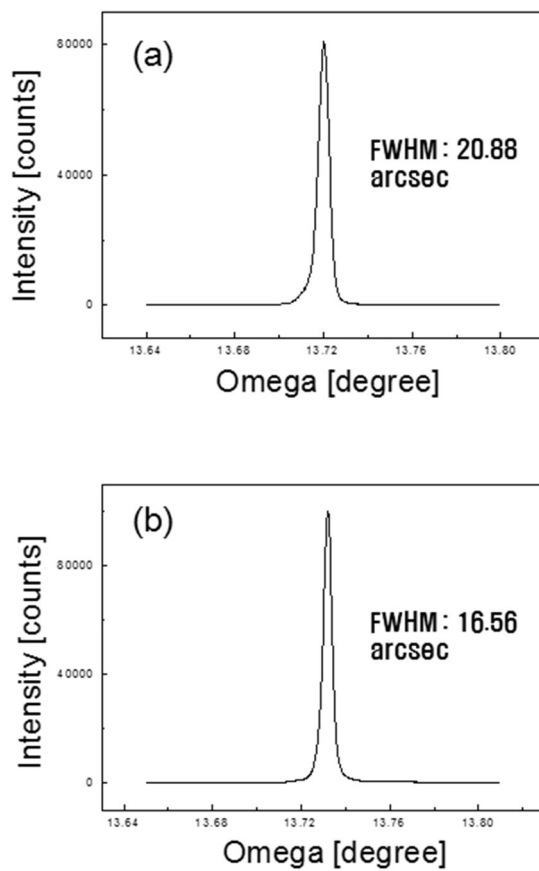


Fig. 4.24. w-Rocking curve for (a) substrate and (b) epilayer grown on 8° off-axis substrate at 1400 °C.



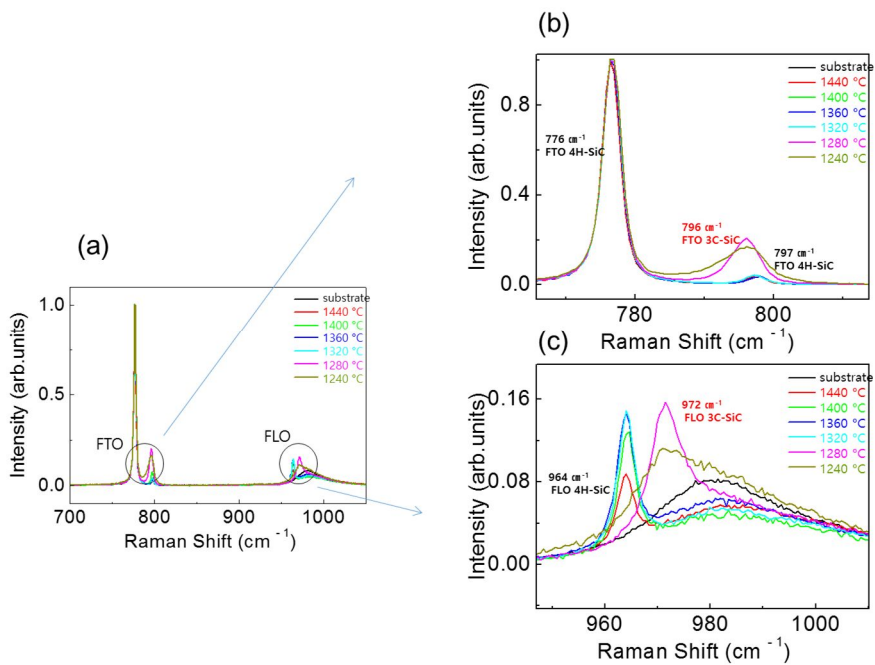


Fig. 4.26. (a) Micro-Raman spectra (FTO, FLO phonon mode) of various growth temperatures for epilayers on  $4^\circ$  off-axis substrates. Magnified view of (b) FTO phonon mode (C) FLO phonon mode.

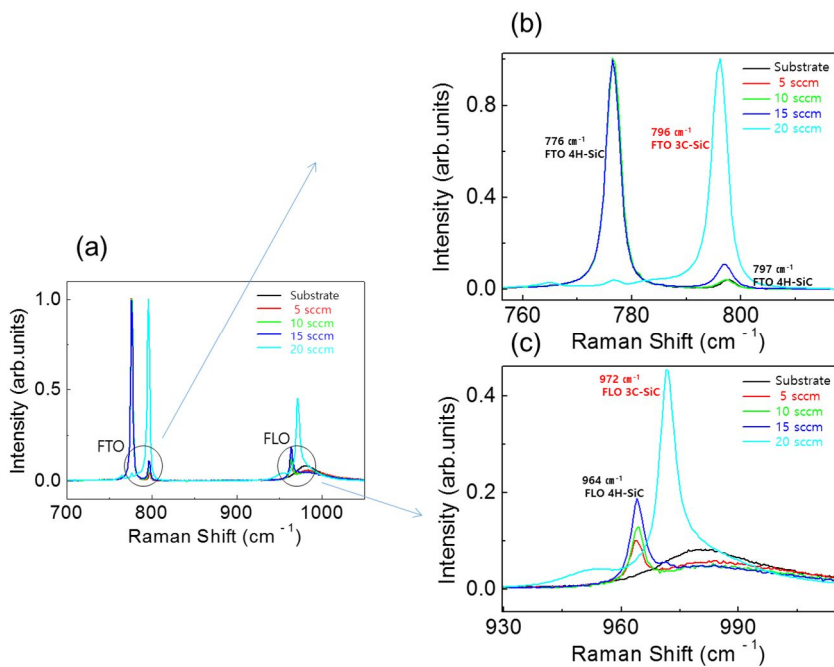


Fig. 4.27. (a) Micro-Raman spectra (FTO, FLO phonon mode) of various flow rates of BTMSM carrier gas for epilayers on 4° off-axis substrates. Magnified view of (b) FTO phonon mode (C) FLO phonon mode.

## 4.2.4. 4H-SiC Epitaxial Layers Grown on On-axis Substrates

### 4.2.4.1. In-situ Surface Preparation

A clean surface with reduced number of surface damages is the key to produce defect free homoepitaxial layers. [42] As received SiC samples are known to have polishing-related damages. It has been well known that, the growth on the imperfective substrate generates larger macro-steps or surface damages; the 3C-SiC inclusions originate at epi-substrate interface, substrate surface damages, or larger macro-steps, and eventually grow to cover the larger area of the surface.

Figure 4.28 presents SEM and AFM images of on-axis Si-face 4H-SiC wafer and hydrogen etched wafers obtained at 1470 °C, 10 min. Figure 4.28 (a) and (b) present the bare substrates of the Si-face, which shows native scratches with RMS roughness of 1.44 nm. Figure 4.28 (c) and (d) present the substrate after processing H<sub>2</sub> etching to have featureless surface. Figure 4.28 (d) presents regular stripe like shape, with RMS roughness of 0.5 nm. Figure 4.29 shows the AFM and the peak to valley of the height profile of the AFM image on H<sub>2</sub> etched surface at 1470 °C on on-axis 4H-SiC Si-face substrates. Figure 4.29 (b) shows that the atomic step of etched surface was 1 nm height. The result revealed a step with clear and even shape, which is different from the aforementioned off-axis substrate formed by H<sub>2</sub> etching. Since H<sub>2</sub> etching originally aims to develop the steps even, native scratches were removed, and RMS roughness was lowered from 1.44 to 0.5nm. Therefore, the surface

preparation was performed under the temperature of 1470°C for 10 minutes, before the epitaxial growth.

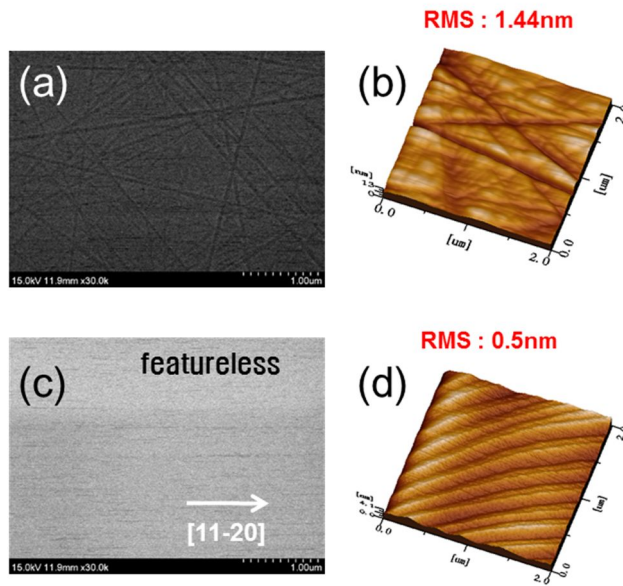


Fig. 4.28. SEM and AFM images of (a), (b) bare on-axis, (c), (d) treated on-axis substrate.

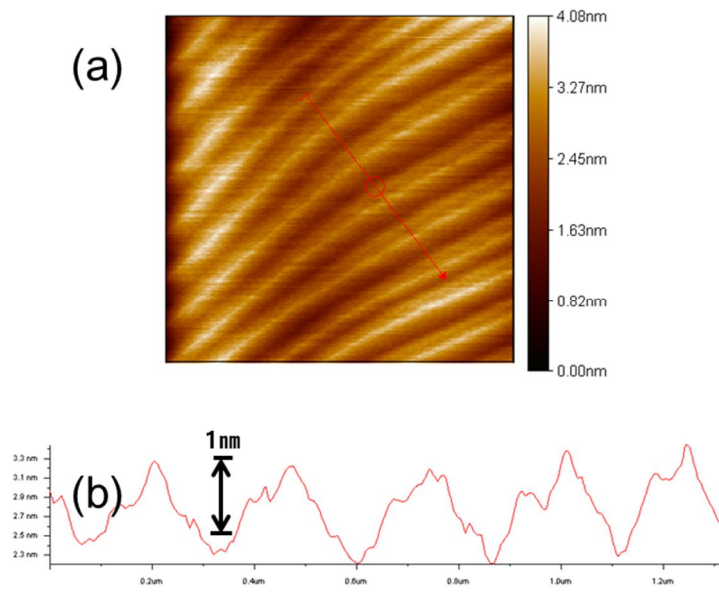


Fig. 4.29. (a) AFM image, and (b) the peak to valley of the height profile of the AFM image of 4H-SiC on-axis substrate after H<sub>2</sub> etching at 1470 °C.

#### 4.2.4.2. 4H-SiC Epitaxial Growth on On-axis Substrates using BTMSM

Figure 4.30 shows the AFM images of the 4H-SiC epitaxial layers, which were grown on the Si-face on-axis substrate at 1240-1440 °C with BTMSM carrier gas flow rate of 10 sccm. Although the surface morphology of the epitaxial layers grown at 1360-1440 °C (Fig. 4.30 (d-f)) are almost flat showing RMS roughness ranges from 0.1 nm to 0.3 nm (Fig. 4.31), the epitaxial layers grown under 1320 °C (Fig. 4.30 (a-c)) show rough morphologies, and each of flat areas are separated by a deep groove with RMS roughness of 29 nm–30 nm (Fig. 4.31).

Figure 4.32 shows the Nomaski micrographs of the 4H-SiC epitaxial layers grown on a Si-face on-axis substrates at 1240-1440 °C when the BTMSM carrier gas flow rate was 10 sccm. As presented in Figure 4.32, epitaxial grown layers were not obtained under 1320 °C, whereas smooth epitaxial grown layers could be observed when it was over 1360 °C. Whereas the RMS roughness grown at 1360~1440 °C reveals fine quality, macroscopic image of the surfaces which were observed by NMS image shows the smooth surface were divided into some blocks.

Figure 4.33 shows the Nomaski micrographs of the 4H-SiC epitaxial layers grown on a Si-face on-axis substrates at 1480 and 1550 °C when the BTMSM carrier gas flow rate was 10 sccm. When growth temperature became 1480 °C, we conducted island growth, which possesses a number of blocks as shown in Figure 4.33, but hexagonal shapes were sparsely appeared. In addition,

epilayer began to have smooth surface in macroscopic view as well as a shape of continuous chain of hexagonal-shape, when the temperature reached 1550 °C. Nominally on-axis (0001) substrates as supplied from manufacturers should not have any tilt from the basal plane, therefore epitaxial growth should in principle occur only via three-dimensional growth (islands formation at screw dislocation, and their expansion through lateral step growth at the islands walls). [43]



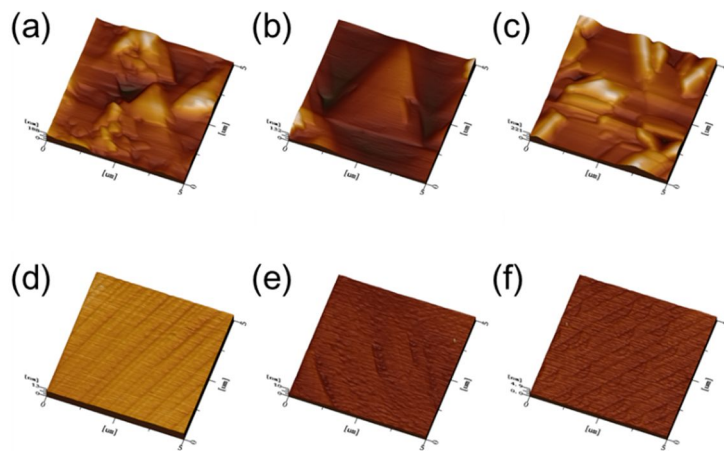


Fig. 4.30. AFM images of 4H-SiC epitaxial layer grown at (a) 1240 (b) 1280 (c) 1320 (d) 1360 (e) 1400 (f) 1440 °C on Si-face on-axis substrates. (BTMSM Source flow rate: 10 sccm)

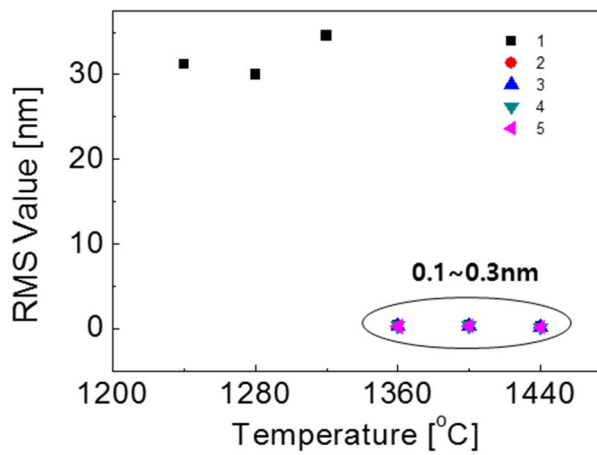


Fig. 4.31. RMS roughness of AFM image in 4H-SiC epitaxial layer, which was grown on Si-face on-axis substrates at various growth temperatures with flow rates of BTMSM carrier gas of 10 sccm.

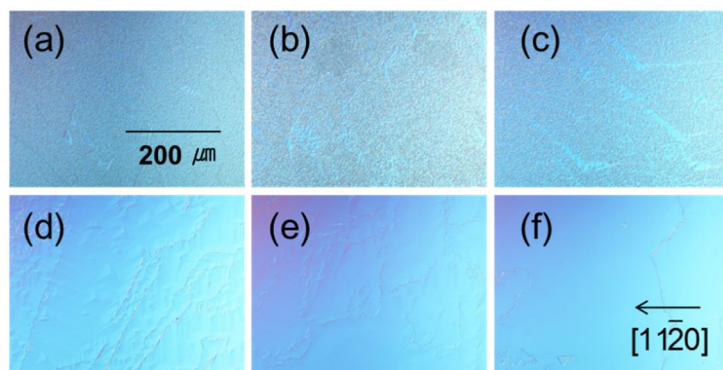


Fig. 4.32. NMS images of 4H-SiC epitaxial layer grown at (a) 1240 (b) 1280 (c) 1320 (d) 1360 (e) 1400 (f) 1440 °C on Si-face on-axis substrates. (BTMSM Source flow rate: 10 sccm)

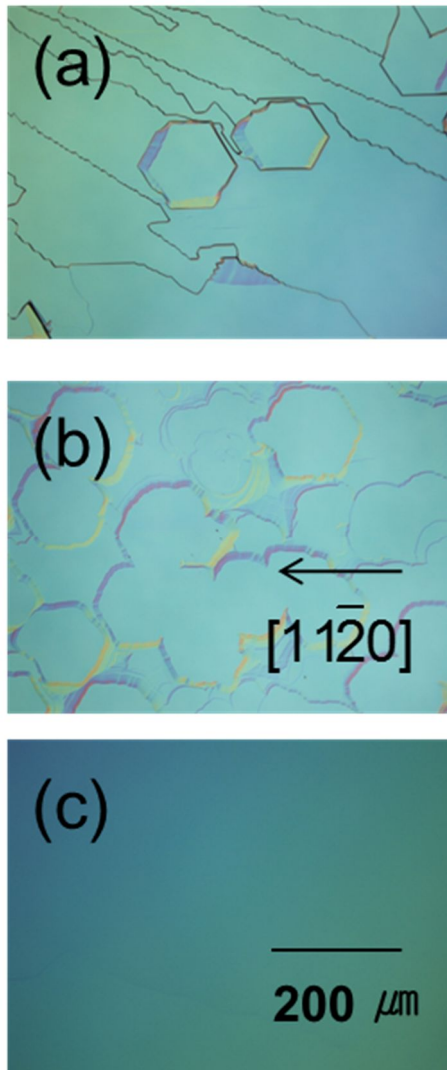


Fig. 4.33. NMS images of 4H-SiC epitaxial layer grown at (a) 1480 (b) 1550 (c) 1550 °C (another part) on Si-face on-axis substrates. (BTMSM Source flow rate: 10 sccm)

Micro-Raman analysis and Electron backscatter diffraction (EBSD) was conducted to verify the formation of the single polytype. As a result, we could observe that the epitaxial layers contained some 3C-SiC polytype at ranges of 1240-1440 °C of the growth temperature (Fig. 4.34). Since the steps cannot be generated on the on-axis substrate surface intentionally, it is difficult to control steps while epitaxial growth, which generates 3C-SiC inclusion. When using on-axis substrates the polytype stability is thus difficult to maintain and typically can result in high concentration of 3C polytype inclusions. The origin of the 3C nucleation can be randomly distributed on the substrate and thus lower the effective usable area of the 4H material. At the growth temperature (typically 1500-1650 °C) [43] the low diffusion length of the adatoms will favor the formation of 3C inclusions. At lower growth temperatures (typically below 1500 °C) the 3C polytype of SiC is more thermodynamically stable [43] and twinned crystalline 3C epilayers were obtained during epitaxy.

When epilayer grows at 1480 °C using BTMSM, 4H-SiC was grown to a hexagonal shape, and nearby blocks were composed of 3C-SiC (Fig. 4.35-36). This means the application of BTMSM source enabled growth of 4H-SiC at a relatively lower temperature of 1480 °C, which is the same as the polytype of on-axis substrate. EBSD was used to evaluate the presence of double-position-boundaries (DPBs), indicating that the 3C-1 and 3C-2 present the domains with two possible orientations tilted with 60 °C, as illustrated in Fig. 4.36. Moreover, through EBSD mapping analysis, we could identify that 4H-SiC could grow at 1550 °C, satisfying stability of 4H-SiC polytype for 100%

(Fig. 4.37-38). The whole area was grown to 4H-SiC epilayer, revealing two types of surface regions which are hexagonal chain-shape and smooth surface. The smooth surface could be obtained due to high dislocation density of the area when compared to the hexagonal chain region. Increasing the growth temperature helps to enhance the mobility of the adatoms on the surface, lowering the probability for a two dimensional nucleation of 3C.

Figure 4.39 shows SEM image, AFM image, and the peak to valley of the height profile of the AFM image of 4H-SiC epitaxial layer grown at 1550 °C with source flow rate of BTMSM of 10 sccm on Si-face on-axis substrate. The nearby interacting spirals meet each other perfectly and no defect or foreign polytype inclusions were found at the interfaces. AFM image taken from area, shows that the surface is covered with micro-steps of unit cell height with a typical spiral-shaped geometry (Fig. 4.39). Figure 4.39 (d) shows that the grown epitaxial layer which showing spiral growth have a 0.1 nm height of each steps. In the case of normal off-cut substrate, the growth is mainly governed by the step-flow while in the case of nominally on-axis surface spiral growth occurs via micro-steps provided by screw dislocations intersecting the surface [44].

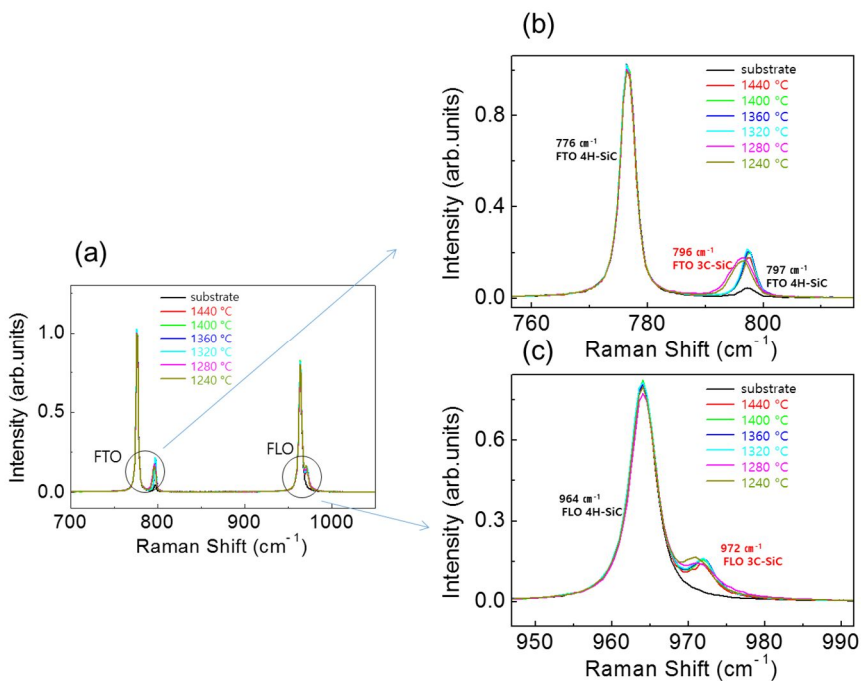


Fig. 4.34. (a) Micro-Raman spectra (FTO, FLO phonon mode) of various growth temperatures for epilayers grown on Si-face on-axis substrates. Magnified view of (b) FTO phonon mode (C) FLO phonon mode.

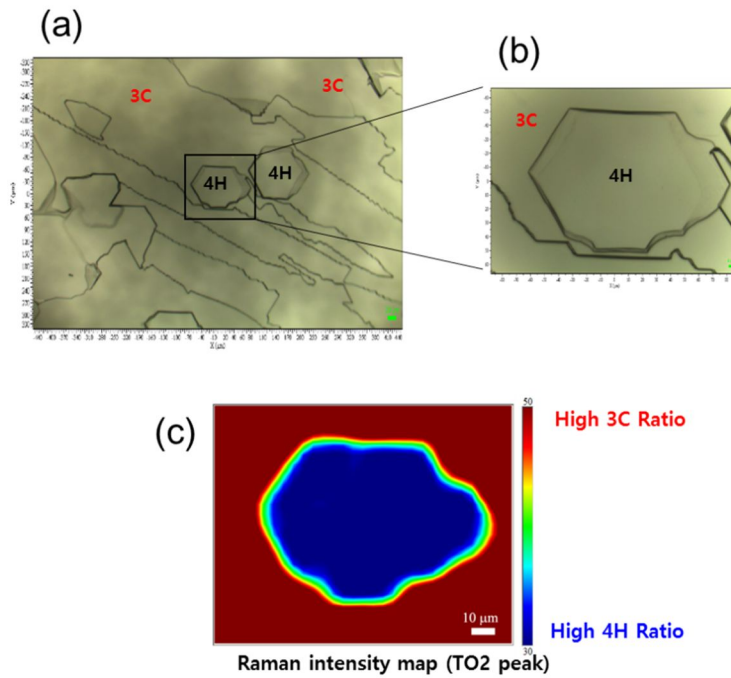


Fig. 4.35. 4H-SiC epitaxial layer grown at 1480 °C on Si-face on-axis substrates. (BTMSM Source flow rate: 10 sccm) (a) The optical image, (b) magnified image of (a), (c) Raman intensity map of the peak at  $972\text{ cm}^{-1}$  (3C-LO phonon mode) for the shown in (b).

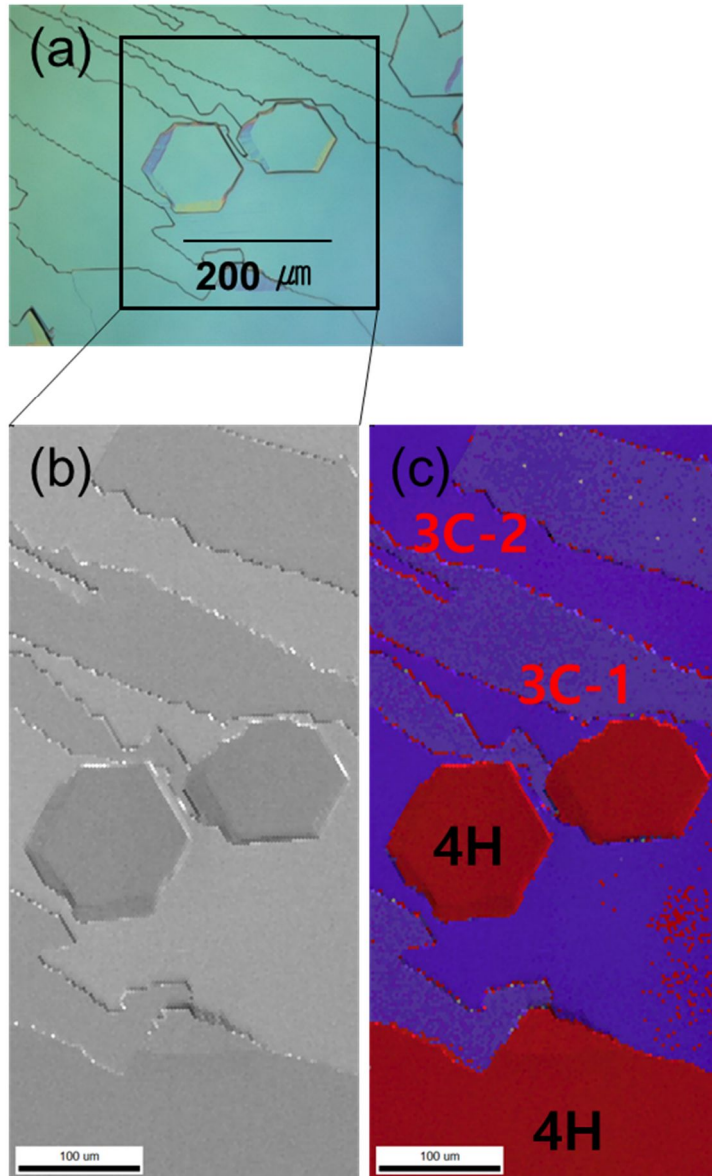


Fig. 4.36. EBSD mapping of the SiC epitaxial layer on on-axis substrate grown at 1480 °C. (a) NMS image, (b) SEM image, and (c) EBSD mapping image for the shown in (b).

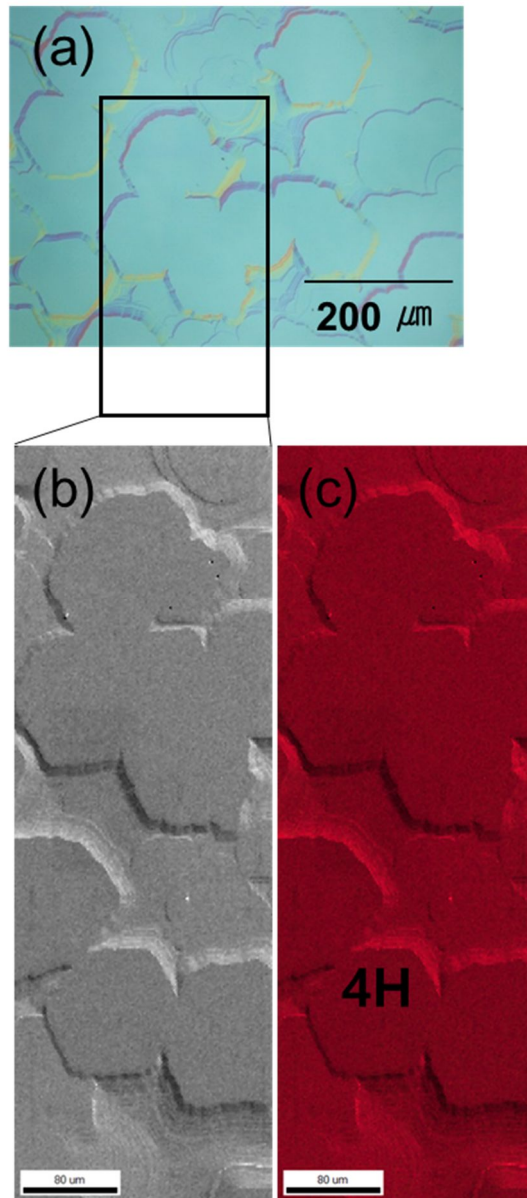


Fig. 4.37. EBSD mapping of the SiC epitaxial layer on on-axis substrate grown at 1550 °C. (a) NMS image, (b) SEM image, and (c) EBSD mapping image for the shown in (b).

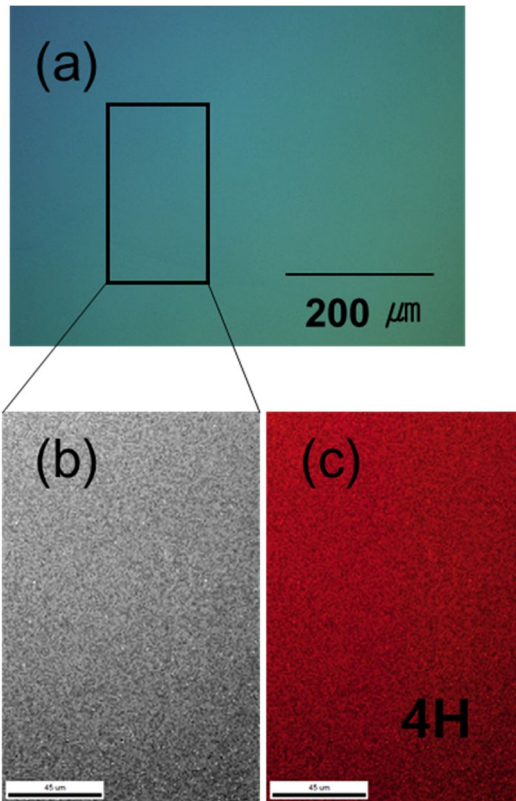


Fig. 4.38. EBSD mapping of the SiC epitaxial layer on on-axis substrate grown at 1550 °C (another part). (a) NMS image, (b) SEM image, and (c) EBSD mapping image for the shown in (b).

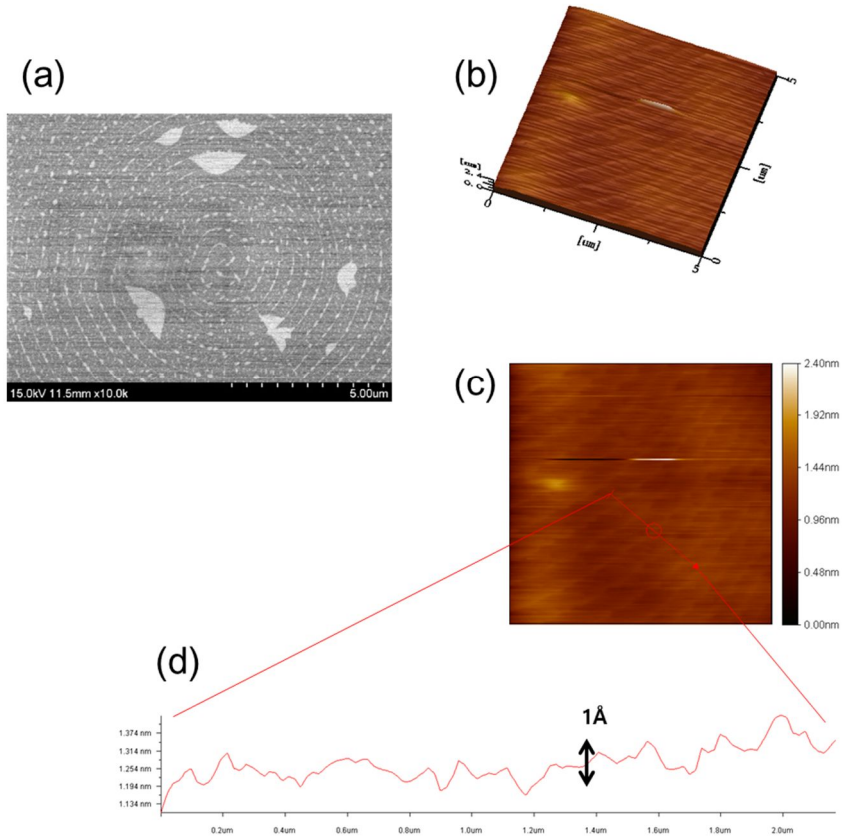


Fig. 4.39. (a) SEM, (b) AFM image, (c) 2D image of AFM, and (d) the peak to valley of the height profile of the AFM image of 4H-SiC epitaxial layer grown at 1550 °C on Si-face on-axis substrate. (BTMSM Source flow rate: 10 sccm)

#### 4.2.4.3. Growth Rate

The thickness of epilayers were observed by the scanning electron microscopy. Figure 4.40 shows cross-section SEM micrograph of 4H-SiC epitaxial layers grown on Si-face on-axis substrates for various growth conditions. All of the samples were grown for 2 hours. When the flow rate of BTMSM carrier gas was 10 sccm and growth temperature of 1380 °C, epitaxial layer grew 1.7  $\mu\text{m}$ , while the samples were grown 1.82  $\mu\text{m}$  and 2.09  $\mu\text{m}$  on 1470 °C and 1550 °C respectively. The result reveals higher growth rate with higher temperature. We assume such result appeared since ad-atoms become mobile with higher rate. In addition, the epitaxial growth was 1.24  $\mu\text{m}$  when the growth temperature was 1470 °C and source flowrate was 5 sccm. Such low growth rate could have influenced by smaller amount of source from decomposition, which causes reaction on the surface in CVD growth environment.

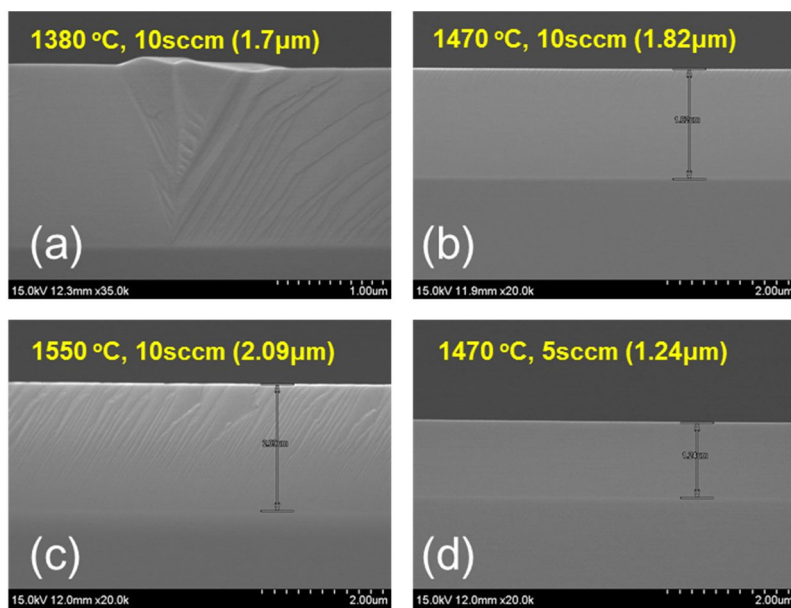


Fig. 4.40. Cross-section SEM micrograph of 4H-SiC epitaxial layers grown on Si-face on-axis substrates at various growth conditions.

## Bibliography

- [1] R. J. Trew, J. B. Yan, and P. M. Mock, *Proc. IEEE*, **79**, 598 (1991).
- [2] B. J. Baliga, *Proc. IEEE*, **82**, 1112 (1994).
- [3] K. V. Vassilevski, K. Zekentes, A. V. Zorenko, and L. P. Romanov, *Electron Device Lett., IEEE*, **21**, 485 (2000).
- [4] K. Kojima, H. Okumura, S. Kuroda, and K. Arai, *J. Cryst. Growth*, **269**, 367 (2004).
- [5] S. Nakamura, T. Kimoto, and H. Matsunami, *J. Cryst. Growth*, **256**, 347 (2003).
- [6] M. Suemitsu, Y. Miyamoto, H. Handa and A. Konno, *e-J. Surf. Sci. Nanotech.*, **7**, 311 (2009).
- [7] K. Volz, S. Schreiber, J. Gerlach, W. Reiber, B. Rauschenbach, B. Stritzker, W. Assmann, and W. Ensinger, *Mater. Sci. Eng., A*, **289**, 255 (2000).
- [8] H. Matsunami and T. Kimoto, *Mater. Sci. Eng., R*, **20**, 125 (1997).
- [9] K. Kojima, T. Suzuki, S. Kuroda, J. Nishio, and K. Arai, *Jpn. J. Appl. Phys.*, **42**, L637 (2003).
- [10] K. Fukuda, M. Kato, K. Kojima, and J. Senzaki, *Appl. Phys. Lett.*, **84**, 2088 (2004).
- [11] K. Danno, T. Kimoto, K. Asano, Y. Sugawara, and H. Matsunami, *J. Electron. Mater.*, **34**, 324 (2005).
- [12] H. Tsuchida, I. Kamata, T. Miyanagi, T. Nakamura, K. Nakayama, R. Ishii, and Y. Sugawara, *Jpn. J. Appl. Phys.*, **44**, L806 (2005).
- [13] T. Kimoto, A. Itoh, and H. Matsunami, *Phys. Status Solidi B*, **202**, 247

(1997).

[14] G. Augustine, M. Hobgood, V. Balakrishna, G. Dunne, and R. Hopkins, *Phys. Status Solidi B*, **202**, 137 (1997).

[15] W. Bahng and H. J. Kim, *Appl. Phys. Lett.*, **69**, 4053 (1996).

[16] J. K. Jeong, H. J. Na, J. Choi, C. S. Hwang, H. J. Kim, and W. Bahng, *J. Cryst. Growth*, **210**, 629 (2000).

[17] H. K. Song, S. Y. Kwon, H. S. Seo, J. H. Moon, J. H. Yim, J. H. Lee, H. J. Kim, and J. K. Jeong, *Appl. Phys. Lett.*, **89**, 152112 (2006).

[18] N. Kubo, T. Kawase, S. Asahina, N. Kanayama, H. Tsuda, A. Moritani, and K. Kitahara, *Jpn. J. Appl. Phys.*, **43**, 7654 (2004).

[19] C. Sartel, V. Soulière, J. Dazord, Y. Monteil, I. El Harrouni, J. M. Bluet, and G. Guillot, *Mater. Sci. Forum*, **389-393** 263 (2002).

[20] V. Ramachandran, M. Brady, A. Smith, R. Feenstra, and D. Greve, *J. Electron. Mater.*, **27**, 308 (1998).

[21] C. Hallin, F. Owman, P. Mårtensson, A. Ellison, A. Konstantinov, O. Kordina, and E. Janzén, *J. Cryst. Growth*, **181**, 241 (1997).

[22] A. Shrivastava, P. Muzykov, J. Caldwell, and T. Sudarshan, *J. Cryst. Growth*, **310**, 4443 (2008).

[23] Y. Ishida, T. Takahashi, H. Okumura, K. Arai, and S. Yoshida, *Mater. Sci. Forum*, **600-603** 473 (2009)

[24] R. L. Schwoebel and E. J. Shipsey, *J. Appl. Phys.*, **37**, 3682 (1966).

[25] G. Ehrlich and F. Hudda, *J. Chem. Phys.*, **44**, 1039 (1966).

[26] T. Kimoto and H. Matsunami, *J. Appl. Phys.*, **78**, 3132 (1995).

[27] V. F. Tsvetkov, S. T. Allen, H. S. Kong, and C. H. Carter, *Inst. Phys.*

Conf. Ser. **142**, 17 (1996).

[28] K. Wada, T. Kimoto, K. Nishikawa, and H. Matsunami, *J. Cryst. Growth*, **291**, 370 (2006).

[29] M. A. Capano and R. J. Trew, *MRS Bull.* **22**, 19 (1997).

[30] J. J. Sumakeris, J. R. Jenny, and A. R. Powell, *MRS Bull.* **30**, 280 (2005).

[31] H. Jacobson, J. Birch, R. Yakimova, M. Syvajarvi, J. P. Bergman, A. Ellison, T. Tuomi, and E. Janzen, *J. Appl. Phys.* **91**, 6354 (2002).

[32] J. J. Sumakeris, M. Das, H. M. Hobgood, S. G. Muller, M. J. Paisley, S. Ha, M. Skowronski, J. W. Palmour, and C. H. Carter, *Mater. Sci. Forum*, **457–460**, 1113 (2004).

[33] S. Ha, P. Mieszkowski, M. Skowronski, and L. B. Rowland, *J. Cryst. Growth* **244**, 257 (2002).

[34] T. Ohno, H. Yamaguchi, S. Kuroda, K. Kojima, T. Suzuki, and K. Arai, *J. Cryst. Growth* **271**, 1 (2004).

[35] K. Kojima, H. Okumura, S. Kuroda, D. Arai, A. Ohi, and H. Akinaga, *Mater. Sci. Forum* **483**, 93 (2005).

[36] S. Nakamura, T. Kimoto, and H. Matsunami, *Mater. Sci. Forum* **457–460**, 163 (2004).

[37] A. Tsuchida, T. Miyanagi, I. Kamata, T. Nakamura, K. Izumi, K. Nakayama, R. Ishii, K. Asano, and Y. Sugawara, *Mater. Sci. Forum* **483**, 97 (2005).

[38] J. A. Powell, D. J. Larkin, P. B. Abel, L. Zhou, and P. Pirouz, *Proceedings*

of the Sixth International Conference on Silicon Carbide and Related

- Materials, Kyoto, Japan, 1995 \_IOP Publishing, Bristol, UK, p. 77. (1996).
- [39] H. Saitoh and T. Kimoto, Mater. Sci. Forum **483**, 89 (2005).
- [40] K. Masahara et al., Mater. Sci. Forum **353–356**, 135 (2001).
- [41] J. K. Jeong, Ph. D. Dissertation, Department of Material Science and Engineering, Seoul National University, Seoul, Korea (2002).
- [42] J.A. Powell, J.B. Petit, J.H. Edgar, I.G. Jenkins, L.G. Matus, J.W. Yang, P. Pirouz, W.J. Choyke, L. Clemen and M. Yoganathan, Appl. Phys. Lett. **59**, p. 333. (1991).
- [43] A. Henry, S. Leone, X. Li, J. Hassan, O. Kordina, J.P. Bergman and E. Janzén, Research Signpost **37/661**, p. 97 (2012).
- [44] F.C. Frank, Acta Crystallogr. **4**, p. 497 (1951).

## 5. Conclusion

Silicon carbide is an attractive wide band gap semiconductor which can be applied in high temperature and high power environments. The commercialization of its large single-crystal wafer and excellent epitaxial growth technique provide a better candidate for application in high-power and high-frequency electronic devices compared with other wide-bandgap materials such as GaN, ZnO, and diamond. 4H-SiC is the most promising material for power devices application among various polytypes.

Homoepitaxial growth of SiC epitaxial layers on various substrates including 4H-SiC 4°, 8° off-axis, on-axis Si-face substrates, and C-faces substrates was carried out at temperature ranging from 1240 to 1550 °C and carrier gas flow rates of 5-20 sccm for the BTMSM source.

We particularly used BTMSM source on 4° off-axis substrate to compare the results from two different polarities of Si-face and C-face. Therefore, we could observe the effect of using BTMSM source on two polarities. In addition, characteristics of epitaxial layers grown on on-axis, 4°, and 8° off-axis substrates were also studied.

*In situ* H<sub>2</sub> etching and homoepitaxial growth of 4H-SiC have been carried out on 4° off-axis Si-face and C-face 4H-SiC substrates by low-pressure CVD. H<sub>2</sub> etching characteristics and epitaxial growth behaviors on two different polarities using a BTMSM were systematically analyzed and discussed. When the temperature of *in situ* H<sub>2</sub> etching was 1500 °C, the Si-face and C-face showed macro step-bunching and some clusters, respectively, whereas both

faces showed fairly good quality when treated at 1450 °C for 10 min. High-quality 4H-SiC epitaxial layers with less crystallographic defects and free of step-bunching were demonstrated on both Si-face and C-face substrates. The optimal growth temperature on the Si-face substrate was 1320-1400 °C with a BTMSM source flow rate of 5-10 sccm, while the growth temperature should be increased to 1500 °C on the C-face substrate with a lower source flow rate of 5 sccm. A mechanism for the observed generation of step-bunching and surface morphological defect on both substrates depending on the growth temperature and source flow rate was also proposed.

In the case of homoepitaxial growth on various off-angle substrates, it was found that the structure perfection of SiC epilayers is improved with higher temperature and lower flow rate of BTMSM. This growth behavior can be explained by the step-controlled epitaxy model.

At the on-axis substrate, since H<sub>2</sub> etching originally aims to develop the steps even, native scratches were removed, and RMS roughness was lowered from 1.44 to 0.5nm. Therefore, the surface preparation was performed under the temperature of 1470°C for 10 minutes, before the epitaxial growth. The grown epitaxial layer on on-axis substrate, which showing spiral growth have a 0.1 nm height of each steps. In the case of normal off-cut substrate, the growth is mainly governed by the step-flow while in the case of nominally on-axis surface spiral growth occurs via micro-steps provided by screw dislocations intersecting the surface. When growth temperature became 1480 °C on the nominally on-axis, we conducted island growth, which possesses a number of blocks, but hexagonal shapes were sparsely appeared.

In addition, epilayer began to have smooth surface in macroscopic view as well as a shape of continuous chain of hexagonal-shape, when the temperature reached 1550 °C. When epilayer grows at 1480 °C, 4H-SiC was grown to a hexagonal shape, and nearby blocks were composed of 3C-SiC. This means the application of BTMSM source enabled growth of 4H-SiC at a relatively lower temperature of 1480 °C, which is the same as the polytype of substrate. Moreover, we could identify that 4H-SiC could grow at 1550 °C, satisfying stability of 4H-SiC polytype for 100%. The whole area was grown to 4H-SiC epilayer, revealing two types of surface regions which are hexagonal chain-shape and smooth surface. The smooth surface could be obtained due to high dislocation density of the area when compared to the hexagonal chain region. Increasing the growth temperature helps to enhance the mobility of the adatoms on the surface, lowering the probability for a two dimensional nucleation of 3C.

# LIST OF PUBLICATIONS

## 1. Journals (SCI)

### 1.1. International

1. **Hunhee Lee**, Hyunwoo Kim, Han Seok Seo, Dohyun Lee, Changhyun Kim, Suhyeong Lee, Hongjeon Kang, Jaeyeong Heo, and Hyeong Joon Kim. “Comparative Study of 4H-SiC Epitaxial Layers Grown on 4° Off-Axis Si- and C-Face Substrates Using Bistrimethylsilylmethane Precursor”, *ECS Journal of Solid State Science and Technology*, **4** (8) N89-N95 (2015)

2. Changhyun Kim, Suhyeong Lee, Jeong Hyun Moon, Joon Rae Kim, **Hunhee Lee**, Hongjeon Kang, Jaeyeong Heo, and Hyeong Joon Kim, “The effect of reduced oxidation process using ammonia annealing and deposited oxides on 4H-SiC metal-oxide-semiconductor structure”, *ECS Solid State Letters*, **4** (9) N9-N12 (2015)

3. Dohyun Lee, Changhyun Kim, **Hunhee Lee**, Suhyeong Lee, Hongjeon Kang, Hyunwoo Kim, Hui Kyung Park, Jaeyeong Heo, and Hyeong Joon Kim, “Improving the Barrier Height Uniformity of 4H-SiC Schottky Barrier Diodes by Nitric Oxide Post-Oxidation Annealing”, *IEEE Electron Device Letters*, **35**, 8, 868 (2014)

4. Changhyun Kim, Jeong Hyun Moon, Jeong Hyuk Yim, Do Hyun Lee, Jong

Ho Lee, **Hun Hee Lee**, and Hyeong Joon Kim, “Comparison of thermal and atomic-layer-deposited oxides on 4H-SiC after post-oxidation-annealing in nitric oxide”, *Applied Physics Letter*, **100**, 082112 (2012)

## **2. Proceeding**

1. **Hunhee Lee**, Han Seok Seo, Do Hyun Lee, Changhyun Kim, Hyunwoo Kim, and Hyeong Joon Kim, “Low temperature homoepitaxial growth of 4H-SiC on 4° off-axis carbon-face substrate using BTMSM source”, *Materials Science Forum*, **740-742** (2013) pp 247-250

## **3. Conferences**

### **3.1. International**

1. Changhyun Kim, Suhyeong Lee, **Hunhee Lee**, Hyunwoo Kim, Hong Jeon Kang, and Hyeong Joon Kim, “Enhancement of SiO<sub>2</sub>/4H-SiC interface properties using ALD oxides and nitridation”, Pacsurf 2014, 7-11 December 2014, Hawaii, USA

2. **Hunhee Lee**, Dohyun Lee, Changhyun Kim, Hyunwoo Kim, Suhyeong Lee, Hongjeon Kang, Hyeong Joon Kim, “Comparative study of 4H-SiC epitaxial layers grown on 4° off-axis Si- and C-face substrates using BTMSM”, ECSCRM 2014, 21-25 September 2014, Grenoble, France

3. Dohyun Lee, Changhyun Kim, **Hunhee Lee**, Suhyeong Lee, Hongjeon Kang, Hyunwoo Kim, Jeong Hyun Moon, Hyeong Joon Kim, “Improving uniformity of Schottky barrier height of 4H-SiC Schottky Barrier Diode by nitrated sacrificial oxidation”, ICSCRM 2013, 29 September – 4 October 2013, Miyazaki, Japan

4. Changhyun Kim, Do Hyun Lee, **Hun Hee Lee**, Hyunwoo Kim, and Hyeong Joon Kim, “Effect of deposition and annealing conditions on the characteristics of atomic layer deposited oxides/4H-SiC interface”, ECSCRM 2012, 2-6 September 2012, St.Petersburg, Russia

5. **Hunhee Lee**, Han Seok Seo, Do Hyun Lee, Changhyun Kim, Hyunwoo Kim, and Hyeong Joon Kim, “Low temperature homoepitaxial growth of 4H-SiC on 4° off-axis carbon-face substrate using BTMSM source, ECSCRM 2012, 2-6 September 2012, St.Petersburg, Russia

6. Changhyun Kim, Jeong Hyuk Yim, Do Hyun Lee, Han Seok Seo, **Hun Hee Lee**, Jeong Hyun Moon, and Hyeong Joon Kim, “Comparison of the thermal and atomic-layer-deposited oxides in 4H-SiC MOSFET in respect of nitridation effect and field effect mobility”, ICSCRM 2011, 11-16 September 2011, Cleveland, Ohio, USA

7. Do Hyun Lee, Jeong Hyuk Yim, Chang Hyun Kim, Han Seok Seo, **Hun hee Lee** and Hyeong Joon Kim, “Fabrication of 1A, 1500V 4H-SiC Schottky

Barrier Diodes with Field Guard Ring Edge Termination”, ICSCRM 2011, 11-16 September 2011, Cleveland, Ohio, USA

### 3.2. Domestic

1. 이훈희, 이도현, 김창현, 김현우, 이수형, 강홍전, 김형준, “Bis-trimethylsilylmethane 소스를 이용하여 Silicon(Si)-face 와 Carbon(C)-face 기판 위에 성장 한 4H-SiC epitaxial layer의 비교 연구”, 2014년 한국세라믹학회 추계총회 및 연구발표회, 15-17 October 2014, Yeosu, Korea
2. 이훈희, 김현우, 이도현, 김창현, 이수형, 강홍전, 김형준, “BTMSM 소스를 이용한 4° off-axis Si-face 와 C-face기판 에서의 4H-SiC 동종 단결정 박막 성장에 관한 비교 연구”, 한국반도체디스플레이기술학회 2014년 춘계학술대회, 5 June 2014, Pyeongtaek, Korea
3. 김창현, 이수형, 이도현, 이훈희, 김현우, 김형준, “원자층 증착산화막의 적층과 암모니아 열처리를 이용한 SiO<sub>2</sub>/4H-SiC 계면에서의 재산화 방지 및 절연특성의 향상 방법”, 한국반도체디스플레이기술학회 2013년 추계학술대회 및 제4회 반도체공정포럼 반도체차세대 공정장비기술 심포지엄, 23 October 2013, Bundang, Korea
4. 이도현, 김창현, 이훈희, 이수형, 강홍전, 김현우, 김형준, “NO 열처

리를 통한 4H-SiC 쇼트키 다이오드의 쇼트키 장벽 균일도와 항복전압 향상”, 2013년 한국세라믹학회 추계총회 및 연구발표회, 16-18 October 2013, ICC Jeju, Korea

5. 이훈희, 이도현, 김창현, 김현우, 이수형, 강홍전, 김성경, 김형준, “4° off-axis 4H-SiC 기판에서의 스텝 번칭이 발생하지 않는 Homoepitaxy 성장 연구”, 2013년 한국세라믹학회 추계총회 및 연구발표회, 16-18 October 2013, ICC Jeju, Korea

6. 김창현, 이수형, 이도현, 이훈희, 김현우, 강홍전, 김형준, "원자층 증착산화막의 적층과 암모니아 열처리를 이용한 SiO<sub>2</sub>/4H-SiC 계면의 재산화 방지 및 절연과피 특성의 향상방법" 2013년 한국세라믹학회 추계총회 및 연구발표회, 16-18 October 2013, ICC Jeju, Korea

7. 김창현, 이도현, 이수형, 이훈희, 김현우, 김형준, “재산화 방지를 위한 원자층 증착 산화막과 암모니아 열처리가 SiO<sub>2</sub>/4H-SiC에 미치는 영향”, 한국반도체디스플레이기술학회 2013년 춘계학술대회 및 제1회 SiC 전력반도체 심포지움, 31 May 2013, Seoul, Korea

8. 이훈희, 김현우, 이도현, 김창현, 이수형, 강홍전, 김형준, “BTMSM 소스를 이용한 on-axis 기판에서의 6H-SiC 동종 단결정 박막 성장에 관한 연구”, 한국반도체디스플레이기술학회 2013년 춘계학술대회 및

제1회 SiC 전력반도체 심포지움, 31 May 2013, Seoul, Korea

9. 김현우, 이훈희, 이도현, 김창현, 이수형, 강홍전, 김형준, “KOH 에칭을 이용한 4H-SiC 단결정 박막의 표면결함 분석”, 한국반도체디스플레이기술학회 2013년 춘계학술대회 및 제1회 SiC 전력반도체 심포지움, 31 May 2013, Seoul, Korea

10. 김성경, 서성인, 이훈희, 박상현, 김형준, "HTCVD 기술 개선을 위한 SiC 증착 시뮬레이션" 한국반도체디스플레이기술학회 2013년 춘계학술대회 및 제1회 SiC 전력반도체 심포지움, 31 May, 2013, Seoul, Korea

11. 김창현, 이도현, 이훈희, 김현우, 김형준, “원자층 증착 산화막의 성장 조건이 4H-SiC MOS 계면 특성에 미치는 영향”, 한국반도체디스플레이기술학회 2012년 추계학술대회, 10 October 2012, KINTEX, Ilsan, Korea

12. 이훈희, 이도현, 김창현, 김현우, 김형준, “4H-SiC 동종 단결정 박막 성장 조건에 따른 표면결함 분석”, 한국반도체디스플레이기술학회 2012년 추계학술대회, 10 October 2012, KINTEX, Ilsan, Korea

13. 김창현, 이도현, 이훈희, 김현우, 김형준, “The effect of nitridation on

4H-SiC MOS interface using atomic layer deposited oxides”, 한국반도체디스플레이기술학회 2012년 춘계학술대회 및 제2회 반디 제주포럼, 18 may 2012, Jeju, Korea

14. 이훈희, 이도현, 김창현, 김현우, 김형준, “Homoepitaxial growth of 4H-SiC on carbon-face substrate using BTMSM”, 한국반도체디스플레이기술학회 2012년 춘계학술대회 및 제2회 반디 제주포럼, 18 may 2012, Jeju, Korea

15. Hun Hee Lee, Han Seok Seo, Jeong Hyuk Yim, Do Hyun Lee, Changhyun Kim and Hyeong Joon Kim, “Homoepitaxial growth of 4H-SiC on carbon-face substrate using BTMSM”, 22<sup>nd</sup> Korean Conference on Semiconductor, 15 February 2012, Seoul, Korea

## ABSTRACT (IN KOREAN)

탄화 규소(SiC)는 그 전기적, 화학적, 열적 성질이 우수하여 고온, 고주파, 고출력용 반도체 소자 및 우주항공이나 발전소 같이 극한 환경에서 사용되는 반도체 소자의 재료로 응용 가능성이 매우 크다. 특히, 단결정 및 박막 성장 기술이 GaN이나 ZnO와 같은 다른 화합물 반도체 물질에 비하여 월등히 우수하다는 장점을 가지고 있다. 여러 polytype 중 특히 4H-SiC의 경우, 높은 포화전자이동도 등 좋은 물성과 그의 상업적인 기관 생산 및 판매가 가장 활발하다는 장점이 있어 최근에 매우 중점적으로 연구되고 있다. 고품질의 SiC 단결정 박막을 성장시키기 위해 지금까지 Molecular-beam epitaxy (MBE), liquid-phase epitaxy (LPE), vapor-phase epitaxy (VPE) 등의 방법이 시도되었지만, 아직 많은 문제점이 남아있어 이런 기존 방법들의 문제점들을 해결하고자 본 연구에서는 독성 및 발화성이 없어서 일반적인 SiH<sub>4</sub>을 이용한 공정에 비해 이점이 많은 유기실리콘 화합물원료인 bis-trimethylsilylmethane (BTMSM, C<sub>7</sub>H<sub>20</sub>Si<sub>2</sub>)을 사용하여 단결정 4H-SiC 박막을 metal organic chemical vapor deposition (MOCVD) 법으로 성장하였다. 게다가 BTMSM은 Si-C bonding structure를 가지고 있기 때문에 저온 성장이 가능하다는 장점도 가지고 있다.

4H-SiC 단결정 박막 성장에 off-axis angle이 다른 4°, 8° off-axis 기관 및 on-axis 기관과, 면 극성이 다른 Si-face와 C-face 기관을 이용하였으며, 성장 온도와 소스 유량은 각각 1240~1550 °C, 5-20 sccm을

사용하였다.

Off-axis 기판에서의 단결정 박막 성장 시 성장 온도가 높을수록, 소스 유량이 낮을수록 단결정 박막의 특성이 우수하였는데, 이는 step-controlled model로 설명이 가능하다. On-axis 기판에서의 성장 시에는 기판에 존재하는 나선 전위로부터 기인된 micro-step을 통해서 spiral 성장을 하였음을 확인하였다. 성장온도가 1480 °C 가 되면 표면 전체적으로 3C-SiC 구조의 여러 구역을 지나는 island 성장을 하였지만 중간 중간에 4H-SiC 구조의 hexagonal 모양으로 성장한 형상이 혼재되어 있는 것을 확인 할 수 있었다. 이는 BTMSM 소스를 on-axis 기판에서의 단결정 박막 성장에 적용 시 상대적으로 낮은 온도에서부터 기판과 동종인 4H-SiC 성장이 가능하다는 것이다. 그리고 성장온도가 1550 °C 가 되면 표면이 전체적으로 hexagonal 모양의 형상들이 연속하여 이어지는 형상뿐만 아니라 거시적으로도 매끄러운 표면을 가지는 단결정 박막으로 성장 하였음을 확인 하였으며, 전 영역이 100% 4H-SiC로 동종 단결정 박막의 성장이 이루어 졌음을 확인 하였다. 1550 °C 에서 성장한 샘플내의 매끄러운 영역은 그렇지 않은 영역보다 나선 전위의 밀도가 많고, 각각의 영역에서 spiral 성장을 할 때 서로 완전하게 만나게 되어 국부적으로 매끄러운 표면을 확보 할 수 있었다고 판단했다. 즉, 성장 온도를 높임에 따라 기판 표면에서의 흡착원자의 확산속도가 빨라지게 되고, 3C 핵 생성 및 성장의 가능성이 낮아지게 되어 4H-SiC 단결정 박막으로의 성장이 용이 한 것으로 생각한다.

4H-SiC epitaxy 성장 연구 시 지금까지 많은 연구자들이 Si-face기판에서의 성장을 주로 하였고, 면 극성이 다른 C-face기판에서의 연구는 많지 않을 뿐만 아니라 저온 성장이 가능한 유기실리콘 화합물 원료를 적용하여 C-face기판에서의 단결정 박막 성장은 보고된 바가 없어 본 연구에서는 BTMSM소스를 적용하여 면 극성에 따른 단결정 박막의 여러 특성들을 확인 하였다. 서로 다른 극성을 지니는 기판에서의 수소 식각 현상 및 BTMSM소스를 적용하여 성장한 단결정 박막의 여러 특성 차이점을 체계적으로 분석하였다. 1500 °C 수소 식각 시 Si-face 기판에서는 거대한 step-bunching이 발생하였고, C-face 기판에서는 몇몇 cluster들이 발생하였다. 반면 1450 °C 수소 식각 시에는 두 면 모두 좋은 양질의 표면을 확보할 수 있었다. Si-face기판 뿐만 아니라 C-face기판에서도 결정학적 결함이 없고, step-bunching도 발생하지 않은 양질의 동종 단결정 박막의 성장이 가능하였다. 각 면에서의 최적의 성장 조건은 Si-face기판인 경우 성장 온도 1320-1440 °C, BTMSM 소스 유량 5-10 sccm 이었으며, C-face기판은 그 보다 100 °C 가량 높은 1500 °C, BTMSM 소스 유량 5 sccm 일 때였다. 성장 온도와 소스 유량에 따른 극성이 다른 두 기판에서의 step-bunching과 결정학적 결함 발생의 메커니즘을 분석하고 제안하였다.

**주요어:** 4H-탄화규소, 동종 단결정 박막 성장, BTMSM, Si-face와 C-face 기판, off-axis 각, on-axis 기판

**학번:** 2009-23054

이 훈 회